Microstructural and Mechanical Characterization of Additively Manufactured Binary Metallic Alloys

Thesis by
Thomas Tuan Tran

In Partial Fulfillment of the Requirements for the
Degree of
Doctor of Philosophy

CALIFORNIA INSTITUTE OF TECHNOLOGY
Pasadena, California

2025
Defended May 21, 2025

Thomas Tuan Tran
ORCID: 0009-0003-7034-9486

Dedicated to my family,
to my fiancée Jocelyn,
and to our foster dogs
(mostly Kuma, who was present during the drafting of this thesis)

ACKNOWLEDGEMENTS

My growth as a scientist and researcher thus far has been a privilege afforded to me by the support of many mentors, colleagues, mentees, friends, and family. I would like to first thank my advisor Julia for her mentorship and guidance which began even before the start of my Ph.D. journey, when I was a visiting undergraduate student (SURF) shuttling through Los Angeles each day during the summer of 2019. I am grateful to have worked in the interdisciplinary lab you cultivated, and I have always appreciated the trust and creative freedom you grant us as students and researchers.

The culture of the Greer Group is invaluable, and I have always enjoyed the company and advice of all my lab mates, both former and present. I am grateful for early mentorship—as well as some continued collaboration—from Professors Rebecca Gallivan and Max Saccone and our Microlattices sub-sub-group. I am grateful for the camaraderie from my lab cohort: Dr. Wenxin Zhang, and future-Drs. Kevin Nakahara and Wenyuan Chen. Through this work, I am fortunate to have mentored brilliant undergraduate students in Maria Azcona-Baez, Kitty Joyce, and Anna Wu, as well as many San Marino High School Students, who inspired and invigorated new directions in my work.

I would also like to acknowledge my peers in my Caltech Materials Science cohort with whom I weathered the trials of virtual coursework and candidacies with, amid several variants of COVID-19. A special shout-out goes to future-Drs. Kevin Yu, Lily Shiau, Emily Hwang, and Sahil Patel, with whom I shared many fruitful and motivating discussions outside Red Door Café with.

I am thankful to have been supported by the National Science Foundation's Graduate Research Fellowship Program. This work would not be possible without the assistance of Dr. Austin Akey and the Harvard University Center for Nanoscale Systems (CNS); Dr. Mingjie Xu and the UC Irvine Materials Research Institute; Dr. Chi Ma and the Caltech GPS Analytical Facility; Dr. Jean-Philippe Harvey and the Centre for Research in Computational Chemistry; and Dr. Simon Billinge and Dr. Gihan Kwon at Brookhaven National Lab. I would also like to thank my committee: Professors Katherine Faber, Guruswami (Ravi) Ravichandran, and Hosea Nelson.

I could not have done this without the love and support of my family, who undoubtedly started it all.

ABSTRACT

Hydrogel infusion-based additive manufacturing (HIAM) is a chemically versatile solid-state processing pathway that allows 3D structuring of ceramics and metals with micro-scale precision. Using controlled thermal treatments of 3D-printed metal ion-infused gels, this process generates intricate microstructures which are heavily influenced by the kinetics of gas-solid reactions and their subsequent phase evolution. This work seeks to refine our understanding of the process-structure-property relationships in HIAM-produced alloys and provide general insights for AM-enabled alloy development and microstructure design using metal oxide reduction.

Through HIAM, we demonstrate the arbitrary alloying of Cu_xNi_{1-x} binary alloys, where systematic characterization of microstructures down to the atomic scale revealed that reduction, or the lack thereof, drove the formation of chemically homogeneous alloy grains with numerous annealing twins and entrapped unreduced oxide nano-inclusions, resulting in a hierarchical two-phase composite. These features appear to elevate the average nanoindentation hardnesses by up to four times that of bulk annealed Cu_xNi_{1-x} and lead to a composition dependence on the scaling of the "smaller is stronger" size effect in uniaxial micropillar compressions. This compositional dependence of hardness and deformation mechanisms arises from changes in reduction kinetics which influence the density of inclusions and voids developed by HIAM processing. As a result, HIAM demonstrates the capability to fabricate heterogeneous alloy systems as a result of their oxide reduction pathways, which are revealed by thermogravimetry experiments and kinetic analysis.

PUBLISHED CONTENT AND CONTRIBUTIONS

This thesis has been directly adapted from:

1. Tran, T. T., Gallivan, R. A. & Greer, J. R. Multiscale Microstructural and Mechanical Characterization of Cu-Ni Binary Alloys Reduced During Hydrogel Infusion Additive Manufacturing (HIAM). *Small, under review* (2025).

   T. T. T. participated in the conception of the project, fabricated all samples, conducted experiments, analyzed data, prepared the figures, and wrote the manuscript.

2. Tran, T. T. & Greer, J. R. Nonisothermal Kinetics of Reduction in Hydrogel Infusion-Based Additive Manufacturing. *In preparation* (2025).

   T. T. T. conceived the study, conducted experiments and analysis, and wrote the manuscript.

3. Tran, T. T., Zhang, W., Joyce, K. J., Wu, A. & Greer, J. R. Oxide-Dispersion Strengthened Alloys Printed via Hydrogel Infusion-Based Additive Manufacturing (HIAM). *In preparation* (2025).

   T. T. T. participated in the conception of the project, solved and analyzed the crystal structures, prepared the data, and participated in the writing of the manuscript.

Not directly adapted in this thesis:

4. Hylak, J., Tran, T. T. & Atwater, H. A. Growth and Characterization of Epitaxial $FeWO_4$ Thin Films with Controlled Oxygen Stoichiometry. *Chemistry of Materials, under review* (2025).

   T. T. T. conducted transmission electron microscopy experiments and analysis.

5. Kagias, M., Tran, T. T., Toniolo, P., Nakahara, K., Phillips, N. W. & Greer, J. R. Elucidating the link between energy absorption and morphology in scalable nanoarchitected materials with X-ray nano-ptychography and digital twins. *In preparation, preprint available at Research Square.* doi:10.21203/rs.3.rs-3536097/v2 (2025).

   T. T. T. participated in the conception of the project, performed mechanical experiments, and edited the manuscript.

6. Koch, T. *et al.* Approaching Standardization: Mechanical Material Testing of Macroscopic Two-Photon Polymerized Specimens. *Advanced Materials* **36,** 2308497. ISSN: 1521-4095. doi:10.1002/adma.202308497 (2024).

   T. T. T. conducted micro-tensile experiments and their analysis.

7. Li, Z. *et al.* Nanoporous amorphous carbon nanopillars with lightweight, ultrahigh strength, large fracture strain, and high damping capability. *Nature Communications* **15,** 8151. ISSN: 2041-1723. doi:10.1038/s41467-024-52359-6 (2024).

   T. T. T. conducted microcompression experiments and their analysis.

8. Zhang, W. *et al.* Suppressed Size Effect in Nanopillars with Hierarchical Microstructures Enabled by Nanoscale Additive Manufacturing. *Nano Letters* **23,** 8162–8170. ISSN: 1530-6984. doi:10.1021/acs.nanolett.3c02309 (2023).

   T.T.T. contributed to data analysis and edited the manuscript.

TABLE OF CONTENTS

LIST OF ILLUSTRATIONS

LIST OF TABLES

Number *Page*

Chapter 1

INTRODUCTION

The core objective throughout the discipline of materials science and engineering is to tailor the relationship between structure and properties to achieve desired performance goals in a given material system. Therefore, as we select and augment existing materials—or design and develop novel materials—it becomes imperative to elucidate how material fabrication processes arrange matter and form structures that consequently impact material responses to external stimuli. Characterization tools are integral in guiding our exploration and understanding of these process-structure-property relationships, providing feedback on how choices about chemistries or thermal treatments, for example, can be modified to form favorable structures and properties (Figure 1.1).

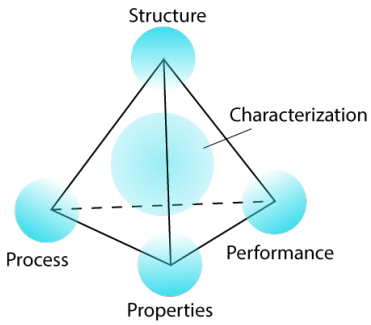

Figure 1.1: The materials tetrahedron represents the central paradigm of materials science and engineering. The process, structure, properties, and performance of a given material are all interrelated, and their characterization allows us to answer questions about the physical mechanisms and phenomena behind those relationships.

However, the characterization of structure is challenging as the length scales relevant to various properties span many degrees of magnitude. Structures and their defects can exist in materials throughout atomic bond lengths, nanoscale crystalline defects, intermolecular interactions, microscale grain structures, and macroscopic specimen geometries. Moreover, many local structures and phenomena originating at the atomic and nanoscale often collectively shape bulk material responses. For example, dislocation motion and grain boundary migration usually dictate the mechanical properties of polycrystalline metals.

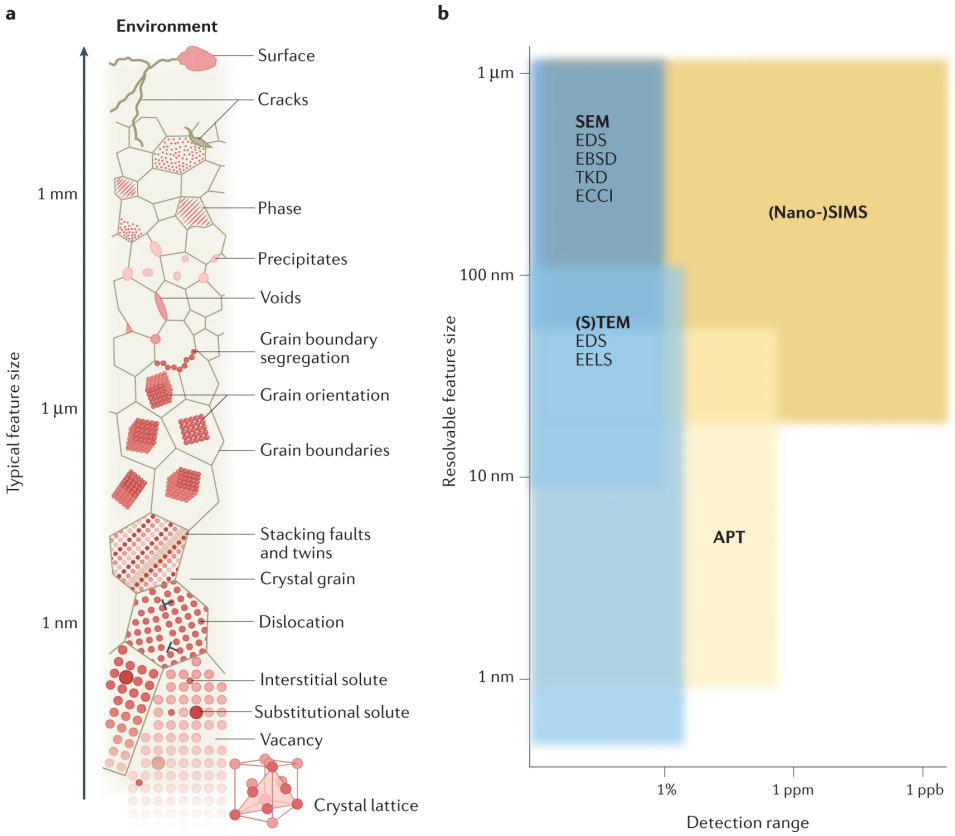

Figure 1.2: (a) Schematic of various microstructural features with their associated length scales and (b) the characterization techniques used to analyze them. Acronyms used: atom probe tomography (APT), electron backscattered diffraction (EBSD), electron-channelling contrast imaging (ECCI), energy-dispersive X-ray spectroscopy (EDS), electron energy loss spectroscopy (EELS), scanning electron microscopy (SEM), secondary ion mass spectrometry (SIMS), (scanning) transmission electron microscopy ((S)TEM), and transmission Kikuchi diffraction (TKD). Reproduced with permission from reference [1].

A complete understanding of the process-structure-property relationships must then encapsulate all length scales, including down to the atomic scale. This understanding has been facilitated by the continued development of techniques like electron microscopy throughout the last several decades, whose spatial resolution greatly surpasses that of optical light microscopes and approach sub-Ångstrom limits, since enabling the direct observation of countless nano- and atomic scale structures. While spatial resolution of characterization techniques have improved, recent decades have also seen the development of capabilities for in situ property measurements inside electron microscopes, illuminating the physical mechanisms by which structure and properties are interconnected (Figure 1.2).

While characterization techniques have rapidly advanced, emerging manufacturing technologies continue to present new opportunities and challenges in understanding how local processes shape material behavior. Specifically, additive manufacturing (AM) serves as an interesting case study due to its building of entire components from the bottom up using highly localized phenomena. As parts are built layer-by-layer, each layer may experience conditions like residual stresses that result in defects unique to AM that are not observed in conventional manufacturing.

1.1 Introduction to the Additive Manufacturing of Metals

In AM technologies, digital three-dimensional (3D) models made by computer-aided design (CAD) are sliced into layers in order to realize the object by the inkjet-printer-like deposition of material either layer-by-layer or spot-by-spot. This contrasts conventional "subtractive" manufacturing processes or formative manufacturing processes. In subtractive manufacturing, components are shaped by continuously removing excess material until the designed geometry is achieved. Formative processes produce near-net shape geometries but require tooling such as molds or dies into which molten liquids are solidified or raw material are deformed into shape. Because AM builds from the bottom-up, it is able to fabricate complex geometries previously impossible by subtractive and formative manufacturing. The clear benefits of AM approaches are their ability to consolidate parts and realize topologically optimized designs, reducing weight, improving process and material use efficiency, and minimizing manufacturing waste [2]. AM approaches can also print highly customized parts cost effectively and are well-suited for rapid prototyping in an iterative design process.

For these reasons, AM of metals is critical in industries such as aerospace and biomedical engineering to manufacture high-performance structural components. Much of commercial metal AM is dominated by two classes of techniques where the consolidation of feedstock material in the form of powder or wire is commonly achieved in the liquid state by energy supplied in the form of optical lasers, electron beams, or plasma arcs: powder bed fusion (PBF) and directed energy deposition (DED). In PBF technologies, thin layers of powder are repeatedly spread across a build platform and selectively sintered or melted by a scanning energy source (Figure 1.3(a)). In the DED class of metal AM techniques, the energy source and melting zone is continuously fed feedstock material (Figure 1.3(b)). On the other hand, some less popular approaches do form components fully in the solid state. Binder jetting AM deposits polymeric binder material into a powder bed to adhere

the particles and form an intermediate green body (Figure 1.3(c)). The green body is a composite which is thermally treated to first decompose the polymeric matrix and later sinter and densify the metallic part. In cold spray AM, powder particles are accelerated towards a substrate and are bonded by their impact.

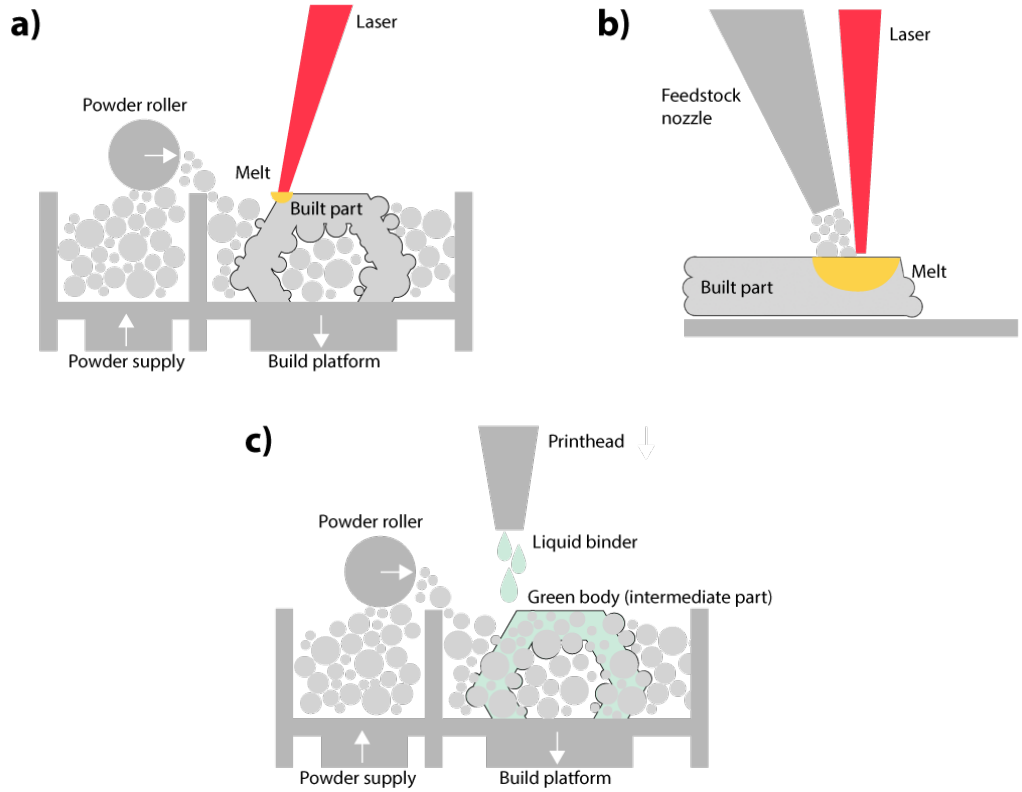

Figure 1.3: Various additive manufacturing techniques for fabricating metallic parts, which vary by the type of feedstock material and the energy source used. (a) Powder bed fusion and (b) directed energy deposition are depicted using metallic powders as feedstock material with a laser as an energy source. Both methods involve the solidification of melt pools, while (c) binder jetting deposits liquid binder into a powder bed to form a intermediate green body, to be formed into the metal part by subsequent thermal treatments.

1.2 Towards Microstructure Design with AM

Each metal AM technique poses different conditions through which material is consolidated and microstructures are formed. Unlike conventionally processed and finished parts, PBF- and DED-printed parts possess convoluted thermal histories due to cyclic local melting and solidification. In binder jetted parts, a polymeric matrix must be decomposed (i.e., "debinded") prior to densification of the metallic powder compacts through solid-state diffusion processes, while in cold sprayed parts,

powder particles are bound together by severe plastic deformation [3][4][5]. Each AM technology introduces characteristic process parameters that may create unique AM microstructures and defects. For instance, inherently high thermal gradients, thermal cycling, and varying feedstock material conditions in PBF and DED must be optimized, or else they can present major challenges, such as lack of fusion or hot cracking producing detrimental structural defects [3][4][5].

Under the right processing conditions, however, AM-induced microstructural defects can enhance material properties [6][7][8][9][10]. Residual stresses and thermal cycling developed during laser-PBF forms dislocation cell networks in 316L stainless steel, simultaneously improving both its strength and ductility (Figure 1.4)[8][6]. Similarly, dislocation cell structures associated with carbide and oxide precipitate arrays have been introduced as novel AM structures in an electron beam melted Co-based alloy and Cu, respectively, hardening and strengthening the base material [11][9]. These examples illustrate how AM processing can be harnessed to introduce novel internal microstructures with beneficial properties.

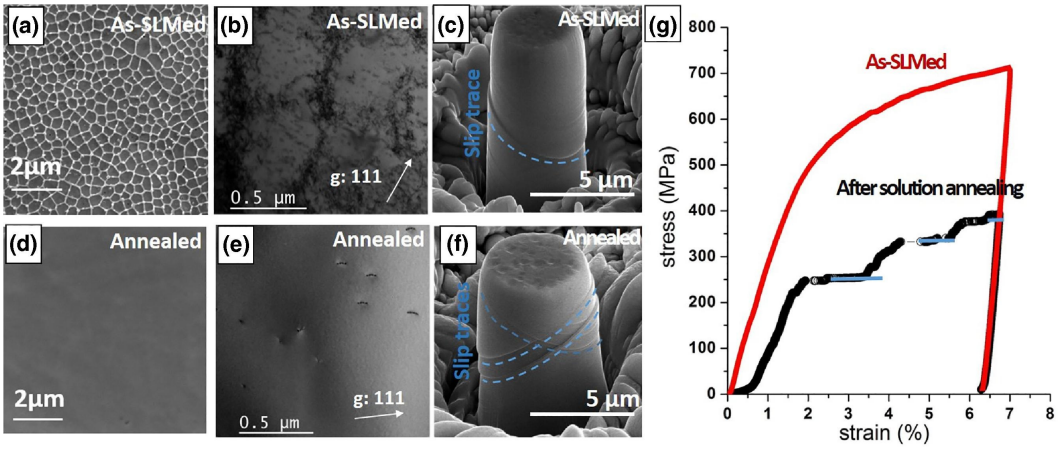

Figure 1.4: Improved mechanical properties in as-printed AM stainless steel via selective laser melting (SLM) due to dislocation networks formed during processing. The as-SLMed sample shows almost doubled yield strength and much smoother plastic flow behavior than the annealed sample. Reprinted from [8], with permission from Elsevier.

Furthermore, the additional degrees of freedom granted by AM process parameters presents an opportunity for microstructure design in situ. Dehoff et al. showed how controlling scanning strategies (i.e., changing the beam scanning pattern, speed, and power) can grant spatiotemporal control over heat transfer conditions in electron beam melting (Figure 1.5). By considering the solidification dynamics of the melt pool and indirectly adjusting the thermal gradient and liquid-solid interface

velocity, the rapid switching of conditions favoring columnar and equiaxed grain growth were achieved, demonstrating site-specific control of crystallographic texture in a Ni-based superalloy [12]. By understanding the mechanisms of microstructure formation and controlling the corresponding kinetic parameters to achieve desired microstructures—which in melt-based AM was achieved by combining an analytical understanding of melt solidifcation dynamics with the control of scanning parameters—AM becomes more than a tool for introducing geometric control and complexity to our parts: it becomes a promising platform for also introducing microstructural complexity.

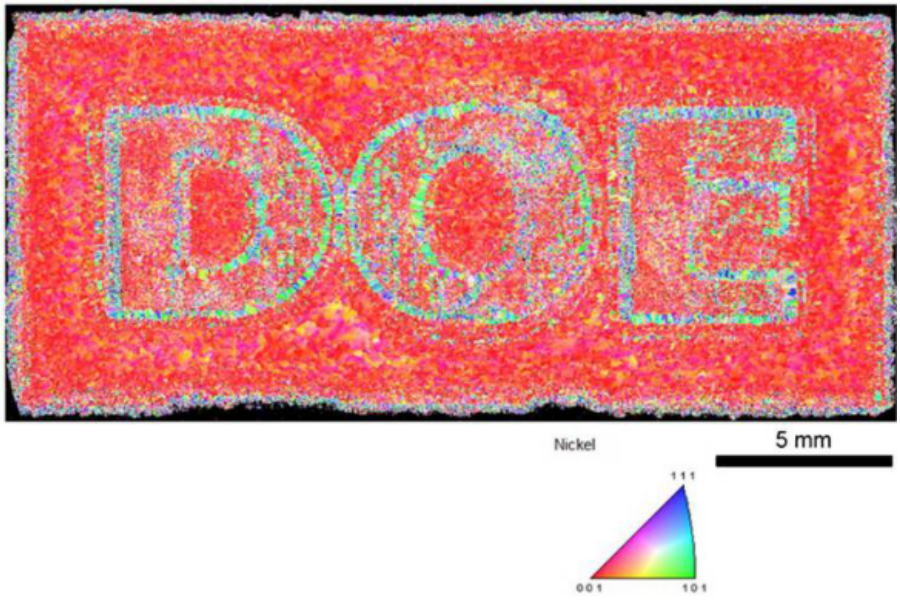

Figure 1.5: Control of crystallographic orientation in AM Ni-based superalloy Inconel 718 illustrated by inverse pole figure for FCC phase obtained on cross-section of electron beam-melted build obtained through EBSD: as intended, the bulk shows preferred <001> columnar solidification grain growth; at the part edges, misoriented growth is indicated by lack of any significant <001> components; lastly, the letters D, O, and E show a mixture of <001> growth and misoriented growth. © Copyright 2015, reprinted by permission of Informa UK Limited, trading as Taylor & Francis Group [12].

As such, the promise of engineering microstructures in situ throughout the manufacturing process is revitalizing fields like grain boundary engineering (GBE), which seek to optimize or improve properties like strength, thermal stability, and corrosion resistance through the manipulation of grain boundary structure [13][14]. AM defines new degrees of freedom by which precise control over microstructural evolution can be achieved [12][15]. By regulating heat transfer conditions like previously discussed for melt-based techniques, or conducing conditions for recrys-

tallization in the solid-state, AM offers new mechanisms for implementing GBE strategies directly during part fabrication while also overcoming limitations for conventional GBE such as restrictive part geometries [16][17]. While AM-based GBE is a growing area of research, knowledge gaps still remain regarding the mechanistic links between AM processes and structures. This is especially true for nascent AM technologies being developed for micro- and nanoscale printing, whose kinetic pathways and consequent microstructural evolution vastly differ from more mature AM technologies like PBF and DED.

1.3 Hydrogel Infusion-Based Additive Manufacturing

Hydrogel infusion-based additive manufacturing (HIAM) is one such AM approach which has emerged with distinct parameters for kinetic control because of its decoupling of material formation in the solid-state from its geometric definition of a part (Figure 1.6)[18][19][20][21][22][23][24]. While it is a solid-state approach most comparable to binder jetting AM, it distinguishes itself based on its lack of a metallic precursor material. Instead of starting with metal feedstock, HIAM combines high-resolution polymer printing with metal ion infusion and thermal treatments, taking a pyrometallurgical approach to form metals from their respective metal oxides. Metallic microarchitectures are formed after a complex series of chemical reactions and physical processes, enabling metal AM at low temperatures (below typical metal melting temperatures) and slow heating and cooling rates, while also providing compositional tunability through the substitution of the metal salts in the infusion solution.

The multi-step process for printing metallic architected parts in HIAM is as follows: geometries are first printed as organogels using standard polymer-resin AM processes like stereolithography (SLA) or digital light processing (DLP). Printed structures then undergo a solvent exchange step to displace the organic solvent with water, resulting in a hydrogel. The hydrogel is subsequently infused with metal ions. These gel precursors undergo a slow calcination process where the water is evaporated and the matrix is combusted. Lastly, the reduction of the remaining metal oxide structure also occurs by another gas-solid reaction with hydrogen [25][26][27]. Thus, microstructural evolution during HIAM occurs in the solid state unlike in LPBF and DED alloys. Additionally, it produces unique microstructural characteristics due to the slower heating and cooling schedules, substantial mass and volume loss, and generation of mechanical stresses during phase transformations—all while being subject to the kinetics of the reduction. The final metal-forming step, re-

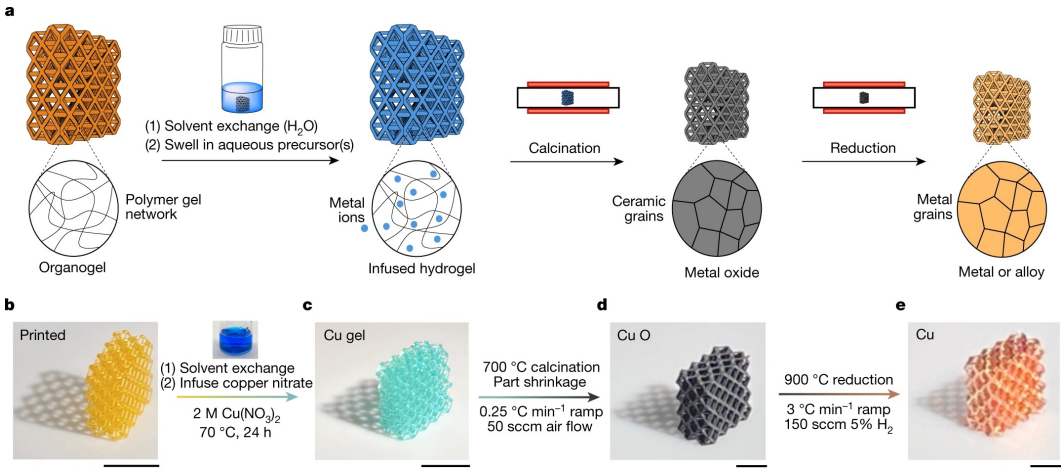

Figure 1.6: (a) Schematic of HIAM process. A DMF/PEGda-based 3D printed organogel structure is converted to an infused hydrogel replica after leaching out photoactive compounds, solvent exchange, and infusing an appropriate aqueous precursor. Subsequent calcination in air forms metal oxide structures, which are reduced to metals in forming gas. (b–e) Optical images of the HIAM process for Cu metal, showing (b) printed organogel, (c) infused hydrogel, (d) calcined metal oxide, and (e) reduced metal. Scale bars: b,c, 5 mm; d–e, 1 mm. Reproduced with permission from Springer Nature [18].

ductive annealing, alone produces a unique environment where solid-state atomic interdiffusion, sintering, grain growth, and densification occur simultaneously with reduction. We aim to study these reductively annealed microstructures and develop an understanding of their process-structure-property relationships and shed light on it as a novel pathway to tailor AM microstructures.

1.4 Thesis Summary

This thesis aims to elucidate the process-structure-property relationships in HIAM alloys with particular emphasis on the microstructural evolution of the metal-forming thermal treatment and its impact on mechanical properties. We first evaluate the complex microstructure and properties exhibited even by the simple binary solid solution system Cu-Ni. Later we discuss how the varying kinetics of reduction with composition can induce hetereogeneity in increasingly complex systems which feature immiscibility or irreducibility. We conclude with general insights on HIAM-based approach to alloy development and microstructural design.

Chapter 2 demonstrates the fabrication of Cu_xNi_{1-x} alloys of arbitrary composition and presents a multiscale experimental framework for characterizing their additively manufactured microstructures. We identify and discuss the formation of mi-

crostructural features idiosyncratic to HIAM-fabricated alloys, including chemically homogeneous, equiaxed, fine grains with numerous annealing twins and hierarchical unreduced oxide structures, which occur in Cu_xNi_{1-x} as a result of extensive grain growth and phase transformations. Chapter 3 extends the mechanical characterization performed on the HIAM Cu_xNi_{1-x} system to uncover the extent of anomalous hardening beyond the HIAM-fabricated $Cu_{55}Ni_{45}$ composition previously tested via nanoindentation by Saccone et al [18]. The intergranular mechanical response, where deformed volumes contain interfacial features like grain and twin boundaries, is compared to the intragranular response affected by lattice-scale defects and extrinsic size effects. Their differences highlight additional microstructural insights into the defect distribution within HIAM Cu_xNi_{1-x} grains. The multiscale mechanical characterization approach showcases the strength of combining a microscale fabrication approach with in situ micromechanical tests to probe deformation mechanisms in solid solutions. Chapter 4 introduces the development of HIAM-fabricated multiphase alloys such as oxide dispersion-strengthened (ODS) alloys or dual-phase alloys. We review how material selection influences the pathway to reduction based on their oxides' reducibilities and their phase stability throughout the HIAM thermal treatments. Chapter 5 refines our understanding of the reductive annealing thermal treatment in the microstructural evolution of HIAM alloys. Multi-step kinetics of reduction in HIAM are investigated with nonisothermal thermogravimetry experiments and mathematical deconvolution to ascertain the predominant reaction mechanisms during the thermal treatment. Finally, Chapter 6 briefly summarizes the findings of the earlier chapters and provides an outlook for HIAM-based alloy design. We recontextualize the microstructural evolution of the various HIAM alloys presented in the thesis and discuss the future of alloy design and microstructural engineering using AM.

Chapter 2

MULTISCALE MICROSTRUCTURAL CHARACTERIZATION OF HIAM CU_XNI_{1-X}

This chapter has been directly adapted from:

Tran, T. T. *et al.* Multiscale Microstructural and Mechanical Characterization of Cu-Ni Binary Alloys Reduced During Hydrogel Infusion Additive Manufacturing (HIAM). *Small, under review* (2025)

2.1 Introduction

While early studies on hydrogel infusion additive manufacturing of metallic micro- and nanoarchitectures demonstrated the viability of the approach by focusing on its compositional tunability and its ability to print complex geometries, there has been limited insight thus far into the local processes that govern their microstructural evolution and properties. For example, in HIAM-fabricated Cu and $Cu_{55}Ni_{45}$, HIAM's complex microstructural evolution led to high reported nanoindentation hardnesses by Saccone & Gallivan et al., which exceeded literature values by 47% and 15%, respectively [18]. One of the hypotheses put forward to explain the additional hardness enhancement was the incorporation of carbon into the lattice. However, the specific microstructural features and mechanisms that elicited the superior mechanical characteristics of these alloys remain to be uncovered, in part because the microstructural analysis lacked the necessary spatial resolution and chemical sensitivity. As a result, the connection between these properties and HIAM processing is poorly understood and necessitate a more thorough characterization of the microstructures formed.

This chapter further examines the Cu_xNi_{1-x} binary alloy system as a model HIAM material, since it has been shown to generate hardened, homogeneously microstructured architectures on the microscale. As a single phase solid solution, it provides a platform the explore potential non-equilibrium effects induced by HIAM's convoluted processing steps which include chemical reduction, interdiffusion, and grain growth occurring during reductive annealing. By varying Cu_xNi_{1-x} alloy composition and employing a multiscale characterization framework, composition-dependent differences in the processing conditions and microstructure are high-

lighted and provide mechanistic insights into HIAM binary alloys' microstructural evolution, i.e., reduction reaction kinetics and its thermally activated consolidation.

The microstructures and defects formed by the HIAM Cu_xNi_{1-x} binary alloy system are investigated by a suite of complementary characterization techniques whose analytical resolution range from the micro to the atomic scale. Beyond scanning electron microscopy and energy-dispersive spectroscopy providing microscale morphological and compositional information, electron backscatter diffraction quantifies crystallographic grain and twin structures and texture, and transmission electron microscopy and electron diffraction reveals nanoscale phases and defects stemming from HIAM. In addition, preliminary atom probe tomography is used for 3D chemical mapping on an atom-by-atom basis with sub-nm resolution to analyze solute partitioning. The highly sensitive and localized microstructural analysis is complemented by atomic pair distribution function analysis, which is able to sample bulk material and yet provide information of local atomic structure and their degree of ordering. Together, these techniques enable a comprehensive understanding of the multiscale microstructural evolution in HIAM-fabricated Cu_xNi_{1-x}.

2.2 Hydrogel Infusion-Based Additive Manufacturing of Binary Alloys

Cu_xNi_{1-x} alloy lattices are fabricated following the hydrogel infusion-based additive manufacturing (HIAM) procedure as outlined by Saccone et al. [18]: beginning with N,N-dimethylformamide (DMF) and polyethylene glycol diacrylate (PEGda)-based photoresin, architected organogels are polymerized layer-by-layer via a 405 nm digital light processing (DLP) printer (AutoDesk Ember) and subjected to solvent exchange, metal salt infusion, calcination, and reductive annealing steps to convert the printed materials to their desired alloy compositions.

Printed organogel geometries consisted of 2.5-D honeycomb structures with designated wall thicknesses of 250 μm, hexagon edge lengths of 625 μm, and specimen heights of 5 mm. During the infusion step, the hydrogels were infused by submerging them in varying volumetric ratios of 2 M solutions of copper (II) nitrate hemi(pentahydrate) and nickel (II) nitrate hexahydrate targeting Cu_xNi_{1-x} compositions x = 0, 5, 10, 15, 35, 50, 75, and 100. Heating infusion solutions to 70°C for 24 hours aids diffusion of the precursor metal ions throughout the thin wall thicknesses. During the calcination thermal treatment, infused gels are subject to 700°C at a mass flow of 50 sccm compressed air for 6 hours. Nanocrystalline oxide structures are recovered from this process and are subsequently subject to 900°C with mass flow

of 150 sccm forming gas (N_2 - 5% H_2) for 3 hours. The calcination heating rate is 0.25°C/min, and the reductive annealing rate is 3°C/min.

2.3 Scanning Electron Microscopy (SEM) and Energy Dispersive X-Ray Spectroscopy (EDS)

Secondary electron micrographs were captured using a dual-beam FIB-SEM at electron accelerating voltages between 10 and 20 kV (FEI Versa 3D Dual Beam). To determine the nominal alloy compositions, the atomic ratio of Cu to Ni are calculated from quantified EDS spectra (Bruker XFlash, Bruker ESPRIT). The reported value is an average. Measured alloy compositions differed from target compositions presumably due to varying affinities of the Cu^{2+} and Ni^{2+} species to the hydrogel network.

2.4 Electron Backscatter Diffraction (EBSD)

Traditional metallographic sample preparation was performed prior to EBSD and nanoindentation analysis. Specimens were mounted in epoxy (Buehler EpoxiCure™ 2 Epoxy Resin 20-3430-128 and Hardener 20-3432-032) loaded with 50 wt.% Ni powder as a conductive filler (Buehler 20-8500) and subsequently ground and polished with silicon carbide papers from grit number 240 up to 1200. Further polishing was performed with a 1 μm Buehler MetaDi polycrystalline diamond suspension before electrochemical polishing at 16 V using a 60:40 volume ratio of 85% phosphoric acid and deionized water as an electrolyte (Struers LectroPol-5).

Orientation mapping was performed across honeycomb wall thicknesses at a 20 kV accelerating voltage in a variable pressure SEM (LEO (ZEISS) 1550 VP, HKL Nordlys II). Tilt corrections were applied to the collected maps to correct for the SEM stage tilt of 70°. Map step sizes ranged between 80-200 nm. Standard noise reduction was performed in the HKL Channel 5 Tango software to remove isolated, incorrectly indexed points and to extrapolate solutions for small regions that could not be indexed (grain boundaries, for example). Grains were detected by identifying areas of the same crystallographic orientation while excluding adjacent grains with a $\Sigma 3$ $\langle 111 \rangle$ relationship to avoid over-counting twins. Average grain diameters were calculated from measured grain areas, assuming perfect circular fits (i.e., the diameter of grain I would be $d_i = \sqrt{4/\pi A_i}$). Resulting grain diameter histograms are fit with log-normal distributions from which mean and median grain sizes are calculated.

2.5 Transmission Electron Microscopy (TEM)

TEM lamellae were FIB-milled from the walls of as-fabricated HIAM Cu_xNi_{1-x} samples, lifted out and attached to Mo grids using a dual-beam SEM. Prior to FIB milling, a Pt protective layer was deposited, after which coarse milling was performed using the Ga+ FIB (FEI Versa 3D Dual Beam) at 30 kV and 5nA. Lamella thinning was done at 8kV and 48 pA. All TEM characterization (high-resolution imaging (HRTEM), selected area electron diffraction, energy dispersive spectroscopy in scanning mode (STEM-EDS)) were performed at 200 kV in a JEOL JEM-2800. Post-processing of any images in Gatan Micrograph were limited to adjustments in brightness, contrast, and gamma, as well as fast Fourier transforms (FFT) for HRTEM images.

2.6 Atom Probe Tomography (APT)

Atom probe tomography (APT) combines field ion microscopy with time-of-flight mass spectrometry to enable 3D compositional mapping with sub-nanometer resolution. A destructive technique, needle-shaped specimens are field ionized and evaporated atom-by-atom in front of an ion detector by a field $F = \frac{V}{kR}$ where V is the external applied voltage, F is the field correction factor, and R is the radius of the needle-shaped specimen typically below 100 nm. The mass spectrometer provides sufficient mass resolution with virtually no limits on the atomic number of the elements analyzed as well as sensitivity for detecting elemental isotopes, and based on the position of the incoming ions onto the detector, a 3D point cloud can be reconstructed.

A $Cu_{15}Ni_{85}$ atom probe tomography specimen was prepared using a dual-beam instrument (Versa 3D LoVac). First, a rectangular area of interest whose length visibly intersects several grain interfaces in the alloy was selected. Annealing twin boundaries were targeted in addition to random high-angle grain boundaries. A 2 μm Pt protective layer is deposited via electron-beam induced deposition followed by ion-induced deposition to minimize FIB damage of the APT specimens by ion implantation or amorphization. Then, a V-shaped groove is machined undercutting the region of interest. The resulting wedge shaped area containing the region of interest is attached onto the Si posts of the M22 microtip array available from CAMECA (26880). The attached specimen is sharpened into needle tips by FIB milling annuli from the top down. The specimen is run with a local electron atom probe (CAMECA LEAP 4000X HR) with 355 nm UV laser pulses to assist the field ionization through local heating. Based on each evaporated ion's corresponding

times of flight and detected coordinates, a 3D point cloud is reconstructed.

2.7 X-Ray Total Scattering and Pair Distribution Function (PDF) Analysis

In the total scattering method, the experimental atomic pair distribution $G(r)$ function is derived from a structure function $S(Q)$ that contains both Bragg and diffuse intensities from X-ray, electron, or neutron diffraction experiments. It is dependent on Q, the magnitude of the diffraction vector ($Q = 4\pi \sin\theta/\lambda$ during elastic scattering, where 2θ is the scattering angle and λ is the scattering wavelength). The PDF is the Fourier transform of $Q[S(Q) - 1]$, also known as the total scattering structure function $F(Q)$ [29]:

$$G(r) = \frac{2}{\pi} \int_{Q_{min}}^{Q_{max}} Q[S(Q) - 1] \sin(Qr) dQ, \tag{2.1}$$

where Q_{min} and Q_{max} are the limits of Q defined by the experimental scattering setup. $G(r)$ offers a description of how pairs of atoms are distributed in a material. Considering a random atom, the real-space distances at which peaks occur map out the likelihood that another atom occupies that space. The peaks of the reduced PDF $G(r)$ specifically map out the deviation from a random atom distribution represented by the oscillations' lower bound of $-4\pi r\rho_0$, where is the ρ_0 average number density of the material.

Copper and nickel oxides, produced via the standard HIAM calcination treatment with a peak temperature of 700°C for 3 hours, were ground via mortar and pestle to uniform fineness to fill into 1 mm inner diameter kapton capillaries. As-fabricated metallic HIAM Cu, Ni, and Cu_xNi_{1-x} specimens resulting from the standard reductive annealing treatment at 900°C for 6 hours were too ductile to ground into fine powders, so a razor blade was used to mince the structures into sub-mm fragments to fill the capillaries.

Samples were run at the Pair Distribution Function beamline (28-ID-1) at the National Synchrotron Light Source-II (NSLS-II) of Brookhaven National Lab using an incident X-ray wavelength of 0.1665 Å. Measurements were taken at room temperature and ambient conditions with a Perkin Elmer amorphous silicon 2D detector. Background signal intensities due to scattering resulting from the Kapton tube and air was corrected by subtracting the signal collected from an identical empty Kapton capillary. Signal was calibrated using a CeO_2 standard to acquire instrument parameters for Rietveld analysis. 2D diffraction rings are integrated using Dioptas to

give a 1D pattern that [**prescher_dioptas_2015**], from which reduced atomic pair distribution functions are calculated using the PDFgetX3 package using diffraction data ranging from $Q = 0 - 25$ Å^{-1} [30]. The local structures probed by atomic PDF are fit with a real-space Rietveld refinement approach using PDFgui [31][32]. Starting from known phases Cu, Ni, CuO, and NiO, the scale factors, unit cell lattice parameters, isotropic atomic displacement parameters, quadratic atomic correlation factors, signal dampening, and peak broadening are each refined.

2.8 Multiscale Microstructure in HIAM Cu_xNi_{1-x}

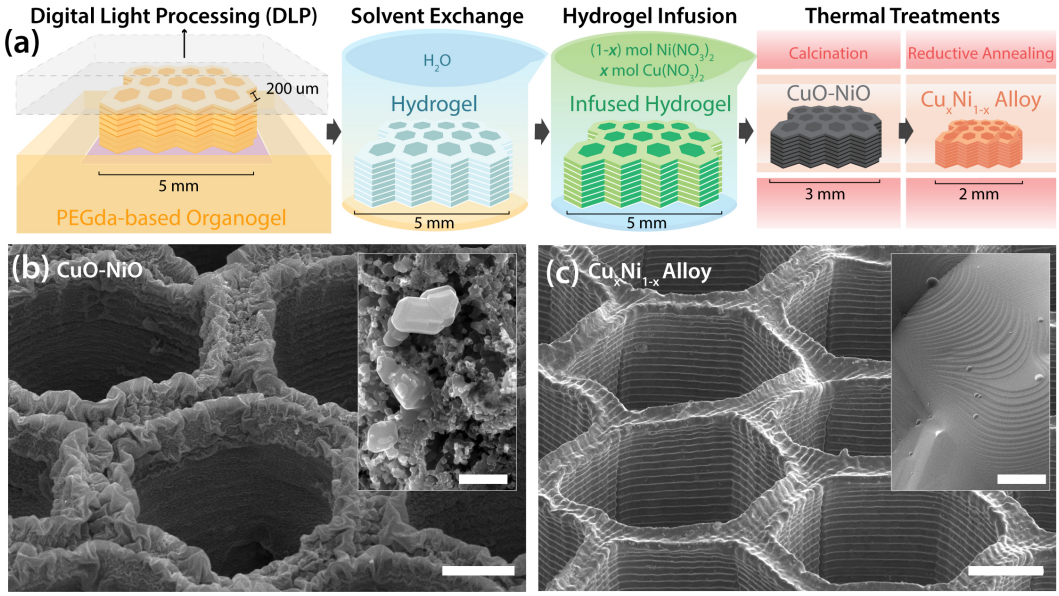

Figure 2.1: Cu_xNi_{1-x} alloy formation via HIAM. (a) Schematic illustration of HIAM process for making Cu_xNi_{1-x} sample shaped in a vertically stacked honeycomb pattern. (b-c) SEM images reveal morphologies for a representative sample after two consecutive thermal treatments. (b) Calcination converts the infused gel into a CuO-NiO composite system and reveals a highly porous agglomerate of faceted nanocrystals (scale bar 100 μm, inset scale bar 500 nm. (c) The reductive annealing thermal treatment reduces the oxide into its parent metals and produces an alloy Cu_xNi_{1-x} that is mostly dense (scale bar 100 μm, inset scale bar 1 μm).

Figure 2.1 shows the fabrication route for producing Cu_xNi_{1-x} alloys via HIAM (Figure 2.1a) and depicts the typical morphology of Cu_xNi_{1-x} 2.5D honeycomb structures after calcination at 700°C for 3 hours under 150 sccm of compressed air flow and subsequent reductive annealing at 900°C for 6 hours and 50 sccm flow of forming gas (N_2-5% H_2 mixture). These images reveal that the designed pattern fidelity is maintained throughout the thermal treatment steps (Figure 2.1b-c). Upon calcining, the metal ion-infused gel structure is converted to a highly

porous nanocrystalline oxide (Figure 2.1b). After reductive annealing, the surface morphology of all Cu_xNi_{1-x} alloys resembles that of a well-annealed polycrystal with prominent crystal facets visible in the SEM images (Figures 2.1c, 2.2, and 2.4), though sometimes containing sparsely distributed internal porosity, similar to what has been reported for the HIAM-synthesized pure Cu and Ni (Figures 2.3 and 2.5) [13].

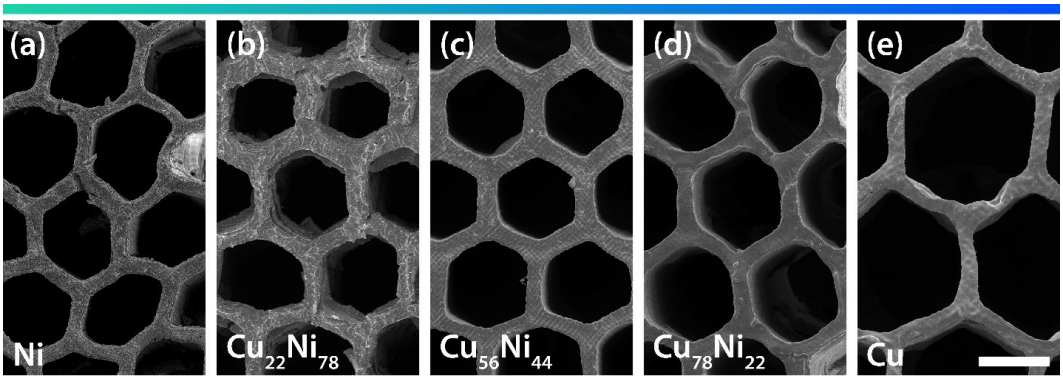

Figure 2.2: HIAM Cu_xNi_{1-x} honeycomb lattices. Secondary electron micrographs depicting surface morphologies and geometry maintained after the HIAM process as a function of composition (scale bar 200 μm).

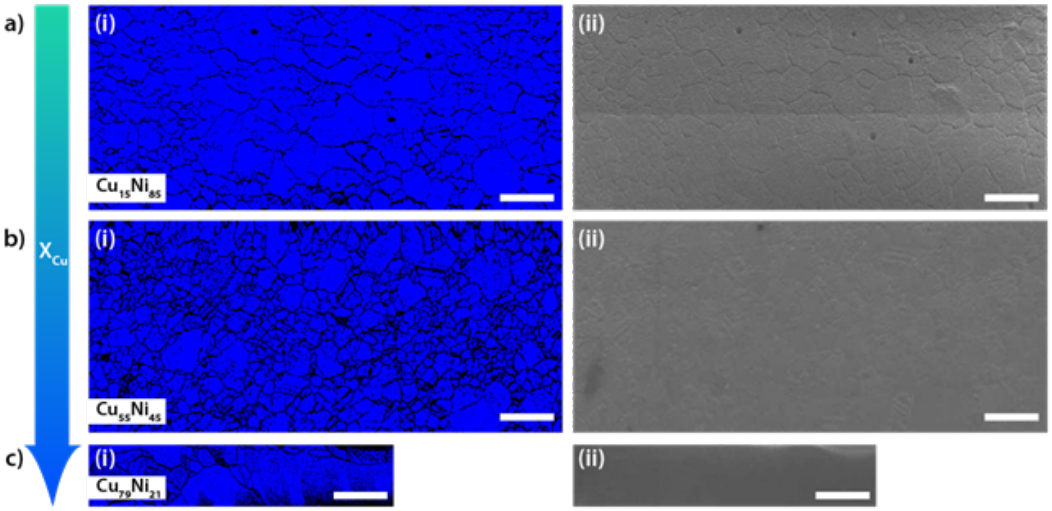

Figure 2.3: Phase mapping of HIAM Cu_xNi_{1-x}. Raw (unprocessed) phase maps from (a-c) same specimens as Figure 2.4. (a-c)(i) Spots whose electron back scatterbackscatter diffraction patterns are indexed as face-centered cubic (FCC) are marked as blue, while any unindexed or zero-solution spots are marked as black. (a-c)(ii) Corresponding secondary electron micrographs of polished areas mapped by EBSD.

Figure 2.4a-c(i) shows the grain orientation maps for Ni-rich, near-equiatomic, and Cu-rich HIAM Cu_xNi_{1-x} alloys, where each indexed point was identified as the single

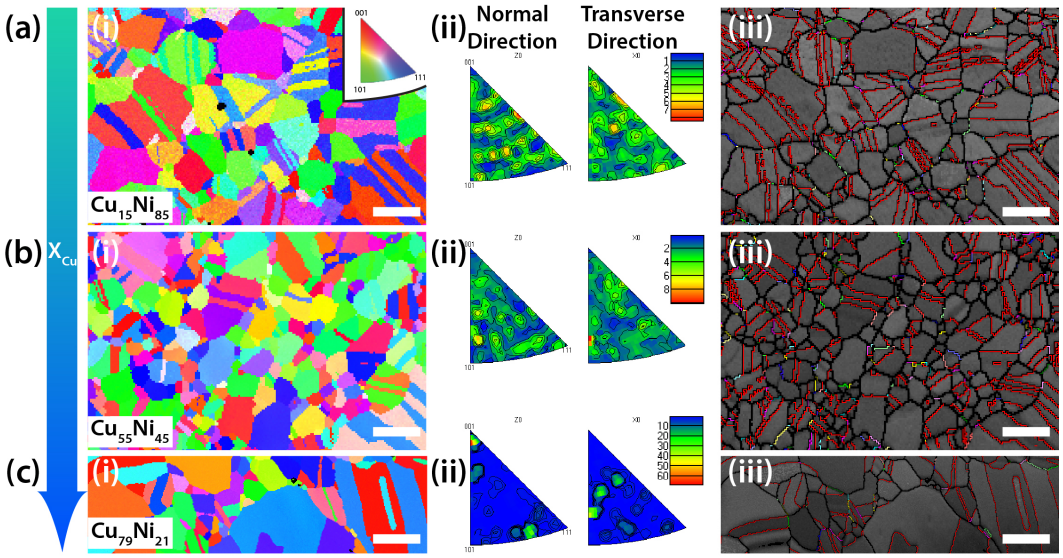

Figure 2.4: Electron Backscatter Diffraction (EBSD) analysis of HIAM Cu_xNi_{1-x} alloys. (a-c) (i) Crystallographic orientation maps of (a) $Cu_{15}Ni_{85}$, (b) $Cu_{55}Ni_{45}$, and (c) $Cu_{79}Ni_{21}$. Coloring is based on the specimen z-axis inverse pole figure according to the stereographic triangle, shown in 2(a)(i) and reveal the absence of texture or a preferred orientation. (ii) Inverse pole figures of specimen normal and transverse directions, which demonstrate the random orientation of HIAM Cu_xNi_{1-x}. (iii) Boundary maps show the presence of numerous annealing twin boundaries, with $\Sigma 3$ boundaries shown in red over a Kikuchi band contrast image and the high angle grain boundaries (misorientation<10°) outlined in black over the SEM image. Higher order Coincident Site Lattice (CSL) boundaries are demarcated by other colors, including green for $\Sigma 5$, blue for $\Sigma 7$, and magenta for $\Sigma 9$. Scale bar for all images is 5 μm.

phase face-centered cubic (FCC) solid solution of Cu and Ni (Figure 2.3). All maps highlight equiaxed and randomly oriented grain morphologies for both axial and transverse cross-sections of the honeycomb lattices. Grain size analysis shows an average grain size and standard error of 2.6 ± 0.19 μm for $Cu_{15}Ni_{85}$, 2.3 ± 0.04 μm for $Cu_{55}Ni_{45}$, and 4.3 ± 0.48 μm for $Cu_{79}Ni_{21}$. The grain sizes follow a log-normal distribution for all alloys, each containing large grains in excess of 30 μm (Figure 2.6 and Table 2.1). Figure 2.4(iii) depict multiple $\Sigma 3$ twin boundaries, indicated by the red lines, with higher order coincident site lattice (CSL) boundaries marked by green ($\Sigma 5$), blue ($\Sigma 7$), magenta ($\Sigma 9$), and yellow ($\Sigma 11$) lines. The fraction of twin boundaries relative to all other boundaries is 50.6% for $Cu_{15}Ni_{85}$, with a line density of 0.85 μm^{-1}, similar to what was observed for pure HIAM Cu_xNi_{1-x}, Cu, and Ni (Table 2.1, Figure 2.7).

Figure 2.8 illuminates additional hierarchical features, not observed in earlier stud-

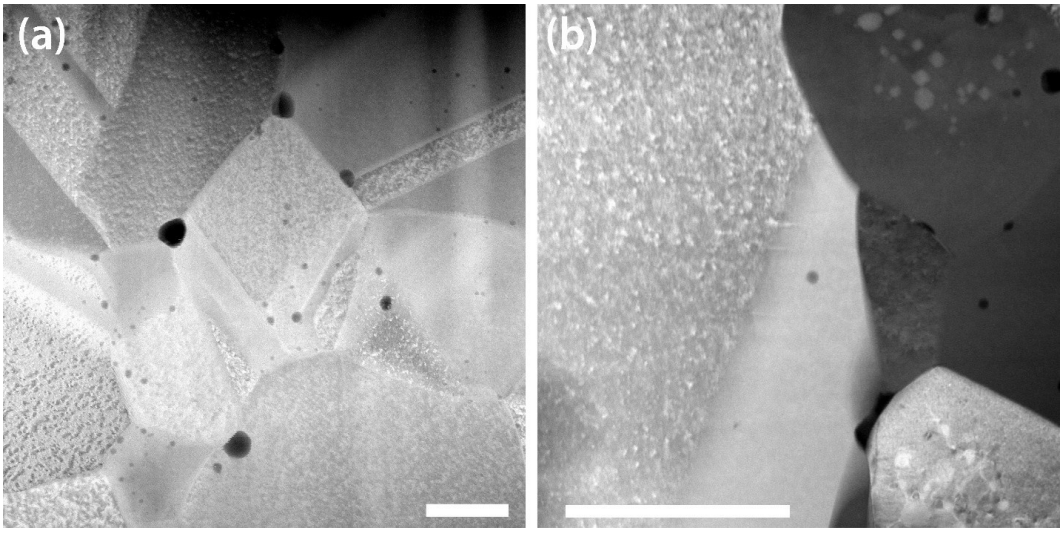

Figure 2.5: Internal porosity and unreduced grains in HIAM $Cu_{17}Ni_{83}$. Low-magnification STEM-HAADF images lamellae prepared by FIB liftout reveal (a) interior porosity (scale bar 500 nm) and (b) regions of partially unreduced oxide. Reduced nanoinclusions within oxide grains are visible in (b) by Z-contrast (scale bar 200 nm).

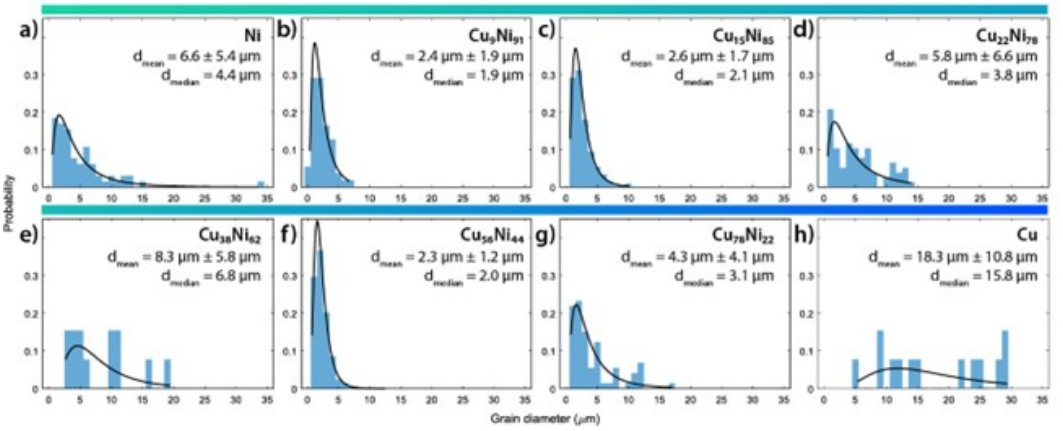

Figure 2.6: Grain size distributions for HIAM Cu, Ni, and Cu_xNi_{1-x}. Grain diameter histograms obtained from EBSD mapping. Log-normal distributions are applied from which the means and medians are calculated.

ies, within the microstructure of a representative HIAM-produced $Cu_{17}Ni_{83}$ alloy. Isolated nanopores, sub-50 nm in diameter, were observed within the grain interiors. Larger voids, over 100s of nm wide, were located alongside a region of grains relatively darker in atomic number (Z) contrast (Figures 2.8a and 2.5). The darker grains also encapsulate brighter nano-inclusions, suggesting chemical inhomogeneities between the dark grains and their surrounding grains, as well as between the dark grains and their inclusions (Figure 2.5b). HRTEM imaging of the composite grains (Figure

Table 2.1: **Summary of grain and boundary morphologies**. Reported bounds of mean grain diameter is a standard error, boundary percentages are relative to the length of all boundaries, and the line density is relative to the area scanned in EBSD.

Specimen Composition	# Grains Analyzed	Mean Grain Size (μm)	%CSL Boundary	%Σ3 Boundary	Σ3 Line Density (μm^{-1})
Cu	13	18.3 ± 0.8	60.7	54.1	–
$Cu_{78}Ni_{22}$	73	3.1 ± 0.1	49.7	58.6	0.26
$Cu_{56}Ni_{44}$	860	2.0 ± 0.0	68.8	37.4	0.31
$Cu_{38}Ni_{62}$	14	6.8 ± 0.4	62.3	59.9	0.28
$Cu_{22}Ni_{78}$	77	3.8 ± 0.1	67.1	59.5	0.53
$Cu_{15}Ni_{85}$	441	2.1 ± 0.0	59.8	50.6	0.85
$Cu_{9}Ni_{91}$	54	1.9 ± 0.4	60.1	51.5	0.42
Ni	65	5.1 ± 0.2	61.7	54.2	0.33

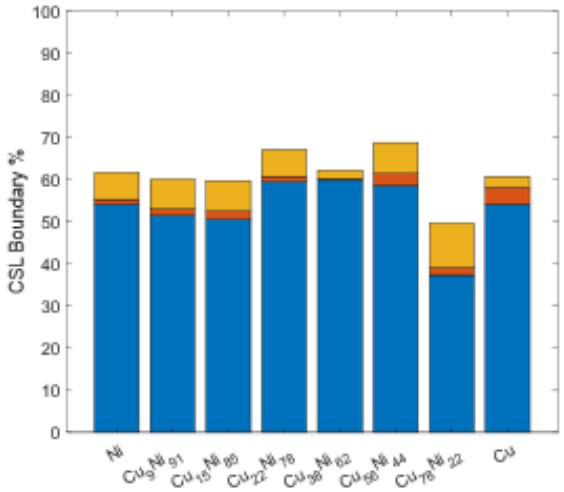

Figure 2.7: Low energy boundaries formed by HIAM. Percentages of Cu_xNi_{1-x} boundary lengths measured in EBSD which are CSL boundaries ($\Sigma \leq 29$). Blue, orange, and yellow bars correspond to Σ3, Σ9, and all other CSL boundaries.

2.8b) indicate translational Moiré fringing where nano-inclusions are located due to overlapping lattice fringes from two distinct crystalline phases. The periodicity is accurately described by a Moiré fringe spacing of 1.4 nm as calculated by

$$D = \frac{d_1 d_2}{d_1 - d_2}, \tag{2.2}$$

where D is the Moiré fringe spacing, and d_1 and d_2 are the parallel interplanar spacings of the matrix and precipitate phases.

Visible lattice spacings of the matrix phase, d = 2.3 Å, match that of interplanar

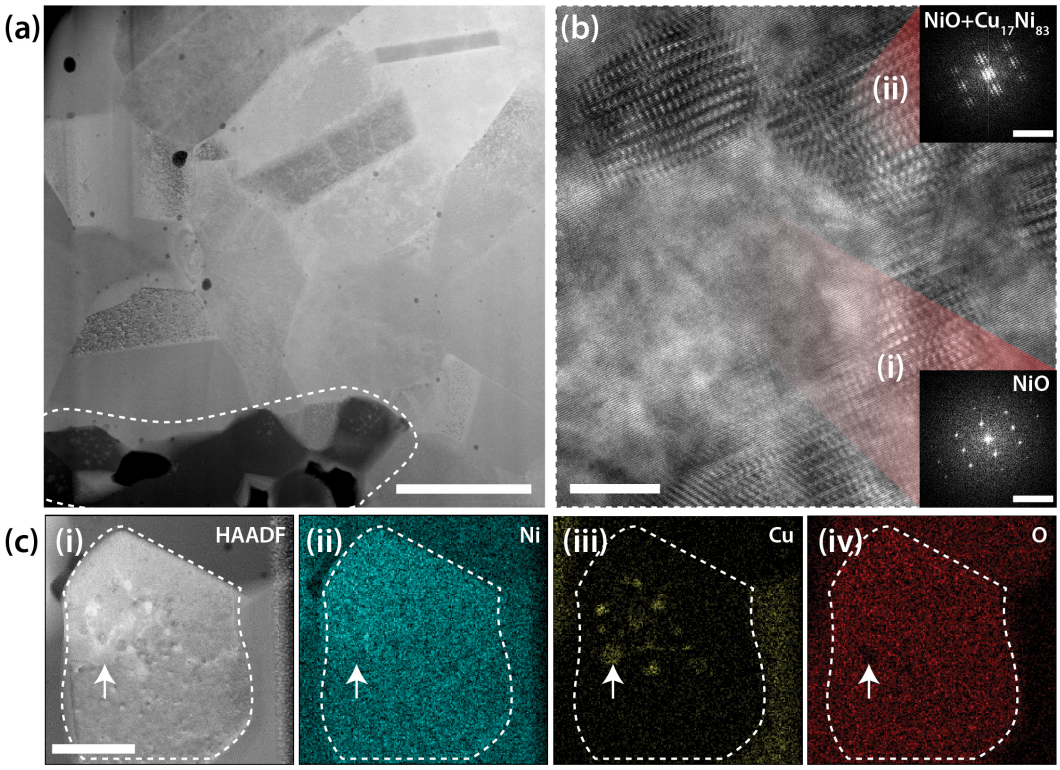

Figure 2.8: Hierarchical composite microstructure in HIAM $Cu_{17}Ni_{83}$. (a) STEM-HAADF image of a $Cu_{17}Ni_{83}$ alloy cross section reveals internal porosity and unreduced oxide grains incorporated into the microstructure by HIAM (scale bar 1 μm). The highlighted oxide grains which are adjacent to voids and darker in contrast are analyzed via (b) HRTEM. FFT diffractograms indicate lattice spacings corresponding to that of $\langle 112 \rangle$-oriented NiO. Translational Moiré fringing also conveys the presence of multiple nano-sized $Cu_{17}Ni_{83}$ inclusions (scale bar 10 nm, inset scale bars 10 nm^{-1}) which are identified with brighter Z-contrast in (c)(i) further STEM-HAADF imaging and (ii-iv) STEM-EDS mapping. Segregation of Cu and O is observed between the unreduced grain (highlighted) and surrounding alloy grains, as well as between the unreduced grain and its alloy inclusions (scale bar 200 nm).

distances of NiO {111} planes. At the inclusions, the Moiré patterns' spacings substantiate that the observed nano-inclusions consist of metallic Cu_xNi_{1-x}, since they are commensurate with those formed by parallel planes of FCC (Cu_xNi_{1-x}) and rock salt (NiO) crystal structures. Fast Fourier transform (FFT) diffractograms of the matrix phase match that of the NiO reciprocal lattice oriented along its $\langle 112 \rangle$ zone axis (Figure 2.8b(i)), while FFTs of the Moiré fringed regions replicate double diffraction effects between the two lattices (Figure 2.8b(ii)). The (Cu_xNi_{1-x}) nano-inclusions range in sizes below 10 nm and assume both spherical and cuboid morphologies, with the latter bound by {111} facets similar to [33]. Figure 2.8c confirms the inhomogeneous distribution of Cu and O within the composite grains.

The energy dispersive X-ray spectroscopy maps taken via a scanning transmission electron microscope (STEM-EDS) (Figure 2.8c(ii-iv)) convey that the composite grains' matrix phase is depleted in Cu and enriched in O relative to their inclusions and their surrounding grains. In HIAM $Cu_{17}Ni_{83}$, the composite grains which are darker in Z contrast in high-angle annular dark field (HAADF) mode are predominantly unreduced NiO grains with $Cu_{17}Ni_{83}$ nano-inclusions, and they are clustered together beside voids.

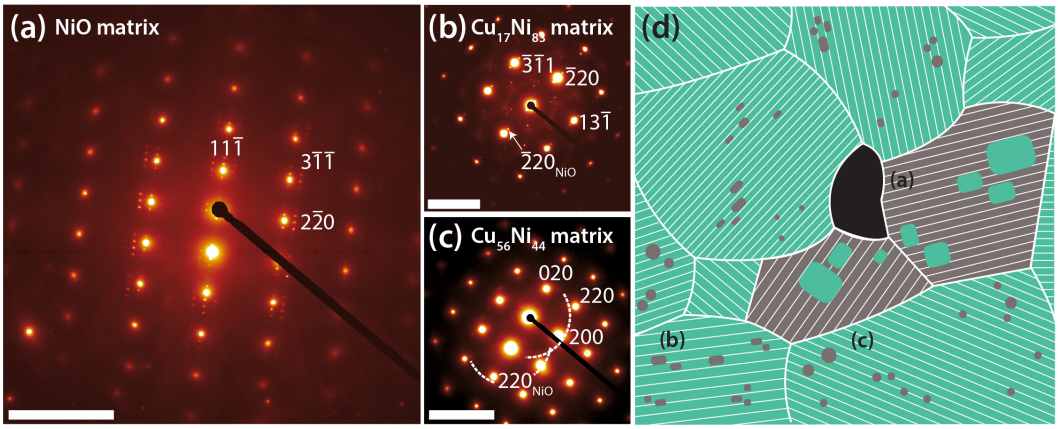

Figure 2.9: Analysis of HIAM-generated inclusions via double diffraction effects in selected area electron diffraction. (a) Within grains of unreduced oxide, a NiO ⟨112⟩ zone axis pattern and its satellite spots depict semicoherent alloy inclusions with a cube-on-cube orientation relationship. (b,c) Within predominantly metallic grains, additional (b) spots in a $Cu_{17}Ni_{83}$ ⟨114⟩ zone axis pattern and (c) rings in a $Cu_{56}Ni_{44}$ ⟨100⟩ zone axis pattern depict NiO inclusions that are respectively semicoherent and incoherent (scale bars 10 nm^{-1}). (d) Schematic summarizing various matrix-inclusion orientation relationships observed in HIAM Cu_xNi_{1-x}.

Indexed selected area electron diffraction (SAED) patterns of HIAM-fabricated Cu_xNi_{1-x} exhibit strong double diffraction effects which evidence several orientation relationships between matrix and inclusion phases within their hierarchical composite microstructure. Figure 2.9a, whose selected area contains one oxide grain with multiple nano-inclusions from Figure 2.8, reproduces the FFT diffractogram of Figure 2.8b(ii) with shows periodic arrays of dim satellite reflections around each intense fundamental reflection, reproducing the FFT diffractogram of Figure 2.8b(ii). The fundamental diffraction pattern belongs to the reciprocal lattice of ⟨112⟩-oriented rock salt NiO crystal with lattice parameter a = 4.2 Å[34]. The dimmer arrays of satellite reflections are formed from additional diffraction events with FCC Cu_xNi_{1-x} (a = 3.5-3.6 Å) nano-inclusions with the same orientation [35]. Electrons diffracted by the primary NiO matrix lattice diffract again through the

Cu_xNi_{1-x} inclusions, i.e., each diffraction spot of the NiO pattern acts as an origin through which the slightly larger diffraction pattern of the Cu_xNi_{1-x} lattice is replicated and multiplied. Because the selected area contains multiple inclusions in one grain, the sampled inclusions all share semicoherent boundaries with the matrix grain with a cube-on-cube orientation relationship between the FCC and rock salt phases (i.e., $\langle 112 \rangle_{NiO} \parallel \langle 112 \rangle_{Cu_xNi_{1-x}}$) and 18% misfit.

Additional diffracted intensities also indicate the appearance of oxides as inclusions present within an alloy matrix (Figure 2.9b,c). When recording diffraction patterns away from the unreduced region in HIAM $Cu_{17}Ni_{83}$, the fundamental patterns are instead formed by an FCC $Cu_{17}Ni_{83}$ structure, and additional dim spots corresponding to the {220} reflection by a rock salt NiO structure are replicated throughout the SAED patterns by double diffraction (Figure 2.9b). The spots again indicate a semicoherent, cube-on-cube orientation relationship between oxide inclusions and their parent alloy grain. In contrast, oxide inclusions from HIAM $Cu_{56}Ni_{44}$ are incoherent with their parent alloy grain (Figure 2.9c). Double diffraction between the $Cu_{56}Ni_{44}$ alloy and the randomly oriented inclusions produces the multiple faint diffraction rings with NiO {220} spacing centered around $Cu_{56}Ni_{44}$ diffraction spots. Figure 2.9d summarizes the types of matrix-inclusion relationships identified in the composite microstructure of HIAM-fabricated Cu_xNi_{1-x} by SAED analysis.

Local Chemistry and Structure

Following preparation of the HIAM $Cu_{17}Ni_{83}$ needle specimen, it became evident that no interfaces from the sampled region survived the polishing step and that the needle only contained material from within one grain interior (Figures 2.10b,c). Nevertheless, after correcting for the background signal, the needle specimen yielded 10,492,560 ions for analysis. Ion types detected were primarily those belonging to Ni and Cu, with minor and trace fractions belonging to C, O, and H (Figure 2.11). H-containing ions at 1 and 2 Da were excluded from quantitative analysis due to uncertainty about whether they originated from residual adsorbed gas in the vacuum chamber. Based on the atom fractions, the measured alloy composition is $Cu_{84.7}Ni_{14.9}$ and contains 21 at. ppm of C, 40 ppm of O, 173 ppm of CO, 835 ppm of NiO, and 0.373 at. % NiH, where the latter three species were ionized as molecular ions. By binning the dataset represented by Figure 2.10c into voxels containing 100 atoms each, frequency distribution analysis of the alloy was performed (Figure 2.12). Accumulation of Cu and Ni towards the dashed peaks evidences the random distribution of the major alloying elements without any noticeable solute nanoclus-

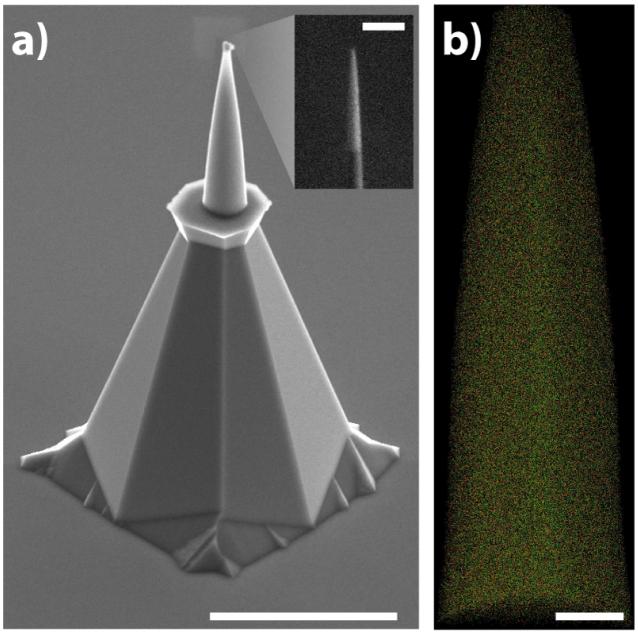

Figure 2.10: Atom probe tomography tip consisting of a Si post with attached HIAM $Cu_{17}Ni_{83}$ specimen prepared by FIB liftout, (a) before and (inset) after polishing. (b) 3D reconstructed point cloud, where orange pixels represent Cu atoms and green pixels represent Ni atoms. Scale bars: (a) 50 μm, inset 500 nm and (b) 20 nm.

ters. The distribution of the other detected species is also randomly distributed throughout the tip, although it is unclear if their quantities are inflated by the field ionization of surrounding or adsorbed gas. Notably, their concentrations exceed equilibrium solubility limits in the FCC Cu and Ni without precipitating noticeable secondary phases, which should warrant a dedicated study to distribution of light elements following reductive annealing.

Through the atomic pair distributions functions in Figures 2.13 and 2.14, the first views of the local atomic environment of HIAM-ed materials before and after reduction is provided without any assumptions of their long-range order. Through a small-box modeling, "real-space Rietveld" approach, we attempt to explore whether the formation of oxides and alloys through HIAM cause local distortions in the average structure that has only been understood thus far in this and previous studies by XRD, EBSD, and TEM [18][22][36]. In all the metallic structures observed, good fits are provided by the real-space Rietveld approach (Figure 2.13). In fact, the fit lattice lattice parameters are able to account for all peak positions through both low and high values of r, indicating that the Cu_xNi_{1-x} alloys are well-ordered without evidence of clustering between metal atoms and/or any solutes present in the structure. Refined lattice parameters range between 3.64, 3.61, 3.59, and

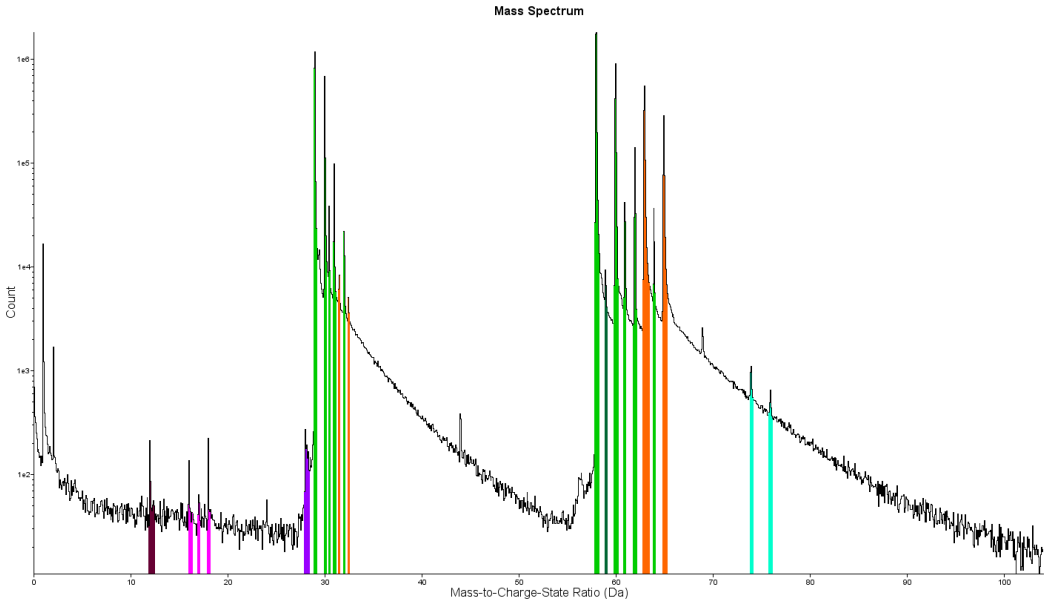

Figure 2.11: Atom probe tomography mass spectrum for $Cu_{17}Ni_{83}$. Identified peaks are Ni (light green), Cu (orange), C (maroon), O (magenta), CO (purple), NiO (teal), and NiH (dark green).

3.54 Åfor Cu, $Cu_{75}Ni_{25}$, $Cu_{50}Ni_{50}$, and Ni respectively in agreement with Vegard's Law. In Figure 2.14, the modeled PDFs of CuO and NiO prepared following their calcination also provide good matches to the experimental PDF, although their agreement are somewhat weaker than in the reductively annealed alloys. In NiO, the single rock salt NiO phase is able to account for all peak positions, but the modeled intensities are systematically under and overestimated. The refinement of the CuO PDF required the fitting of two phases: monoclinic CuO in addition to an 18% phase fraction metallic FCC Cu. However, poor fitting results for the Cu phase using a lattice parameter closer to that of Ni (3.56 Å) uniformly shifted the FCC structure peaks towards smaller r when compared to the experimental PDF and overdamped peaks at high r. In the oxides, models may be improved by accounting for partial site occupancies that would account for discrepancies in intensities due to cation deficiencies in the oxides.

2.9 Isotropic Growth Leads to Equiaxed Grains

We demonstrate a metal additive manufacturing process which can fabricate alloyed parts with complex microstructures by using infused DLP-printed gels as a precursor material. Hydrogel infusion-based additive manufacturing can alloy two or more metals, in this case forming binary alloys with Cu and Ni via grain nucleation and growth processes occurring throughout two thermal treatments (Figure 2.1b-c). The

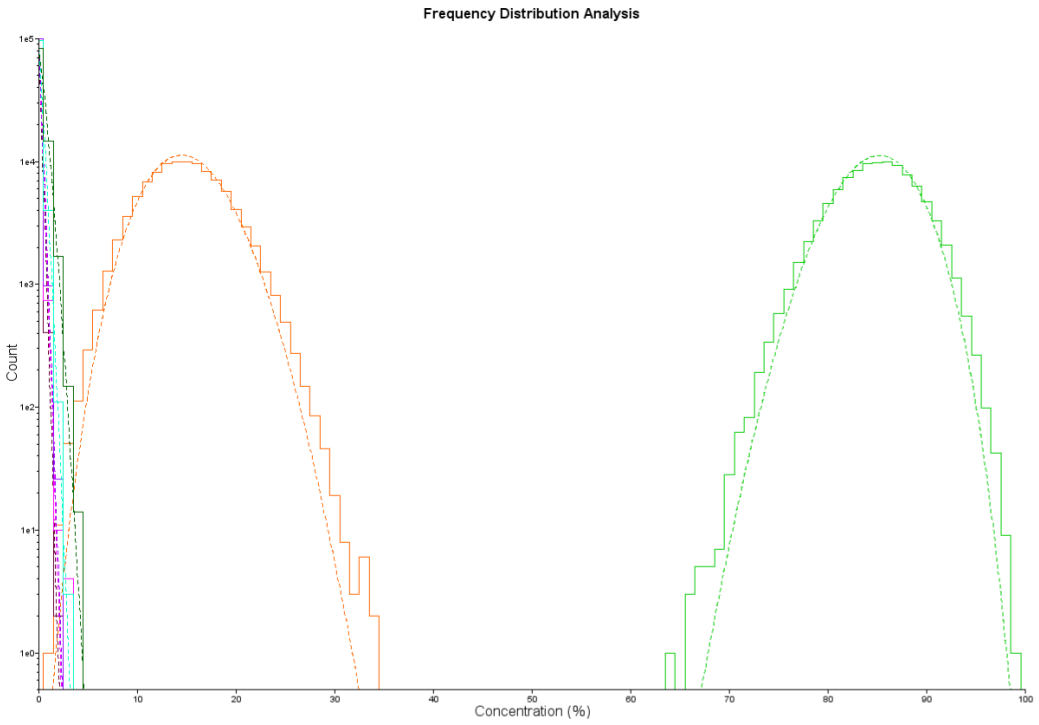

Figure 2.12: Frequency distribution analysis for $Cu_{17}Ni_{83}$ atom probe specimen.

calcination step, typically performed at 700°C and under a controlled atmosphere of 50 sccm compressed air converts the Cu^{2+} and Ni^{2+}-containing gels to porous structures composed of varying proportions of nanocrystalline CuO and NiO [18]. The second thermal treatment, reductive annealing, typically conducted at 900°C under a controlled atmosphere of 150 sccm forming gas (N_2-5% H_2), then reduces the oxide samples to metallic micro-architectures by exposing them to hydrogen gas at high temperatures. The combined kinetics of gas diffusion, solid-state interdiffusion and grain growth serve to produce a broad spectrum of microstructures within a densified alloy (Figure 2.1c), with similar microstructural features despite their complex processing history (Figure 2.4). The resultant multiscale microstructures of HIAM Cu_xNi_{1-x} are discussed below.

As-fabricated HIAM Cu_xNi_{1-x} surfaces exhibit polycrystalline features with well-defined crystal facets (Figures 2.1c and 2.2). EBSD analysis of the polished specimens conveys the produced alloys of all compositions to correspond to a single FCC phase of Cu_xNi_{1-x} (Figure 2.3). Cu_xNi_{1-x} grains are equiaxed and untextured across all compositions with no evident trend between grain size and composition (Figures 2.4a-c(i,ii), Figure 2.6), suggesting isotropic growth of the metallic grains during reductive annealing (Figure 2.4a-c(iii)). The consistency of grain morphol-

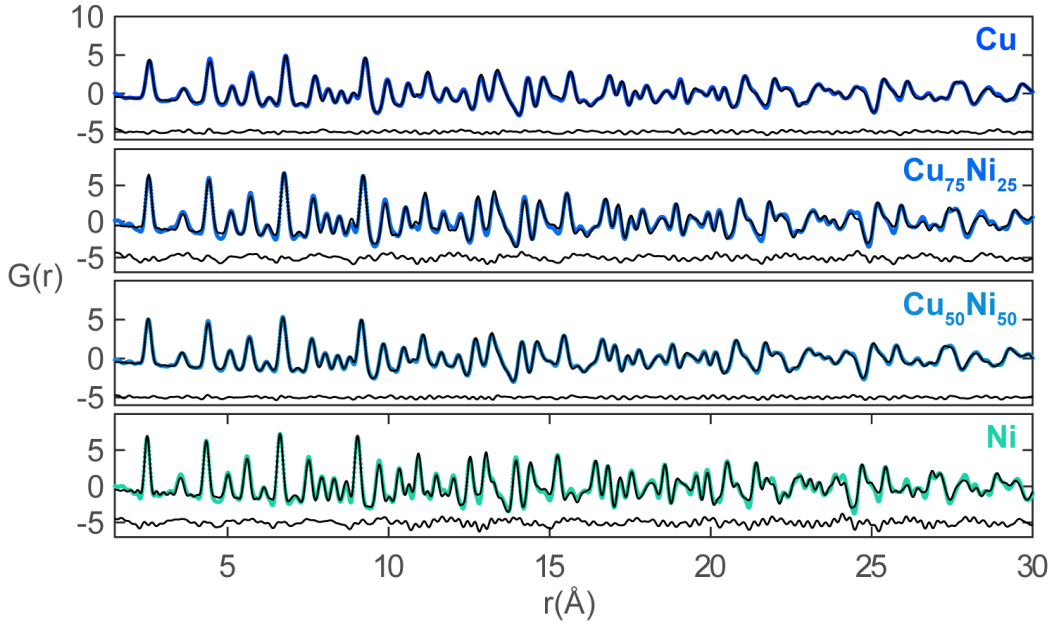

Figure 2.13: Reduced pair distribution function $G(r)$ acquired from total scattering experiments on Cu_xNi_{1-x} fragments prepared by HIAM. Three curves are shown for each composition: the experimental PDF in color, the modeled PDF from real-space Rietveld refinement in black, and the residual function beneath them.

ogy with respect to the alloys' composition arises from the nucleation and growth of the metallic phases, which distinguishes HIAM as a metal AM technique. HIAM-fabricated Cu_xNi_{1-x} alloys generally possess median grain diameters below 4 μm, smaller than those of pure Ni and Cu samples produced using the same process at 4.4 and 15.8 μm, respectively (Figure 2.6). This hints at a slower grain growth rate due to interdiffusion of the two distinct atoms, which does not occur during the reduction of pure oxides.

2.10 Promotion of Annealing Twin Formation

Figure 2.9a-c(iii) and Figure 2.7 illustrate the notably high length density of annealing twin boundaries ($\sim$ 105 m/m^2) as well as of higher-order CSL boundaries in HIAM-produced Cu_xNi_{1-x} alloys. CSL boundaries, which include $\Sigma 3$ twins, compose nearly 60% of the measured boundary lengths for each alloy. The length density of special boundaries in HIAM Cu_xNi_{1-x} are comparable to those of thermo-mechanically processed bulk metals that utilize strain recrystallization specifically to increase density and fraction of special boundaries. Maity et al. reported twin length densities on the order of 10^3 m^{-1} for Ni [37], $Cu_{20}Ni_{80}$, and $Cu_{40}Ni_{60}$, and Cahoon et al. reported the twin densities in annealed cold rolled Ni to be on the

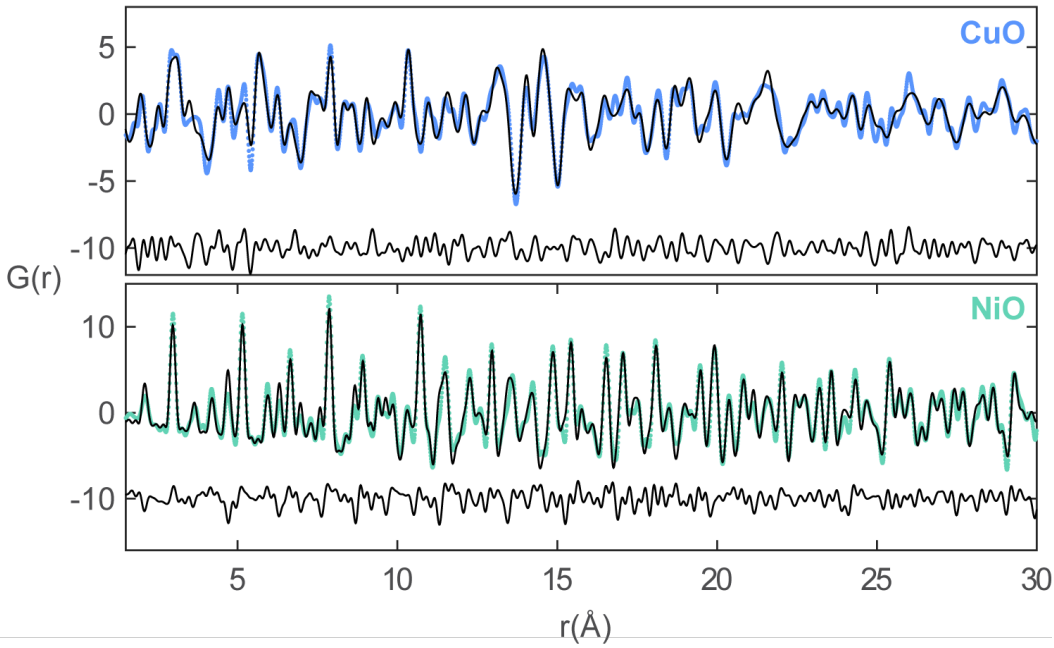

Figure 2.14: Reduced pair distribution function $G(r)$ acquired from total scattering experiments on CuO and NiO powders prepared by HIAM. Three curves are shown for each composition: the experimental PDF in color, the modeled PDF from real-space Rietveld refinement in black, and the residual function beneath them.

order of 10^4 m^{-1} [38]. HIAM Cu_xNi_{1-x} exceeds these values but does not surpass the $> 10^6$ m^{-1} twin boundary length density of nanotwinned Cu, fabricated by pulsed electrodeposition or magnetron sputtering, which drive nanoscale twin formation via the fast deposition of nucleation sites [39][40].

This prevalence of special boundaries in the HIAM samples indicates the existence of another route for twin formation in lieu of mechanical deformation or fast material deposition. In HIAM, growth of reduced metallic nuclei from the atomic to microscale is attained through substantial boundary migration driven by the reduction of grain curvature and high-energy interfaces (i.e., random high-angle grain boundaries). This effect is pronounced for HIAM alloys since the initially reduced alloy grains are small. The driving force for grain growth in the early stages of reduction becomes comparable to that generated by the stored deformation energy in metals prior to strain recrystallization, giving rise to fast grain boundary velocities which make growth accidents and twinning more probable [41]. As atoms migrate towards {111} boundary facets during grain growth, grain boundary motion can nucleate stacking faults bounded by partial dislocations, i.e., Shockley partial loops, whose nucleation on consecutive {111} planes can form annealing twins [41][42].

The fraction and the density of twin and other lower energy boundaries is notably high in HIAM Cu_xNi_{1-x} and independent of chemical composition (Figure 2.7, Table 2.1). This finding stands in contrast to typical intuition from alloying elements with substantial changes in stacking fault energy (SFE) and differences in homologous termpure during processing. A low stacking fault energy (SFE) metal, like Cu ($\gamma_{Cu} \sim 40$ mJ/m^2) [43] stabilizes Shockley partial loops and hence enables greater twin formation within the grains. The addition of an alloying element with moderate SFE like Ni ($\gamma_{Ni} \sim 120$ mJ/m^2) [44] reduces the stability of Shockley partial loops and in turn deters twin boundary formation within the alloy [45]. Additionally, the grain boundary velocity, which controls the rate of growth accidents, is dependent on the homologous temperature of the alloy rather than on the absolute annealing temperature. It can also be slowed by solute drag forces. Given the constant annealing temperature of 900°C used in this work, the combined effects of different homologous temperatures during processing, stacking fault energies, and solute drag forces should act to decrease the twin boundary density in especially Ni-rich Cu_xNi_{1-x}. However, HIAM Cu_xNi_{1-x} remains consistent in its elevated twinning, which suggests that twinning in HIAM alloys is influenced by more complex kinetic factors during processing.

2.11 Diffusive Alloying

It is possible grain boundary migration is dependent on oxide reduction kinetics and limited by additional contributions to drag forces from intermediate HIAM features like vacancies, voids, or unreduced oxide inclusions throughout the alloy. Additionally, diffusion-induced grain boundary motion (DIR) and recrystallization (DIR) are local phenomena that could occur throughout the concentration gradients formed upon the reduction of individual CuO and NiO particles. Already observed in binary alloy systems including Cu_xNi_{1-x} diffusion couples, solute atoms are driven by chemical potential gradients to diffuse into or out of polycrystals and induce grain boundary migration[46][47][48][49][50]. In the wake of the moving grain boundaries, growing grains are enriched or depleted in solute. Moreover, faster diffusion of Cu in grain boundaries compared to Ni leads to a grain boundary Kirkendall effect, where net vacancy flows can lead to pore formation at the grain boundaries and yet also generate stresses causing recrystallization of alloyed grains [46]. The presence of these mechanisms may explain the ability for HIAM to create such chemically homogeneous alloys despite their phase separation as oxides.

2.12 Hierarchical Metal-Oxide Inclusions

The substantive growth of the metallic phase during reductive annealing promotes twin formation but may also impede reduction and lead to the retention of oxides within HIAM alloys. As already-reduced metallic grains coarsen and densify, they encapsulate oxides and locally halt the reduction reaction. Open-pore networks begin to close and trap H_2O vapor, which competes with H_2 for adsorption sites [51][52][53][54]. Reduction then becomes limited by the inward diffusion of H_2 and the outward diffusion of H_2O vapor at an oxide surface. This occurs throughout the AMed parts, slowing the kinetics of reduction at various stages of the reaction to leave behind oxide grains or inclusions of varying size and orientation relationships.

The primary orientation relationship found between the unreduced NiO FCC rock salt grains and the FCC Cu_xNi_{1-x} alloy inclusions in HIAM $Cu_{17}Ni_{83}$ is that of the cube-on-cube orientation relationship, i.e., $(100)_{Cu_xNi_{1-x}} \parallel (100)_{NiO}$ and $[100]_{Cu_xNi_{1-x}} \parallel [100]_{NiO}$, which is not an energetically favorable configuration due to the large lattice mismatch of 18% between the two phases. For growing Cu_xNi_{1-x} inclusions to maintain coherency for such a large lattice mismatch, significant plastic strain must be accommodated via the formation of misfit dislocation arrays, which would be more densely packed and as a result less energetically favorable than other orientation relationships that would minimize the mismatch. This is in contrast to previous studies on analogously structured metal-ceramic systems like epitaxially deposited Ni on MgO substrates, where the orientation relationship $[001]_{MgO}||[1\bar{1}2]_{Ni}$ and $(001)_{MgO}||(11\bar{1})_{Ni}$ was favored over the cube-on-cube orientation relationships due to the minimization of the lattice misfit below 3% from 17% [55]. The cube-on-cube orientation in these systems is metastable, yet they are observed frequently during the reduction of (Me, Mg)O systems [55][56][57][33][58]. It was proposed the orientation relationship arises due to the kinetics of reduction: as oxygen and cation vacancies form during the initial stages of reduction, the metal phase is given enough space to precipitate at those same sites, so the reduction is topotactic; it maintains the crystal orientation of the oxide [55].

The types of inclusions and orientation relationships in the Cu_xNi_{1-x}-NiO system, identified in TEM analysis and summarized by Figure 2.9d, are representative of different stages of reduction. Figure 2.9a shows multiple homogeneously distributed semicoherent inclusions of $Cu_{17}Ni_{83}$ embedded in one larger, unreduced NiO grain. These inclusions are most likely nuclei formed during the early stages of reduction

because they retain their coherency with their parent oxide grains and have not yet grown sufficiently large to break coherency or coalesce. In later stages, as the metallic nuclei continue to grow, they lose coherency with the oxide due to the accumulation of coherency strain with increasing inclusion size and the trapping of produced H_2O. The formation of misfit dislocations at the metal-oxide interface may serve to accelerate the reduction reaction as pipe diffusion mechanisms hasten the diffusion of reactants and products between the interface and free surfaces [59][60]. The later stages of reduction are represented by semicoherent NiO in a Cu_xNi_{1-x} matrix in $Cu_{17}Ni_{83}$ (Figure 2.9b), as well as the formation of incoherent NiO in a Cu_xNi_{1-x} matrix in $Cu_{56}Ni_{44}$ (Figure 2.9c). Voids form from H_2O production. Coarsening of metallic grains forms a matrix surrounding oxide inclusions which may either retain or lose coherency based on their size. The observed coexistence of hierarchical metal-oxide features within HIAM-fabricated Cu_xNi_{1-x} represents kinetically trapped stages of reduction, consistent with those observed in previous kinetics studies of copper and nickel oxide reduction [54][61][62][63][64][65].

2.13 A Note on Diffuse Scattering Observed in SAED

In addition to the double diffraction effects caused by partial reduction (Figure 2.9), we often observed diffuse diffracted intensities in HIAM Cu_xNi_{1-x} SAED patterns among the fundamental FCC reflections (Figures 2.9b, 2.16, and 2.15). Similar observations in literature, particularly for multi-principal element alloy (MPEA) systems like CoCrNi, have been attributed to static displacements by chemical short-range order (SRO) domains [67][68] but has also ignited recent debates over the origin of the diffuse scattering. Walsh et al. summarized explanations besides short-range ordering, including thermal diffuse scattering, planar defects, surface terminations, and dynamical scattering effects [69]. The origin of the diffuse intensities is a curiosity in the HIAM-ed alloys observed because any intensities due to static displacements would imply additional structuring due to HIAM on the atomic scale. However, the positions of most diffuse intensities in HIAM Cu_xNi_{1-x} appear to correspond to those of the higher-order Laue zone (HOLZ) reflections which are less intense because of their substantial deviation from the Bragg condition [66].

The observed diffuse intensities can be understood with an Ewald sphere construction, where a sphere whose radius is formed by the incident wave vector $|\boldsymbol{k_0}| = \frac{2\pi}{\lambda}$ passes through the origin of reciprocal space, and any intersections between the sphere with the reciprocal lattice represents a satisfied Bragg condition (i.e., an observed diffraction spot in the selected area diffraction pattern). For 200 keV

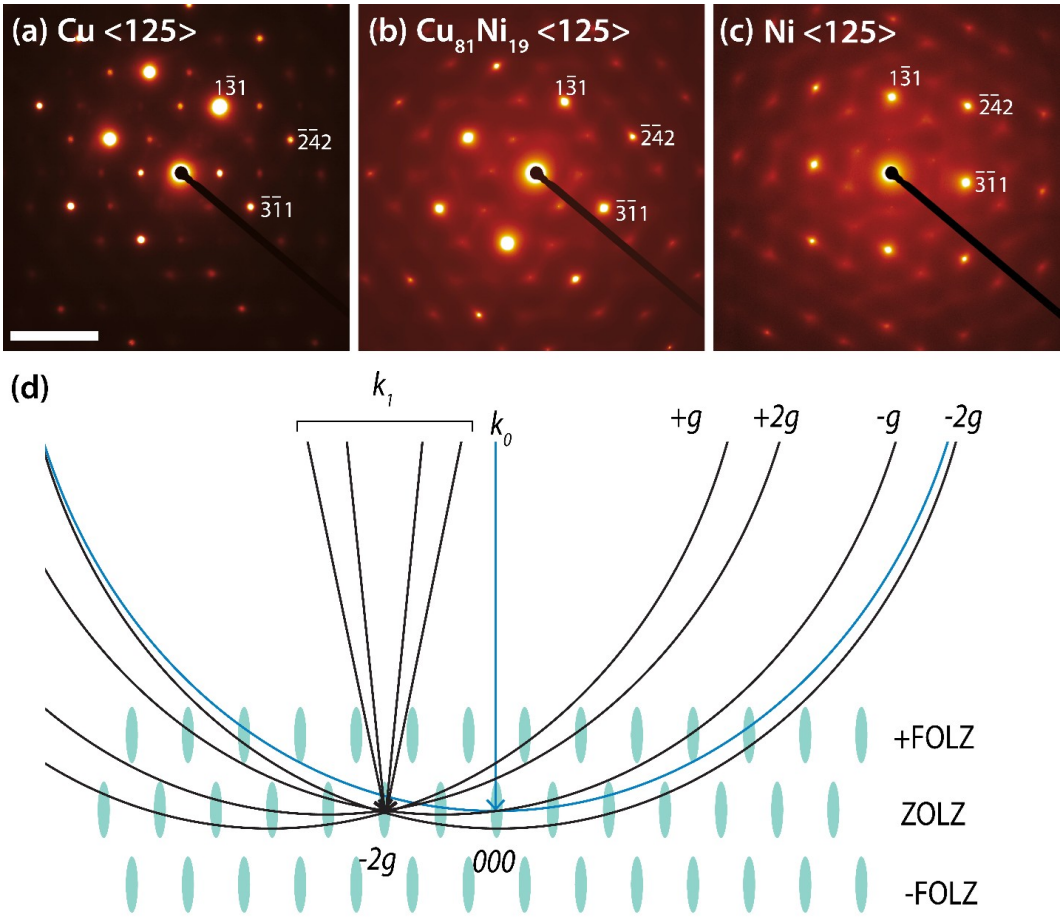

Figure 2.15: Double diffraction results in additional spots and diffuse intensities in SAED. HIAM (a) Cu, (b) $Cu_{81}Ni_{19}$, and (c) Ni SAED patterns contain additional intensities as described by Coury et al [66]. Diffraction spots and diffuse intensities not belonging to the FCC reciprocal lattice oriented along a <125> zone axis are a result of projected higher order Laue zone (pHOLZ) reflections and not oxide inclusions. Scale bar 10 nm^{-1}. (d) Ewald sphere construction schematic indicates how doubly diffracted beams can interact with elongated relrods in reciprocal space to excite higher order Laue zone reflections.

electrons, the small λ leads to a relatively planar surface intersecting a plane of reciprocal lattice points, the zeroth order Laue zone (ZOLZ). However, as the sphere curves upward, it is able to excite higher order reflections outside the ZOLZ. The Ewald sphere is schematically illustrated in Figure 2.15c in two dimensions as a circle intersecting reciprocal lattice rods that can be streaked in real samples due to shape factor effects from finite sample thicknesses. Considering double diffraction was prevalent in Figure 2.9, Figure 2.15c also indicates how doubly diffracted beams denoted by $\boldsymbol{k_1}$ and their secondary Ewald spheres can introduce significant angular deviations based on the Bragg angle and interact with the elongated relrods to excite

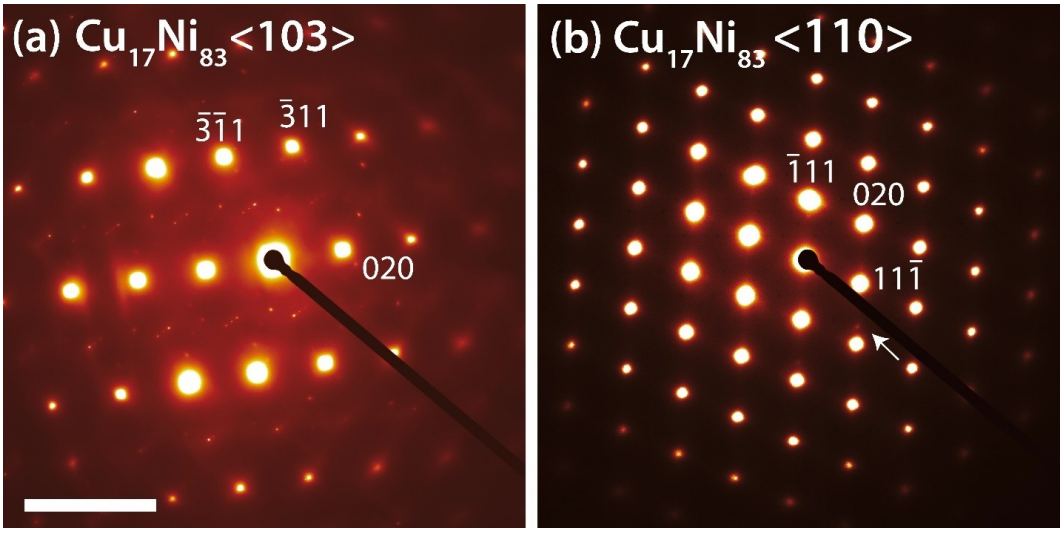

Figure 2.16: HIAM $Cu_{17}Ni_{83}$ SAED pattern while tilted to different zone axes. Additional HIAM $Cu_{17}Ni_{83}$ SAED patterns for metallic grains, featuring additional intensities due to Cux_xNi_{1-x}-NiO composite structure. (a) exhibits diffuse pHOLZ intensities, while (b) sees faint streaks and spots along <111> directions. Scale bar 10 nm^{-1}.

diffuse reflections from higher order Laue zones.

This explains the presence of diffuse intensities even in the unalloyed HIAM Cu and Ni (Figure 2.15a-c). We attribute the extra satellite reflections in high-index zone axis SAED patterns for $Cu_{17}Ni_{83}$ to the double diffraction between reflections from several Cu_xNi_{1-x} Laue zones and NiO (Figures 2.9b and 2.9a). This effect of diffuse projected HOLZ reflections does not explain the faint streaking in $Cu_{17}Ni_{83}$ (Figure 2.9b). Streaks in TEM diffraction patterns are typically indicative of shape factor effects that stretch relrods perpendicular to the habit planes of planar defects or plate-like precipitates. Since the streaks stretch towards $\langle 111 \rangle$ directions, it is likely they are caused by stacking faults or nanotwins which propagate along $\{111\}$ planes in FCC alloys [67][70]. It is also possible that the Cu_xNi_{1-x} alloys exhibit chemical short-range clustering (SRC) as has been observed by Mozer et al., where like atoms begin to segregate into platelets on $\{111\}$ planes due to a miscibility gap [71][72]. Such SRC domains are rarely been observed experimentally because of the extremely slow diffusion rates at low transition temperatures ($< 303°C$) required for alloy decomposition [73]. Furthermore, APT analysis of the same specimen exhibited homogeneous mixing between Cu and Ni without any clustering (Figures 2.10c and 2.12), while PDF analysis provides no indication that the planar defects causing streaks in Figure 2.16 could be formed with high enough density to affect

the average local structure (Figure 2.13).

2.14 Summary of Microstuctures Induced by HIAM

In summary, HIAM is a versatile microscale metal AM approach, which has demonstrated complete control of Cu and Ni alloying through the direct reduction of porous oxide mixtures with hydrogen gas. Oxide-to-metal phase transformations and substantial grain growth during the reductive annealing treatment present unique metal AM process conditions that give rise to a multiscale, hierarchical microstructure. Rapid growth of metallic nuclei into microscale grains drives the formation of low energy interfaces like coincident site lattice (CSL) boundaries, producing densified Cu_xNi_{1-x} with moderately high CSL fractions and twin densities comparable to bulk, thermomechanically processed Cu and Ni. Coalescing metallic grains may also trap oxide grains and prevent their complete reduction, evidenced by extensive double diffraction effects between alloy and oxide phases in the hierarchical nanocomposite structures. HIAM Cu_xNi_{1-x} together possess similar bulk annealed microstructures with comparable grain sizes and twin densities, but nano- and atomic scale defects showcase artifacts due to thermal treatments, including internal nanovoids and partially unreduced structures that contribute to elevated hardness that is seemingly composition-independent.

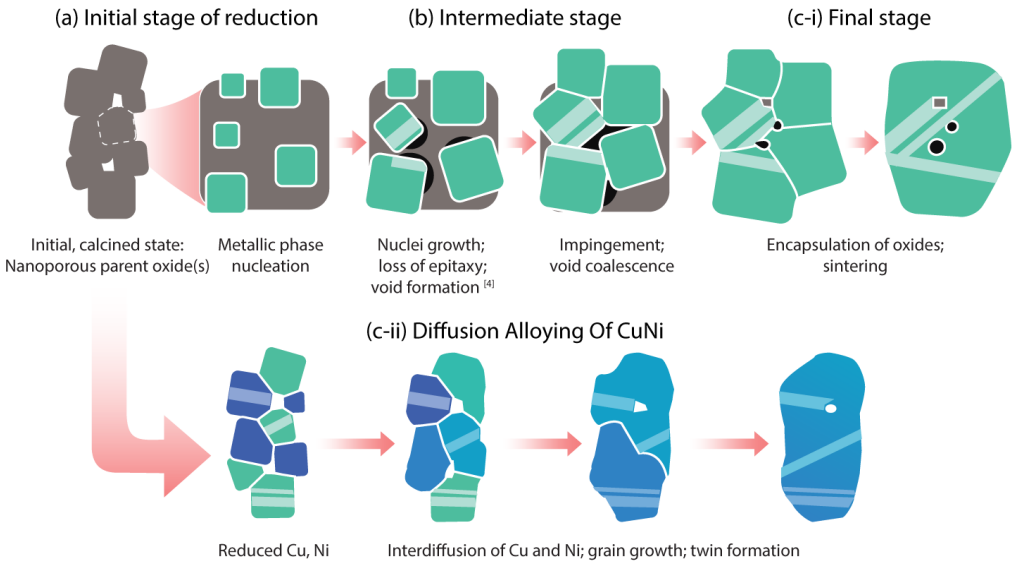

Figure 2.17: Overview of HIAM microstructural evolution during reductive annealing, shown for (a-c(i)) a single phase oxide.

HIAM alloying of Cu_xNi_{1-x} alloy solid solutions is defined by complex metal oxide

reduction kinetics and interdiffusion of locally reduced Cu and Ni regions to drive the formation of a locally homogenized Cu_xNi_{1-x} phase which is greatly twinned but may contain persistent unreduced oxides. Through substantial grain growth, twin formation is energetically favored even for a moderate stacking fault energy metal like Ni. Pervasive coarsening of reduced metal grains additionally form a diffusion barrier to inhibit the reduction reaction inside the AMed parts. This highlights the importance of sample geometry and microstructure prior to reduction. In the early and intermediate stages of reduction, open pores and channels act as a pathway for H_2O to desorb and for the reduction reaction to proceed. These channels can be sealed off during the later stages of reduction to inhibit the reaction. The coarsening of reduced metal forms an encapsulating grain and locks in voids and nanoscale oxide inclusions. Through these simultaneous processes, HIAM Cu_xNi_{1-x} exhibits a unique multiscale microstructure that correspondingly influences their strengthening behaviors.

Chapter 3

INTER- AND INTRAGRANULAR MECHANICAL BEHAVIOR OF HIAM CU_XNI_{1-X}

This chapter has been directly adapted from:

Tran, T. T. *et al.* Multiscale Microstructural and Mechanical Characterization of Cu-Ni Binary Alloys Reduced During Hydrogel Infusion Additive Manufacturing (HIAM). *Small, under review* (2025)

3.1 Introduction

Extensive investigations of microstructure in Chapter 2 discovered several representative key microstructural features in the HIAM Cu_xNi_{1-x} system which were not identified in earlier works on HIAM Cu and CuNi [18][22]. While microscale equiaxed grains with high twin densities were still observed across the entire composition range (Figures 2.6 and 2.7), HIAM Cu_xNi_{1-x} was also observed to contain sparse nanoporosity with unreduced oxide inclusions of varying morphologies, left by diffusion limitations during the reductive annealing process (Figures 2.5, 2.8, and 2.9). However, because of the limited sampling volume in TEM, the spatial distribution of these nanoscale HIAM defects, their compositional dependence, and their resulting impact on mechanical properties remains unclear. These defects may certainly contribute to the anomalous hardening previously reported for Cu and $Cu_{55}Ni_{45}$ [18], but it is unknown what their relative contributions to hardness are compared to other microstructural features like grain boundaries and twin boundaries.

To supplement the microstructure characterization and further resolve the connection between observed microstructures and properties in HIAM Cu_xNi_{1-x}, Chapter 3 takes a multiscale approach to micromechanical characterization to clarify the role of the various microstructural elements in dictating mechanical properties. Nanoindentation is first used to sample the hardness of the collective microstructure, which includes the effects of interfaces. Then, site-specific micropillar compressions are used to dissect and isolate strengthening mechanisms of intragranular HIAM-induced defects. Through the mapping of intergranular and intragranular response

in the Cu_xNi_{1-x} space, this chapter aims to determine the variability and impact of HIAM defects on the mechanical performance of fabricated alloys.

Boundary-Mediated Strengthening in HIAM Cu_xNi_{1-x}

Developing an understanding of individual microstructural features' contributions to hardness and strength requires the interpretation of results through established models for strengthening. In metallic systems, many strengthening mechanisms are derived from interactions between moving dislocations and microstructural obstacles. A well-known example is that of the empirical Hall-Petch relation,

$$\sigma = \sigma_0 + kd^{-1/2}, \tag{3.1}$$

where σ is the measured strength of a metal, σ_0 is its intrinsic strength, k is a scaling constant dependent on chemistry, and d is the average grain diameter. Also applied to indentation hardnesses, the Hall-Petch relation describes the dependence grain size to a metallic polycrystal's strength [74][75]. As dislocations move during deformation, they typically fail to transmit through grain boundaries and pile up. The system continues to carry increasing stress until the accumulated back stress felt by an adjacent grain activates dislocation sources and enables further plastic deformation. As grain sizes decrease, the density of the boundaries increases and hardens the material as a result.

Previous treatments attempted to relate the microstructural features of HIAM Cu and $Cu_{55}Ni_{45}$ tried to attribute enhancements in nanoindentation hardness to a modified Hall-Petch model which accounted for the strengthening due to twin boundaries (Figure 3.1) [18][76][22]. An effective grain size $d_{eff} = d(1 + pN)$ was defined, scaling the average grain size by the average number of twins per grain N and its effectiveness as a barrier to slip p [76][77]:

$$H = H_0 + k\left(\frac{d}{1 + pN}\right)^{-1/2}. \tag{3.2}$$

Because additional CSL boundaries were also discovered to occur frequently in the HIAM system, Equation 3.2 could be expanded to account for their resistances to dislocation motion as well for i types of boundaries.

$$H = H_0 + k\left(\frac{d}{\sum_i 1 + p_i n_i}\right)^{-1/2}. \tag{3.3}$$

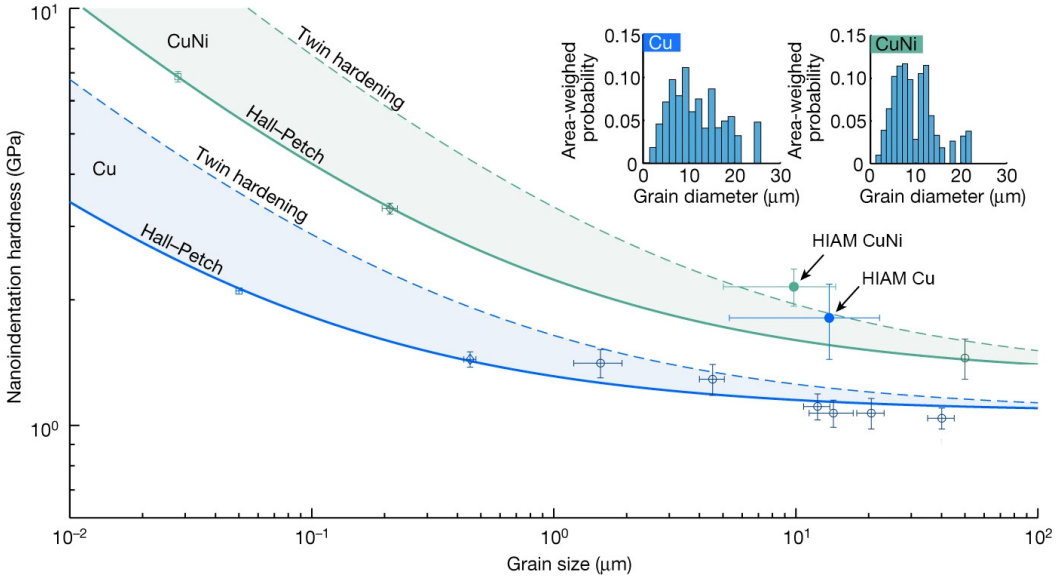

Figure 3.1: Nanoindentation hardness of HIAM-fabricated Cu and CuNi samples is higher than predicted based on Hall–Petch scaling (dashed lines show calculated twin-induced hardening). Error bars show standard deviations of grain size and nanoindentation hardness. Insets: area-weighted grain size distribution for Cu and CuNi. Literature data are reported from [78][79][80][81]. Reproduced with permission from Springer Nature [18].

However, despite the prevalence of twin and CSL boundaries in HIAM Cu and $Cu_{55}Ni_{45}$, authors noted the inability for the anomalous hardening to be explained by boundary-mediated hardening. The assumption of $p = 1$ treated all detected boundaries' effectivenesses as dislocation barriers as equivalent to that of randomly oriented grain boundaries, and the upper bound formed by the assumption still underestimated the performance of HIAM Cu and $Cu_{55}Ni_{45}$ (Figure 3.1) [18][76].

Other Sources of Strengthening

The discovered microstructural complexity of HIAM Cu_xNi_{1-x} complicates efforts to isolate dominant strengthening mechanisms. During deformation, moving dislocations do not only interact with barriers like grain boundaries, twin, and CSL boundaries. Concurrently, they may encounter additional lattice-scale obstacles via defects like pre-existing dislocations, nanoscale oxide inclusions, porosity, and solute atoms. Each feature contributes to strength differently through different mechanisms such as Taylor hardening, precipitate strengthening, and solid solution strengthening. Furthermore, as testing volumes (such as those of micropillars) decrease in size, yield or flow strength can increase for micro- and nanoscale specimens due to changes in their plasticity mechanisms [82]. This is the "smaller is stronger"

size effect which is extrinsically controlled by the sample size biasing of dislocation source lengths and operation stresses. As pillar dimensions decrease, mechanisms for strain hardening transition between collective dislocation interactions to dislocation source-limited behavior. Fewer available dislocations lead to a regime where deformation is governed by dislocation interactions with solute atoms, as well as the HIAM-induced defect landscape that would change the sample's capacity for dislocation storage. As a result, the micropillar compression of HIAM Cu_xNi_{1-x} can be used to both physically excise the effects of boundary strengthening and probe dislocation interactions with solutes and intragranular defects generated by HIAM as a whole.

3.2 Nanoindentation

Load-controlled nanoindentation experiments were conducted on epoxy-mounted and polished samples with a diamond Berkovich tip after performing calibrations on fused silica standards to obtain the instrument frame stiffness and tip area (Agilent Nano Indenter G200). The area indented by the Berkvovich geometry as a function of the contact depth h_c is described following area function:

$$A(h_c) = 24.5h_c^2 + 4794.96h_c - 122952h_c^{1/2} + 444778h_c^{1/4} - 314406h_c^{1/6}. \quad (3.4)$$

Nanoindentation experiments on Cu_xNi_{1-x} were performed at a loading rate $\dot{P} = 0.05$ s^{-1}. An indentation depth 500 nm was chosen in order to sample the mechanical response of the samples' intrinsic microstructures resulting from reductive annealing, including grain and twin boundaries whilst avoiding hardening due to indentation size effects. Polishing procedures were the same as those outlined for EBSD sample preparation. At least 10 indent sites were chosen along wall interiors and nodes, with any adjacent tests performed at least 5 μm away from each other to avoid indenting previously deformed areas. The continuous stiffness measurement (CSM) option was used to monitor hardness and stiffness as a function of depth and filter out outlier tests due to poor contact with the specimens. Reported hardnesses are the mean hardnesses measured for unique samples across multiple indents, each averaged between indentation depths of 300 and 400 nm during CSM. Error bars represent ±1 standard deviations.

3.3 Site-Specific Micropillar Fabrication and Orientation Analysis

A Ga^+ Focused Ion Beam microscope (FEI Versa3D Dual Beam) was used to machine micropillar compression specimens by milling concentric annulus patterns

atop the HIAM-produced honeycomb specimens. Prior to milling, regions of interest previously orientation mapped via EBSD were imaged with FIB ion channeling contrast at low currents (≤10 pA) to minimize surface damage. The FIB images were then correlated with the orientation maps to select large grains with known crystallographic orientation given via Bunge notation (ϕ_1, Φ, ϕ_2) (Figure 3.2a,b). The Bunge Euler angles ϕ_1, Φ, and ϕ_2 are defined as the sequential rotations of a crystal around its reference frame's (1) Z-axis, (2) rotated X-axis after the first rotation, and (3) rotated Z-axis after both rotations, respectively. The crystallographic orientation in Miller indices $(hkl)[uvw]$ is described as the positions of the reference frame's Z and X axes after the rotations, which are columns of the combined rotation matrix. The plane indices are as a result:

$$h = n \sin\Phi \sin\phi_2, \tag{3.5}$$

$$k = n \sin\Phi \cos\phi_2, \tag{3.6}$$

$$l = n \cos\Phi, \tag{3.7}$$

where n is a factor to make h, k, and l integer values. At 30 kV, large beam currents up to 1 nA were used to mill large craters greater than 15 μm in diameter for the clearance of the $\sim 10\mu m$ flat punch tip used for compression. Then, smaller beam currents of 10 pA were used to remove as much taper as possible (until $< 5°$) from each pillar and minimize FIB-induced artifacts. Pillar diameters were varied between approximately 400 nm and 3 μm, with height-to-diameter aspect ratios of $\sim 2.5 - 3$ (Figure 3.2c).

With the orientation of each single crystal pillar known, it is also possible to calculate how well-oriented the crystal is for slip through the relative positions of its slip systems. Since the Cu_xNi_{1-x} system is a single-phase FCC crystal, it contains 12 slip systems consisting of four {111} planes with three slip directions <1$\bar{1}$0> each. Schmid's law states that slip will initiate when the resolved stress τ on a slip system exceeds a critical value τ_c. The resolved stress is defined as

$$\tau = \sigma \cos\phi \cos\lambda = \sigma \cdot m, \tag{3.8}$$

where σ is the applied stress, ϕ is the angle between the slip plane normal and the direction of the applied stress, and λ is the angle between the slip direction and the direction of the applied stress. The cosine factors are commonly denoted together

as m, the Schmid factor. Ranging between values of 0 and 0.5, the Schmid factor is minimized when the direction of the applied stress is perpendicular to either the slip plane or the slip direction, and it is maximized when direction of the applied stress is oriented 45°relative to both the slip plane and slip direction. For an arbitrarily (hkl)-oriented FCC micropillar, the compressive loading direction is along the corresponding direction $[hkl]$, and 12 Schmid factors can be calculated for each individual slip system. Since slip systems with the highest resolved shear stress deform first, it follows from Equation 3.8 that the slip systems with the maximum Schmid factor will initiate plastic yield in a single crystal micropillar. Generally, pillars oriented along low-index crystallographic directions possess several slip systems with equivalently high Schmid factors leading to slip in multiple slip systems, while those oriented along high-index directions may only have one slip system with a uniquely high Schmid factor, leading to single slip.

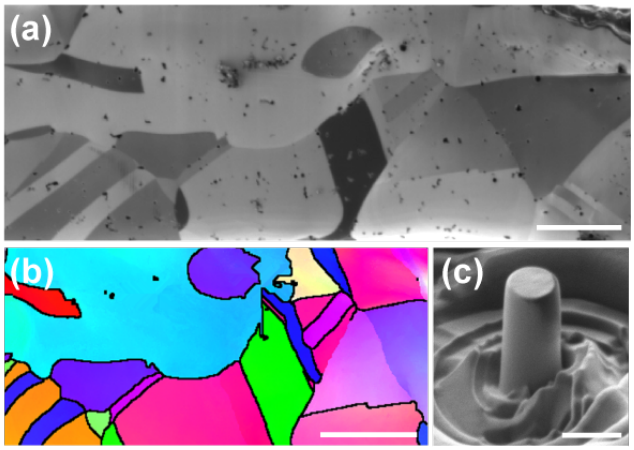

Figure 3.2: Site-specific $Cu_{78}Ni_{22}$ fabrication based on EBSD orientation mapping. By correlating (a) FIB ion channeling contrast images with (b) orientation maps of HIAM honeycomb specimens, (c) micropillars can be FIB machined from individual grains of known orientation in the HIAM-ed polycrystal. Scale bars (a, b) 10 μm and (c) 1 μm.

3.4 In Situ Uniaxial Micropillar Compression

In situ uniaxial compression experiments were performed by a custom setup inside a SEM (FEI Quanta 200F) featuring a nanoindenter with a 10 μm-diameter diamond flat punch tip installed (InSEM, Nanomechanics Inc.). Displacement-controlled loading is achieved with the load-controlled indenter by applying a feedback loop. Compression tests were conducted to nominal strains of 20% at strain rate $\dot{\epsilon} = 10^{-3}$ s^{-1} using the CSM option.

Raw data is output as load-displacement data, which is converted to true stresses and strains following the analysis described in [83]. Deformation due to the compliance of the substrate and indenter tip during the compression experiments are subtracted with the Sneddon correction, which corrects for the displacement of a flat-ended cylinder into an elastic half-space (i.e., the deformation caused by the FIB-ed micropillar specimen acting as a cylindrical indenter against its substrate of the same material and the diamond flat punch indenter tip). The Sneddon compliance is given as

$$C = \frac{1 - \nu^2}{2Er}, \tag{3.9}$$

where ν is the Poisson's ratio, r is the contact radius, and E is the Young's modulus of the indenter and the substrate [84][83][85][86]. Consequently, the displacement of the micropillar specimen during compression is

$$u_{pillar} = u_{tot} - \frac{(1 - \nu^2_{substrate})P}{2E_{substrate}r} - \frac{(1 - \nu^2_{indenter})P}{2E_{indenter}r}, \tag{3.10}$$

where the displacement u_{tot} and load P are measured during the compression experiments, the contact radius is the measured pillar radius, the substrate material properties are those of polycrystalline Cu_xNi_{1-x}, and the indenter material properties are those of diamond [83][87].

True stress is converted to resolved shear stress using the corresponding pillar's maximum Schmid factor calculated from EBSD analysis (Equation 3.8). Lastly, to plot the yield stress or the critically resolved shear stress as a function of pillar diameter, the critical resolved shear stress values are found by identifying the stress where the shear stress—true strain plot deviates from its linear-elastic regime. Most times this is the first strain burst following contact with the top of micropillars, which is identified based on the in situ videos and analysis of stiffness—displacement plots obtained through CSM.

3.5 Composition-Independent Hardening

To assess the mechanical properties of HIAM-produced Cu_xNi_{1-x}, we conducted nanoindentation and uniaxial micropillar compression experiments (Figure 3.3). Figure 3.3a shows the average hardness of unique HIAM-fabricateded samples across the entire alloy composition range from pure Ni to pure Cu. The hardness is calculated as

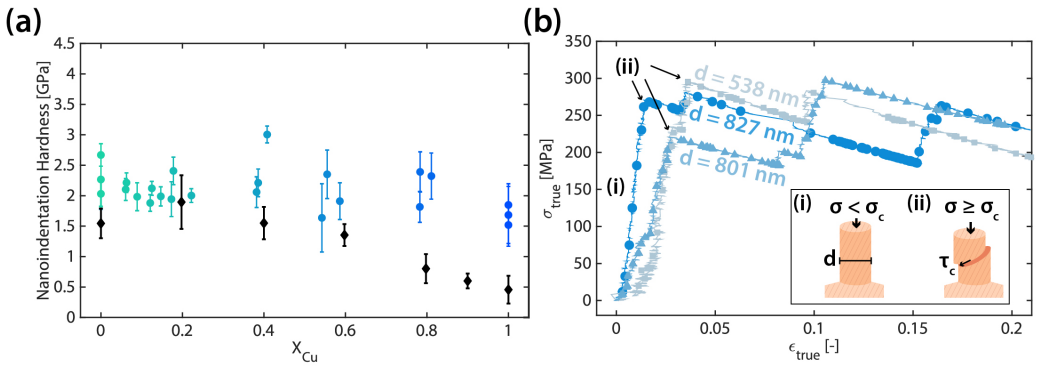

Figure 3.3: Micromechanical Behavior of HIAM Cu_xNi_{1-x}. (a) Average nanoindentation hardness, calculated from (Equation 3.11), as a function of composition plotted in comparison to reported literature values for Cu_xNi_{1-x} compositions with similar grain sizes [81]. (b) Representative uniaxial compression results performed on single crystal micropillars of HIAM $Cu_{59}Ni_{41}$ with shown diameters: (i) elastic loading regime and (ii) first major strain burst. Because the pillars are milled from randomly oriented grains within the HIAM-fabricated sample, the critical resolved shear stress is calculated by multiplying the critical stress at which the first major strain burst occurs, (ii), by the maximum Schmid factor derived from EBSD measurements (Equation 3.8).

$$H = \frac{P_i}{A_i}, \tag{3.11}$$

where P_i is the load and A_i is the contact area for a diamond Berkovich tip at a given indentation depth i. In this study, each hardness measurement is averaged between depths of 300 and 400 nm during depth-sensing measurements, after hardening from the indentation size effect subsides. Each data point represents the mean hardness of a unique HIAM alloy specimen, and their error bars represent the range of hardnesses defined by ±1 standard deviation. The data set denoted by black diamond symbols represents the hardness reported in Bahr et al. for diffusion alloyed Cu_xNi_{1-x} formed by commercially pure alloys, Cu, and Ni with a grain size of approximately 50 μm [81]. While the literature values exhibit a peak hardness for Ni-rich compositions, greater than that of pure Cu and Ni due to solid solution hardening, HIAM Cu_xNi_{1-x} demonstrates hardness values that are consistently high throughout the compositional range. Pure HIAM Ni and Cu show 73% and 305% increases in nanoindentation hardness relative to [81], and the largest hardness amplification for HIAM Cu_xNi_{1-x} alloys occurs for $X_{Cu} \leq 0.4$. Nominally 80 at.% Cu samples exhibit the largest amplification in hardness of ~198%, which corresponds to 1.6 GPa. For Ni-rich alloys, i.e 5-20 at.% Cu content, the hardness

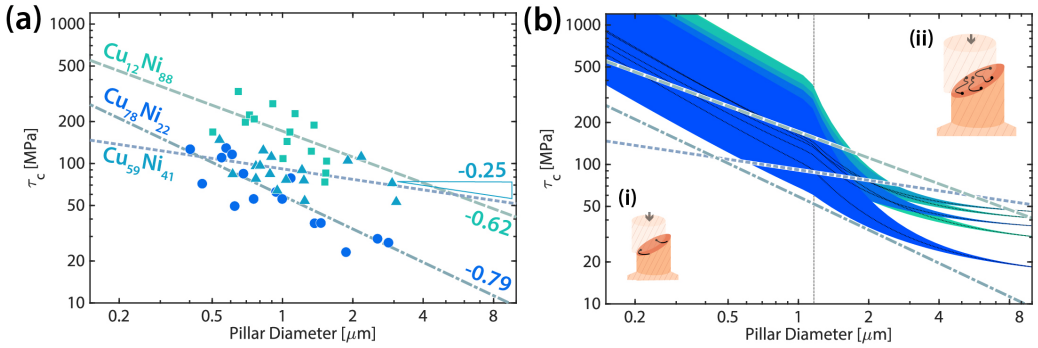

Figure 3.4: Probing intragranular plasticity of HIAM Cu_xNi_{1-x} with the "smaller is stronger" size effect. (a) Critical resolved shear stress (τ_c) vs. pillar diameter results from micropillar compression experiments show a "smaller is stronger" size effect with power-law scaling exponents that vary with composition. (b) Fit lines from (a) plotted against Cu, Ni, and Cu_xNi_{1-x} (x = 12, 59, 78) solid solutions' estimated strength ranges (mean ± 2 standard deviations) predicted by a modified stochastic source length model (Equation 3.14) for an assumed initial defect density. While $Cu_{12}Ni_{88}$ and $Cu_{78}Ni_{22}$ alloys possess scaling exponents nearing that of the (i) small pillar regime where strengthening is dominated by source operation, the suppressed scaling of the near-equiatomic $Cu_{59}Ni_{41}$ alloy suggests behavior representative of (ii) large pillars where strengthening is dominated by dislocation interactions with solutes, dislocations, and other intragranular defects including oxide inclusions.

remains comparable to the results of Bahr, et al. and is virtually constant with differences of less than 27% around 2.00-2.25 GPa [81].

To probe intragranular mechanical behavior in HIAM-fabricated alloys, we FIB-milled cylindrical, single crystalline pillars of varying diameters from large grains of as-fabricated polycrystals whose orientations were determined via EBSD (Figure 2.4(a)). Electron channeling contrast confirmed these pillars to be free from grain boundaries or twin boundaries. Pillars were compressed using a 10 μm diameter diamond flat punch tip under a displacement-controlled strain rate of 10^{-3} s^{-1}. During the compression experiments, load vs. displacement data was obtained (Movies S1-S3) and converted into true axial stresses and strains using

$$\sigma = \frac{P}{A_p} \tag{3.12}$$

and

$$\epsilon = \frac{\sigma}{E} - ln\frac{L_p}{L_0}, \tag{3.13}$$

where P is the compressive load, A_p and L_p are the cross-sectional area and height of the pillars during compression, L_0 is the pillar height prior to compression, and E is the elastic modulus of Cu_xNi_{1-x} in the loading orientation. Calculations for the deformed pillars' dimensions assume volume conservation as in [83]. Once axial stresses are calculated, they are converted to shear stresses on the slip system with the maximum resolved shear stress by multiplying them by the maximum Schmid factor determined from EBSD data (Equation 3.8).

3.6 Observation of Suppressed Size Effect

The critical resolved shear stress (CRSS) of Figure 3.4a is determined by taking the resolved shear stresses where the first major strain burst occurs (Figure 3.3b(ii)) due to slip events (Movies S1-3). The pillars' CRSSes vary with composition and pillar diameter. CRSS vs. pillar diameter plots for representative compositions of Ni-rich ($Cu_{12}Ni_{88}$), equiatomic ($Cu_{59}Ni_{41}$), and Cu-rich ($Cu_{78}Ni_{22}$) alloys show that each alloy exhibits a "smaller is stronger" size effect characterized by a power law scaling exponent m, i.e.,

$$\tau_c \propto d^m, \tag{3.14}$$

where τ_c is the critical resolved shear stress and d is the pillar diameter. They each display shear strengths greater than yield strengths for Cu_xNi_{1-x} at bulk scales [88][89][90]. Cu-rich and Ni-rich alloys scale as m~-0.79 and m~-0.62 respectively. These values align with reported size effects in pure FCC metals including Cu and Ni (m~-0.6 to -1.0) [91][92]. The near-equiatomic alloy, $Cu_{59}Ni_{41}$, exhibits a much weaker scaling exponent of -0.25 despite possessing the same crystal structure as the pure metals. Weaker scaling exponents are reported for systems with greater internal resistance to dislocation motion such as body-centered cubic metals and precipitation-hardened Al alloys [93][94].

3.7 HIAM's Influence on Mechanical Properties

To understand the role of these multiscale microstructural features in the mechanical performance of the HIAM alloys, we employ nanoindentation (Figure 3.3a) and compression of FIB-milled single crystalline micro- and nano-pillars (Figure 3.3).

Nanoindentation results indicate high hardnesses between 1.5 and 3 GPa in the HIAM-produced alloys, consistent with Saccone et al.'s measurements for HIAM Cu and $Cu_{55}Ni_{45}$ [18]. At the indentation depths of 500 nm, the indents probed the

collective response of various microstructural features, including the grain boundaries, coincident site lattice (CSL) boundaries, and unreduced features shown in Figures 2.4 and 2.8. Variation in the features sampled by the indents introduces localized hardening and softening, contributing to the large reported standard deviations (Figure 3.3a). Nevertheless, the full compositional range in HIAM Cu_xNi_{1-x} features elevated average hardness, so hardening is prevalent regardless of composition. Since Figure 2.4 revealed that the HIAM-produced specimens are primarily random substitutional solid solutions with similar grain sizes and twin densities (Figures 2.6 and 2.7), composition-dependent hardening is expected due to contributions from both solid solution and Hall-Petch hardening. Interactions between mobile dislocations and solute atoms, via size misfit and local variations in the elastic modulus, as well as their pile-ups at the grain boundaries, would lead to the greater indentation flow stresses for more Ni-rich Cu_xNi_{1-x} alloy [88][89][95][96][97][98][99]. The observed distinct separation of HIAM hardness from other nanoindentation experiments on Cu, Ni, and Cu_xNi_{1-x} suggests that it is caused by a different mechanism, possibly through the elastic interactions between densely distributed lattice defects or via unusual strengthening at the boundaries [81][95].

3.8 Modified Stochastic Source Length Model for Solid Solutions

To better investigate potential sources of strengthening in the constituent material, we conducted uniaxial micropillar compression experiments to isolate the mechanical response of individual grains and their lattice-scale defects (Figure 3.3b). The plot in Figure 3.4b compares the experimentally measured micro pillar compression strengths to the predictions of a simple stochastic source length model [100], which we modified to include a term for Labusch binary solid solution strengthening:

$$\tau_{CRSS} = \tau_0 + \frac{Gb}{2}\sqrt{\rho_{tot}} + \frac{\alpha G b}{\bar{\lambda}} + kc^{2/3}, \tag{3.15}$$

where $\bar{\lambda}$ is the average source length, G is the shear modulus, b is the magnitude of the Burger's vector, ρ_{tot} is the initial dislocation density in the specimen, α is a geometrical term taken to be unity, k is a pre-factor including both size and modulus misfit terms as described by the Labusch solid solution strengthening model, and c is the concentration of the solute element [96]. G and b are assumed to vary linearly with the Cu_xNi_{1-x} concentration, and k values are taken from fits to single crystal tension experiments for Cu_xNi_{1-x} [88][89]. Calculations for λ follow those of Parthasarathy et al. [100], using a pillar aspect ratio of 2.5 and a ρ_{tot} of $2{\times}10^{12}$

m^{-2}.

The model still contains two distinct size-based regimes for Cu_xNi_{1-x} alloys bounded by the vertical line (Figure 3.4b). The strengthening of smaller pillars are controlled by dislocation source nucleation and has a constant power law scaling of ~-1.0 (Figure 3.4b(i)); in larger pillars it is dominated by the solute-dislocation interactions and a scaling that gradually weakens to ~-0.4 as a function of pillar size (Figure 3.4b(ii)). The strengths of smaller pillars appear proportional to their solute concentration, increasing with Ni content; while in the larger pillars, the alloys always outperform those of pure Cu and Ni. As the availability of dislocation sources becomes limited by sample dimension, the dominant strengthening terms in Equation 3.15 shift from solid solution strengthening in the large pillar regime to source operation in the small pillar regime. This is consistent with Bahr & Vasquez's findings that the solute atoms in a binary solid solution amplify stresses required for dislocation propagation but not for nucleation [81]. The critical transition between the two size regimes and their respective plasticity mechanisms remains at the same position through all Cu_xNi_{1-x} compositions, assuming similar initial defect densities. However, if the defect densities are varied, the transition can shift towards smaller or larger dimensions [101][102]. For example, materials with reduced dislocation densities could drive the critical dimension towards larger pillars.

In contrast, the model overpredicted the strengths of HIAM $Cu_{59}Ni_{41}$ and $Cu_{78}Ni_{22}$ (Figure 3.4b). Results show that the pillars with near-equiatomic composition are weaker than the range defined by ±1 standard deviation below diameters of 1 μm, while the strengths of all Cu-rich pillars fall below even the range defined by pure Cu. Unlike the nanoindentation results, which convey universally elevated hardnesses in HIAM Cu_xNi_{1-x}, micropillar compressions on single crystals of the tested compositions indicate both strengthening and weakening for the largest pillars where the contribution of strengthening due to extrinsic size effects is reduced. While any nanoscale defects emerging from HIAM processing together with interfaces may pin dislocations during nanoindentation and lead to indiscriminate hardening, their variation in strength under uniaxial compression reveals how their scope varies with alloy composition. Their size and distribution can be indirectly represented by their effects on the size effect scaling, which varies based on pillars' internal microstructures.

3.9 Effect of Internal Microstructures in Micropillars

The Cu-rich and Ni-rich compositions follow scaling behavior common to FCC metals (-0.6 to -1.0), the near-equiatomic composition shows an unexpectedly low size scaling exponent of -0.25 [91][92]. This suppression in size effect has been observed in pillars that contain additional microstructural features. Micropillar studies on duralumin, a precipitation-hardened Al alloy, indicate that the introduction of precipitates can diminish the size effect scaling observed in pure Al [94]. Gu et al. compared room temperature (RT) aged duralumin pillars, where the dominant length scale was determined by the spacings between densely distributed Guinier-Preston zones and Cu-Mg clusters, to peak-aged pillars which contained more sparsely distributed θ' precipitates [94]. The RT-aged samples showed greater suppression of the size effect (m~-0.34) when compared to peak-aged samples (m~-0.51). Similarly suppressed size effects have been observed in micropillars of oxide dispersion-strengthened steel as spacings between the oxide dispersions and dislocation cell walls become the dominant microstructural length scale [103][104]. These results indicate that the internal nanoscale features in the HIAM alloy samples in this work, like those discussed in relation to the streaking of spots in electron diffraction observations, dominate the critical dimensionality for size scaling and a decrease in the scaling exponent.

Based on the various composite microstructures observed via TEM (Figures 2.8 and 2.9), it is also plausible that the variation in strength and size effect scaling of HIAM Cu_xNi_{1-x} emanates from the varying initial densities of reductive annealing artifacts, such as internal pores and unreduced oxide nano-inclusions. Specimens concentrated with HIAM defects can inhibit dislocation propagation, causing strengthening while pushing the plasticity mechanism transition towards smaller diameters, thereby assuming a suppressed size effect that is represented by the scaling in the large pillar regime in Figure 2.9c. This is a possible explanation for the behavior of the near-equiatomic $Cu_{59}Ni_{41}$ alloy pillars. Conversely, specimens exhibiting larger scaling exponents representative of source-controlled plasticity maintain a lower initial density of lattice defects because they are more reduced or densified than $Cu_{59}Ni_{41}$. However, defects greater in breadth (i.e., larger pores allowed to coalesce) surviving reductive annealing may weaken pillars, as is the case in $Cu_{78}Ni_{22}$.

3.10 Summary: Linking HIAM Defects to Micromechanical Behavior

Since the large plastic zone of nanoindentation cannot distinguish between hardening caused by the unusual boundary strengthening vs. the high lattice defect densities, the site-specific micropillar compression experiments allow the isolation of individual grains' contributions to the mechanical response in HIAM Cu_xNi_{1-x}. Relative to the model for extrinsic size-dependent strengthening of binary alloy pillars, Cu-rich pillars possess weak shear strengths. Also, the near-equiatomic pillar strengths show a suppressed size effect compared to literature values for pure FCC metal pillars. Compositionally dependent nanomechanical behaviors paint a more nuanced picture of reductively annealed microstructures in HIAM. Respectively, they may suggest a greater breadth of fabricated defects in Cu-rich compositions, generally weakening the alloy, or greater initial defect densities in the near-equiatomic composition, where the formation of an internal microstructure deters the source-controlled behavior commonly reported in studies of single crystal FCC pillars. These defects vary in extent and frequency based on differences in each alloy's microstructural evolution and are likely to be the internal pores formed from H_2O formation during reduction or the disperse unreduced oxides from incomplete reduction. Despite causing notable differences in nanomechanical behavior, they each give rise to high hardnesses in nanoindentation.

Chapter 4

TOWARDS HETEROGENEOUS ALLOYS USING HIAM

This chapter has been directly adapted from:

Tran, T. T. *et al.* Oxide-Dispersion Strengthened Alloys Printed via Hydrogel Infusion-Based Additive Manufacturing (HIAM). *In preparation* (2025)

4.1 Introduction

Material Selection in HIAM Depends on Reducibility

Hydrogel infusion-based additive manufacturing has broadened the compositional space achievable by additive manufacturing technologies through its chemical reduction pathway. By avoiding the direct use of metals as feedstock materials, HIAM circumvents issues like high thermal conductivity materials limiting spatial resolution, high melting temperatures avoiding melting, and feedstock material deterioration leading to deleterious properties in the built part. However, different sets of issues arise for HIAM-based metal additive manufacturing. Materials selection is instead limited to metals that are available as water-soluble salts. In addition, after calcination, they must form oxides that are reducible by hydrogen gas. This precludes particularly stable metal oxides like alumina (Al_2O_3), magnesia (MgO), and titania (TiO_2) and is generally well described by the Ellingham diagram (Figure 4.1).

Figure 4.1 illustrates how thermodynamically favorable the oxidation of various metals are; the lower the corresponding line, the more stable the metal oxide is and the less energetically favorable its reduction is. In order for a metal oxide to be reduced by hydrogen gas, its free energy for formation must be lower than that of water (indicated by the gray line in Figure 4.1). The free energy difference is the driving force for the reduction reaction, and it becomes clear that a minority of the displayed metal oxides are "reducible". The formation of Ni, Co, and Cu from their oxides are favorable above approximately 800°C. In contrast, the driving force to form Fe from wustite (FeO) is near zero. Many light metals like Al, Mg, and Ti are thus impossible to fabricate using the same hydrogen gas based reductive annealing approach that was used to fabricate Cu_xNi_{1-x} alloys in the previous chapters. The

reduction of more stable oxides requires the use of much stronger reducing agents like calcium vapor or hydrogen plasma.

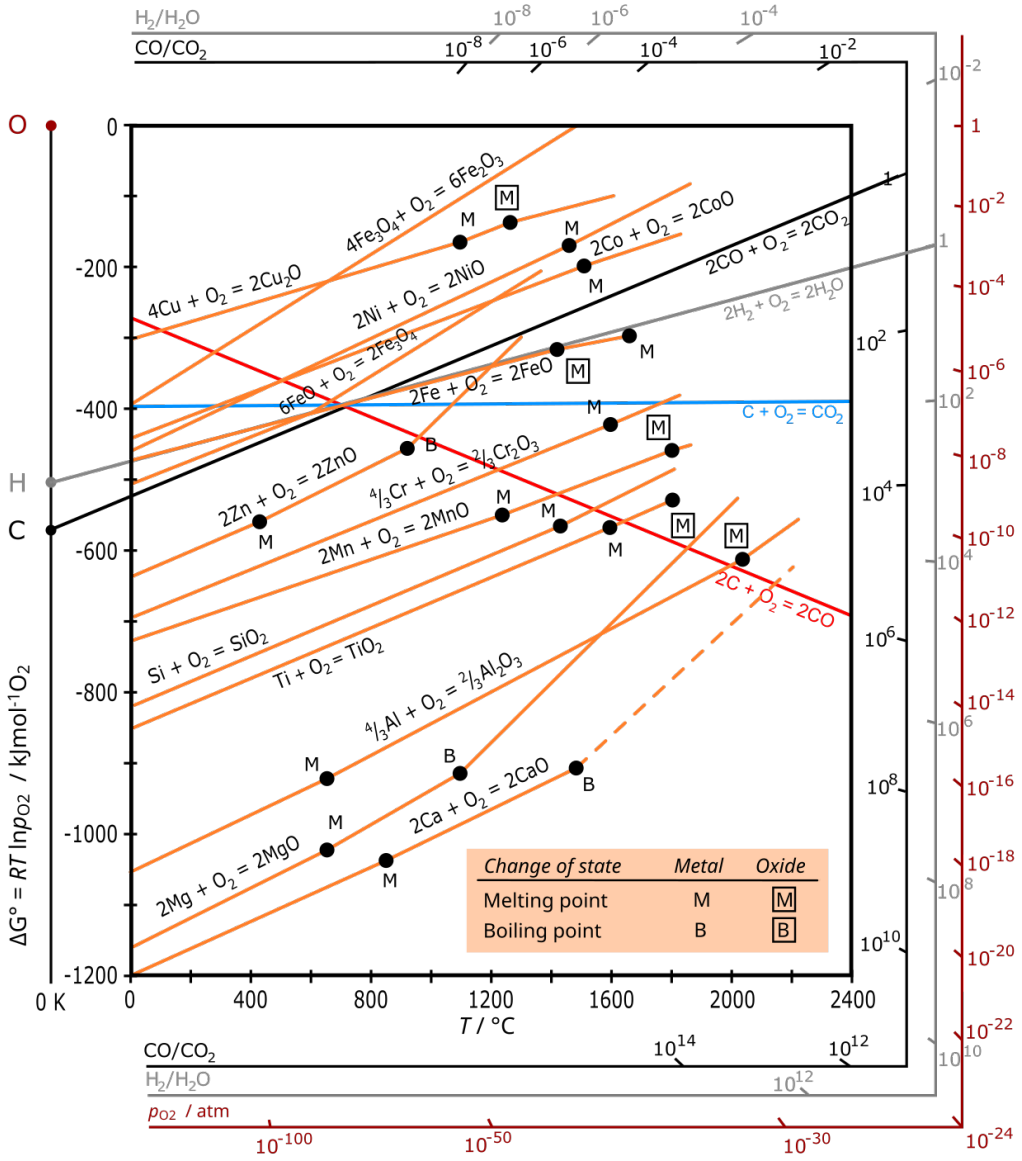

Figure 4.1: The Ellingham diagram gives the Gibbs free energies of the formation of metal oxides relative to the formation of water. The corresponding oxygen partial pressure at equilibrium is also given. Copyright DerSilberspiegel via Wikipedia, licensed under CC BY-SA 4.0.

The Cu_xNi_{1-x} alloy system which has been the focus thus far was fabricated through the reduction of two separate phases, CuO and NiO, which assumed monoclinic and rock salt phases after calcination, respectively. Although separated, both phases were reduced and able to interdiffuse and recombine as the FCC Cu_xNi_{1-x} alloy

through substantial coarsening and densification. Only through kinetic limitations of the reduction reaction are unreduced oxides retained in the printed component. Motivated by the metal matrix composite microstructures demonstrated by Cu_xNi_{1-x}, this chapter seeks to fabricate a two-phase alloy through the selective reduction of only one phase. Instead of fabricating a binary alloy from two reducible oxides that are fully miscible as metals, two alloying materials are selected which are reducible and irreducible as oxides.

4.2 HIAM of oxide dispersion-strengthened Copper

In preliminary attempts to produce ODS alloys by HIAM, Cu_xY_{1-x} is chosen as a prototype system which after calcination contains two oxide components: one reducible by hydrogen gas and another which is not. The reducibility of CuO has been demonstrated by many previous studies on HIAM. Also, the low melting temperature of Cu upon reduction provides an additional benefit as higher homologous temperatures can be achieved with a lab furnace, activating enough solid-state diffusion mechanisms and mobility by which reduced Cu can consolidate into and around irreducible oxide nanoparticles.

For the HIAM of oxide dispersion-strengthened copper, the same PEGda-based honeycomb structures were instead infused with 2 M solutions of copper (II) nitrate hemi(pentahydrate) mixed with minor volumes of 2 M yttrium (III) nitrate hexahydrate to achieve molar ratios of $Cu_{99.5}Y_{0.5}$, $Cu_{99}Y_1$, and $Cu_{95}Y_5$, $Cu_{75}Y_{25}$, $Cu_{50}Y_{50}$, respectively. The structures were subject to the same calcination and reductive annealing thermal treatments as described in Section 2.2. EDS analysis was performed to analyze the average chemical composition after reductive annealing, but the Y content of low-Y specimens below the detection limit of EDS. As a result, the Cu_xY_{1-x} alloys are referred to by their nominal infusion compositions as listed above. For specimens more concentrated in Y, the actual moles of Y was measured to be roughly half of the targeted composition.

4.3 Powder X-Ray Diffraction

Powder specimens for X-ray diffraction are prepared from calcined HIAM specimens by crushing their brittle oxide structures. On the other hand, metallic specimens reduced by the HIAM reductive annealing process are measured as-fabricated. Using Cu Kα radiation generated at 40 kV and 50 mA (λ = 1.54056) Å, $\theta/2\theta$ powder diffraction scans are performed using a 2θ range between 5 and 85°and scan speeds between 4 and 10°/min depending on the signal-to-noise ratio observed for the

sample (SmartLab, Rigaku). Peaks in the diffraction pattern were identified using reference data from the Inorganic Crystal Structure Database (ICSD) [106].

4.4 Phase Diagram and Phase Equilibrium Calculations

Phase diagrams and equilibrium calculations are performed in FactSage 8.3, which considers all the stoichiometric compound and solution phases that may form from a multicomponent system and predicts their phase equilibria by minimizing their Gibbs energy functions. Quasi-binary oxide phase diagrams are calculated at calcination conditions assuming a temperature of 700°C and an ambient pressure of 0.01 bar, using thermodynamic data from FactPS, FTLite, and FTOxide databases [107]. Gas phases are assumed to be ideal. A phase diagram is not calculated for yttria-containing systems since their solutions have not been optimized in the FTOxid database.

4.5 Heterogeneous Grain Morphology

The reductive annealing of Cu_xY_{1-x} oxide honeycombs yielded porous structures which were increasingly dense with for specimens containing greater proportions of Cu. In relatively dense specimens where $x < 0.03$, Cu grains are able to sinter and coarsen, though not in an isotropic manner. Figure 4.2 shows clear bimodal grain morphology on the surface of HIAM $Cu_{97}Y_3$ structures, with segregation between coarse and fine grained regions of Cu. Remarkably, these regions form parallel diagonal lines which appear to be a remanent artifact from the DLP printing of the hydrogel precursor surviving both calcination and reductive annealing thermal treatments. EDS mapping of the coarse and fine grained regions indicate segregation of Y, with increased counts of Y throughout the fine grained region (Figure 4.2e). Although not shown, O map is identical to the Y map, and contrast in the Cu map is caused by the relative tilt of the surface relative to the EDS detector (Figure 4.2c).

Figure 4.3(a) shows the EBSD orientation maps acquired for Cu grains in a reduced HIAM $Cu_{99}Y_1$ honeycomb structure sectioned across its wall thickness. Due to porosity and roughness of the sample even after electropolishing, many unindexed points are depicted as black, including a columnar void present at the core of the wall. Y_2O_3 particles are presumed to be present (Figure 4.4), although too small to be analyzed by EBSD. Larger grains greater than 1 μm in diameter are adjacent to the center void, while smaller submicron grains appeared towards the outer sections of the wall. Inverse pole figures indicate randomly oriented grains without any crystallographic texturing (Figure 4.3b).

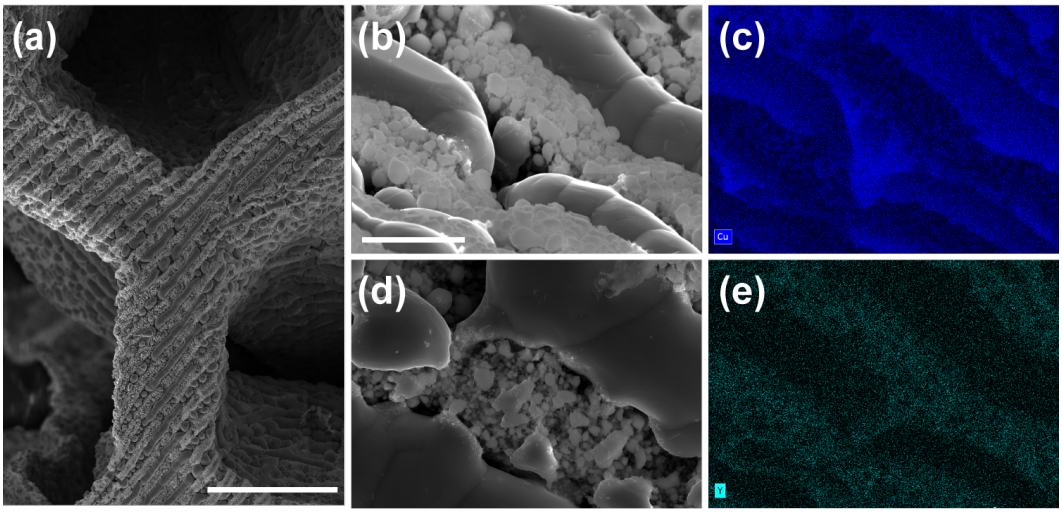

Figure 4.2: Reductively annealed HIAM $Cu_{97}Y_3$. (a, b, d) Surface of honeycomb structure and (c, e) EDS compositional maps showing (c) Cu and (e) Y distribution in (d). Scale bars: (a) 100 μm, (b-e) 5 μm.

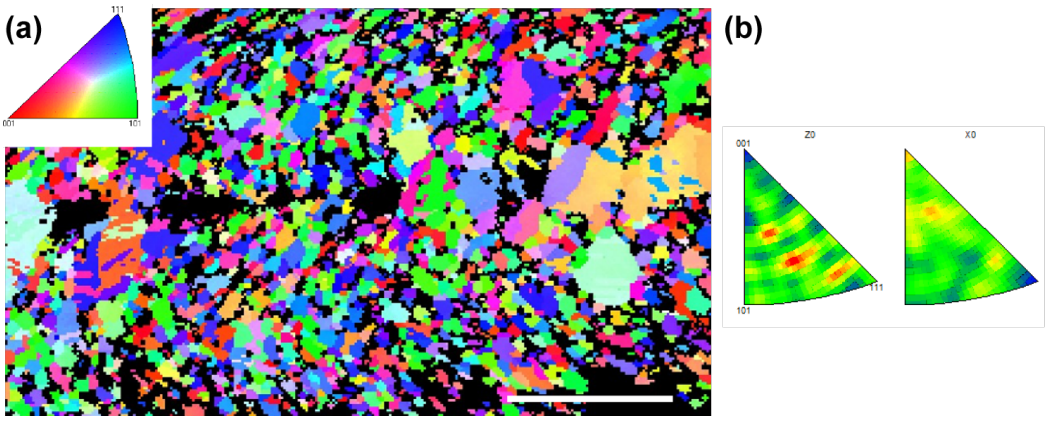

Figure 4.3: EBSD analysis for HIAM $Cu_{99}Y_1$. (a) Crystallographic map for copper grains. Coloring is based on the specimen z-axis inverse pole figure according to the stereographic triangle shown (scale bar 5 μm). (b) Inverse pole figures of the specimen normal (Z) and transverse directions (X).

The initial phases prior to reductive annealing are identified in powder X-ray diffraction patterns for Cu_xY_{1-x} specimens of substantial Y content to ensure adequate signal of Y-containing phases. $Cu_{50}Ni_{50}$ contained two phases after calcination, monoclinic CuO and orthorhombic $Cu_2Y_2O_5$ (Figure 4.4a). This is consistent with phase diagrams predicting stability of the two phases in air below 990°C. (Figure 4.5) [108]. Based on 4.5, we assume CuO and $Cu_2Y_2O_5$ to be the initial starting phases for all Cu_xY_{1-x} compositions fabricated, given that $x < 0.50$ and the maximum calcination temperature was 700°C. The final product of reductive annealing for HIAM $Cu_{75}Y_{25}$ were the FCC Cu and cubic Y_2O_3 (Figure 4.4b). We also predict

that specimens of lesser Y content also form Cu-Y_2O_3 upon reduction.

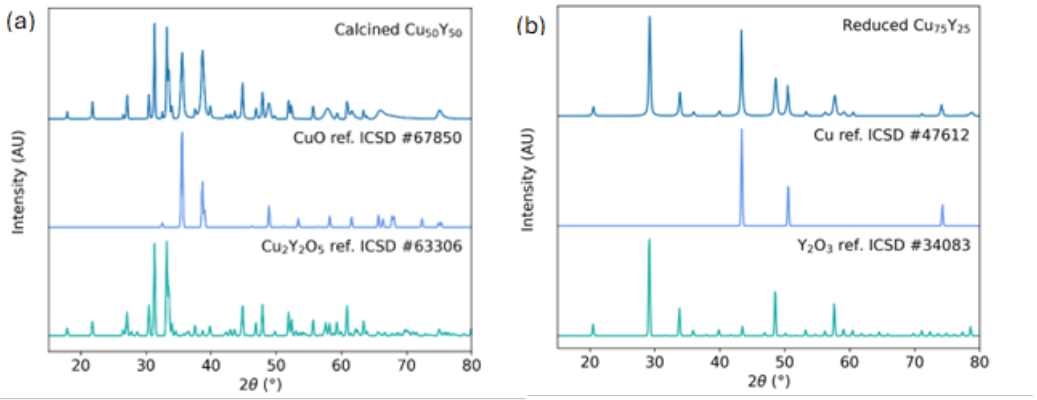

Figure 4.4: Powder X-ray diffraction pattern for HIAM (a) $Cu_{50}Y_{50}$ before reductive annealing and (b) $Cu_{75}Y_{25}$ after reductive annealing, plotted alongside reference patterns for present phases Cu, CuO, $Cu_2Y_2O_5$.

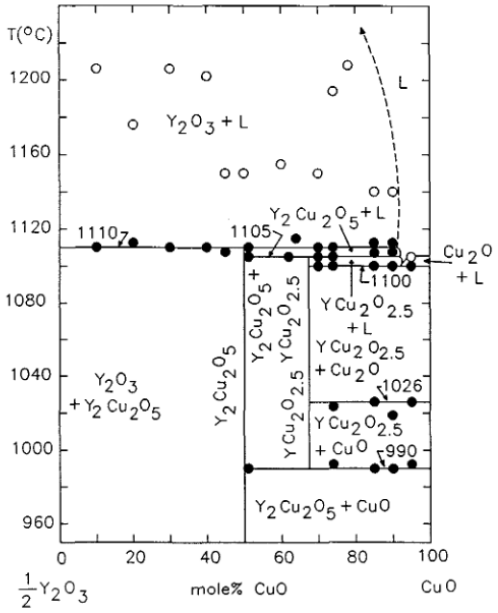

Figure 4.5: Pseudo-binary phase diagram of the Y_2O_3-CuO system in air, indicating the stability of a cupric yttrate $Cu_2Y_2O_5$ phase below 990°C. Reproduced with permission from Springer Nature [108].

4.6 Trimodal Grain Distribution in $Cu_{99.5}Y_{0.5}$

In addition to the bimodal features of the Cu-Y_2O_3 system observed in Figures 4.2 and 4.3, a trimodal grain distribution was also observed in the FIB cross sections of HIAM $Cu_{99.5}Y_{0.5}$. Regions labeled (i) contained the largest Cu grains on the

order of ~10 μm; (ii) contained sub-micron diameter grains; and (iii) could not be measured by SEM or EBSD because of their ultrafine, granular appearance. With ion channeling contrast, small dark spots on the order of 50 nm seem to decorate grain boundaries and triple junctions in region (ii), perhaps indicative of yttria dispersoids. Type-(ii) regions tended to have disperse nanovoids throughout and account for a majority of the FIB cross sections observed. Type-(i) regions often appeared surrounding outer surfaces of the sample (Figure 4.2) and occasionally within large structural voids (Figure 4.6b). The large grains in these regions were also substantially twinned. Type-(iii) regions appeared least frequently but occurred alongside type-(i) regions near large-scale voids.

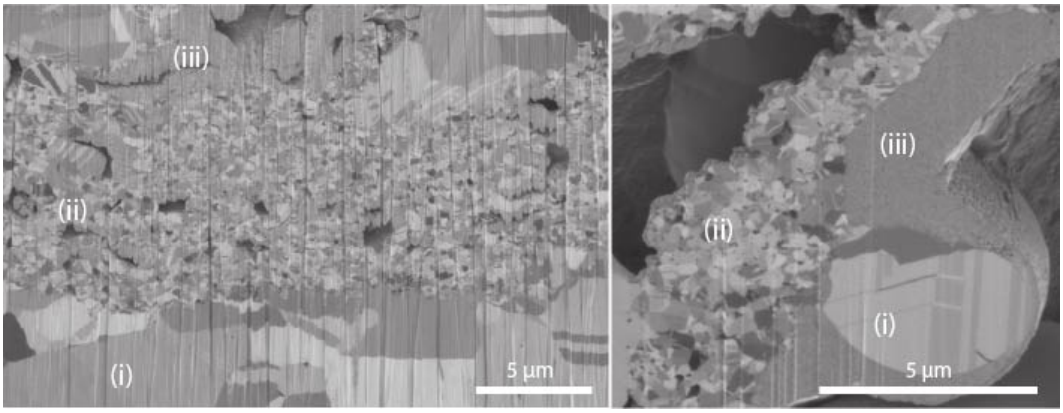

Figure 4.6: Trimodal grain distribution revealed by FIB cross section of reductively annealed HIAM $Cu_{99.5}Y_{0.5}$. Regions (i), (ii), and (iii) contain the largest, intermediate, and smallest grain sizes, respectively.

4.7 Proposed Reduction Pathway for HIAM Cu_xY_{1-x}

While Cu^{2+} and Y^{3+} infused gels were successfully reduced to the target Cu and Y_2O_3 target phases, the pathway by which reduction is achieved introduced extra degrees of heterogeneity into the additively manufactured component. In the most dense alloys, Cu and Y_2O_3 were spatially segregated with clear bi- and trimodal grain size distributions. Assuming Y^{3+} was homogeneized in the infused gels and led to the homogeneous spatial distribution of its oxides after calcination, uniform grain refinement was expected due to the second phase oxides pinning grain boundary motion via Zener pinning [109]. However, in some cases grain refinement surprisingly occurs in varying degrees. Larger grains of type-(i) regions appeared to grow uninhibited given their lack of yttria inclusions while type-(ii) and type-(iii) regions were increasingly refined. It is possible that during hydrogel printing and infusion, nonuniform crosslinking density of the hydrogel from its

photopolymerization (e.g., in DLP printing, directly above a projected pixel versus between two pixels) caused substantial differences in the mass loading of ions during infusion which are exhibited after the thermal treatments as heterogeneous distributions of Y (Figure 4.2a, b, d).

However, a more likely hypothesis is that the difference in reduction kinetics for the two CuO and $Cu_2Y_2O_5$ phases observed in Figure 4.4a gives more time for rapidly reduced Cu to coarsen. In the Cu_xY_{1-x} system, Cu is phase segregated between CuO and $Cu_2Y_2O_5$ which are presumed to reduce at different rates. This may be evidenced by the shells of large Cu grains observed on the outer surface of Cu_xY_{1-x} structures, which would nucleate metallic Cu first due to readily available H_2 during the reductive annealing treatment. In addition to the diffusion limitations discussed throughout Chapter 2, in this system Cu may also be kinetically trapped in the $Cu_2Y_2O_5$ phase since may not directly decompose to Cu and Y_2O_3; in literature it has been demonstrated that the delafossite-type $CuYO_2$ phase could be formed from $Cu_2Y_2O_5$ in a restricted oxygen pressure at 1100°C [110]. This reaction pathway can explain why multiple distributions of grain size occur: the rapidly reducing CuO phase precipitates metallic Cu that is provided more time to sinter and coarsen, as opposed to Cu within $Cu_2Y_2O_5$ which must undergo multiple reduction steps to produce Cu and Y_2O_3 (Figure 4.7). The reaction may be further slowed by diffusion barriers in the late stages of reduction, creating greater differences in reduction times between $Cu_2Y_2O_5$ to $CuYO_2$ and $CuYO_2$ to Y_2O_3. As Cu is gradually reduced, Cu reduced from the Y-containing phases is pinned, leading to spatially heterogeneous grain refinement. Type-(ii) and (iii) regions are also notably located in the cores of the printed structures, while type-(iii) regions are adjacent to structural voids which appear closed off from the outer surface.

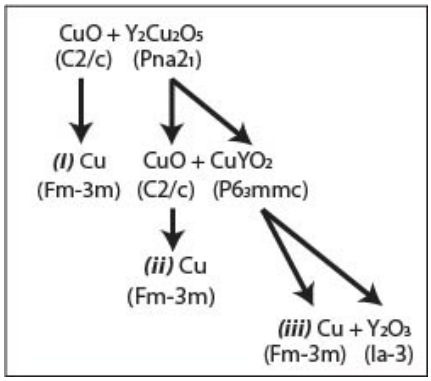

Figure 4.7: Proposed reduction pathway for the HIAM Cu_xY_{1-x} system.

4.8 Perspective on Microstructural Design Using HIAM

The fabrication of HIAM Cu_xY_{1-x} provided new insights into relevant parameters for designing heterogeneous microstructures which may exhibit superior mechanical or functional properties [111]. Key considerations are the reducibilities during material selection and, more specifically, their kinetic pathways to reduction. In addition to thermodynamic considerations like the phase equilibria of the reduced phases (e.g., in Cu_xNi_{1-x} the binary solid solution, or in Cu_xY_{1-x}, Cu + Y_2O_3), the conditions of HIAM have demonstrably led to kinetic limitations that can leave a multitude of stable or metastable oxide phases in the system. Furthermore, the rates at which these reductions occur have a profound effect on the final microstructure. It is possible that even with a different ODS Cu system like Cu_xAl_{1-x} would result in a unimodal microstructure with the same thermal treatment since Cu does not segregate to a mixed oxide phase with Al (Figure 4.8). This highlights the importance of understanding both thermodynamic and kinetic factors in controlling the material's evolution.

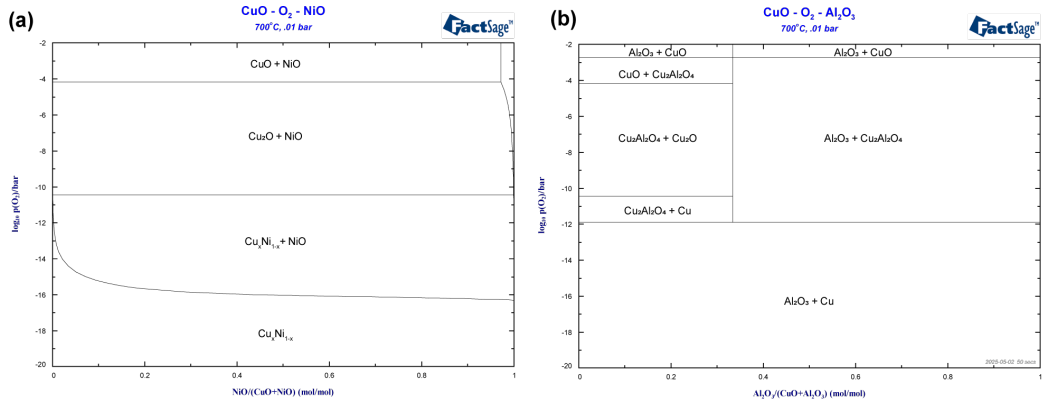

Figure 4.8: Calculated isothermal phase diagram for HIAM (Cu, Ni)O and (Cu,Al)O under calcination conditions used (700°C,~10 bar). Stable phases are shown throughout oxidative (high $p(O_2)$) and reductive environments (low $p(O_2)$).

4.9 Summary

By taking advantage of the nucleation and growth of both oxide and metallic nanoparticles in HIAM, we demonstrate the viability of the approach to produce two-phase metal matrix composites such as ODS alloys. In selecting materials which form oxides that are reducible and irreducible, the composites can be formed and somewhat densified by the coarsening of the metallic matrix surrounding irreducible inclusions which are thermally stable and do not experience significant growth. This serves as a novel approach for manufacturing—and additively manufactur-

ing—engineering alloys, which often rely on microstructural complexity to achieve their desired performance. Furthermore, it circumvents some of the manufacturing limitations associated with processes like ball milling or powder fabrication prior to AM. Nevertheless, densification and kinetic limitations remain as significant challenges for the HIAM process. The rapid growth of Cu was observed to be a double-edged sword that enabled densification and yet competed with the reduction of Y-containing phases. Although not studied in this work, further optimization could be achieved by adapting the reductive annealing thermal treatment to at least two separate temperature regimes, where reduction and coarsening are deconvoluted. The calcination thermal profile can also be controlled to minimize the oxide dispersoid size and distribution prior to reductive annealing.

Chapter 5

NONISOTHERMAL REDUCTION KINETICS OF HIAM OXIDES

This chapter has been directly adapted from:

Tran, T. T. & Greer, J. R. Nonisothermal Kinetics of Reduction in Hydrogel Infusion-Based Additive Manufacturing. *In preparation* (2025)

5.1 Introduction

The complex microstructures revealed in Chapter 2 and 4 exemplified the many mechanisms that are present throughout the microstructural evolution of HIAM. During studies of HIAM Cu_xNi_{1-x} and Cu_xY_{1-x}, calcination was found to produce porous and nanocrystalline metal oxide scaffolds that serve as the precursor for reduction to metal during the reductive annealing step. However, many concurrent processes during reductive annealing led to kinetic limitations affecting the microstructures of the final structures. Trapping of water vapor by shells of reduced metal, for example, diminishes the driving force for reduction and may prevent complete reduction from occurring. By performing a thermochemical study on the reduction reaction forming the metallic phase, this chapter aims to better understand the chemical kinetics of alloy formation in HIAM.

The reduction of metal oxides is frequently studied in literature for its applications in the fields of catalysis, powder metallurgy, and energy. Despite this, reported mechanisms and kinetic parameters for reduction vary greatly due to the reaction's sensitivity to experimental and sample conditions. For example, CuO in H_2 has been observed to both transform directly to Cu and form intermediates like Cu_4O_3 and Cu_2O before Cu [65]. Activation energies for NiO reduction with H_2 varied by orders of magnitude between 10 and 150 kJ/mol [113]. Likewise, numerous kinetic models have been used to describe the reduction reaction in both CuO and NiO, each with different implications about the reaction geometry, mechanism, and rate-limiting steps [54]. To precisely acquire the kinetic parameters for the reduction of HIAM-fabricated oxides and gain insight into the reaction mechanisms occurring during the reductive annealing process, we perform in situ reduction on a thermogravimetric balance on the precursors to binary solid solution Cu_xNi_{1-x} and ODS Cu ($Cu_{99}Y_1$ and $Cu_{99}Al_1$). We derive their reaction models through

combined kinetic analysis and apply a deconvolution approach to decouple multiple independent mechanisms observed.

5.2 Reduction in a Thermogravimetric Analyzer

TGA reduction experiments were performed in ambient pressure conditions at 1 atm under flowing 50 mL/min forming gas (N_2 - 5% H_2) (Discovery TGA 550, TA Instruments). Oxide honeycomb lattices fabricated from the standard HIAM calcination process at 700°C were cut with a razor blade into individual TGA specimens up to 5 mg in mass and placed in an 100 μL alumina pan crucible and subsequently heated to 900°C at 3 different heating rates, β, of 3, 8, and 12°C/min. Between each run, crucibles were cleaned by heating them to 1000°C in air.

5.3 Nonisothermal Kinetic Analysis

The kinetics for an individual solid-state reaction is generally described by two functions: the temperature-dependent rate constant $k(T)$ which follows an Arrhenius form and $f(\alpha)$ which is an algebraic function describing the differential form of the reaction model. A comprehensive list of solid-state kinetic models is presented in the reference [114] and based on their assumptions contain mechanistic insights into the physics and dimensionality of the reaction. Models include those that are nucleation-based, diffusion-based, and shrinking interface-based, which have been used to describe processes like decomposition, crystallization, and phase transformations.

The rate of the reaction $\frac{d\alpha}{dt}$ is

$$\frac{d\alpha}{dt} = k(T)f(\alpha) = Af(\alpha)\exp\left(\frac{-E_a}{RT}\right), \tag{5.1}$$

which is dependent on the absolute temperature T the extent of the reduction reaction α, defined to range between 0 and 1 at the start and end of the reactions, respectively. During the non-isothermal thermogravimetric measurements performed at linear heating rates, the reactions are assumed to begin after the specimen mass stabilizes above 150°C, following the release of any adsorbed moisture. The reactions are assumed to reach completion after the stabilization of the specimen mass. α is thus mass-based and calculated via

$$\alpha = \frac{m_i - m}{m_i - m_f}, \tag{5.2}$$

where m_i and m_f are the initial and final specimen masses after moisture desorption and after the final weight stabilization, and m is the mass measured during the reduction reaction. At constant heating rates $\frac{dT}{dt} = \beta$, the nonisothermal reaction rate as a function of temperature is thus

$$\frac{d\alpha}{dT} = \frac{d\alpha}{dt}\frac{dt}{dT} = \frac{d\alpha}{dt}\frac{1}{\beta}, \tag{5.3}$$

so

$$\frac{d\alpha}{dT} = \frac{A}{\beta}\exp\left(\frac{-E_a}{RT}\right)f(\alpha). \tag{5.4}$$

Isoconversional Friedman Method for Determining Activation Energy

In the Friedman differential isoconversional method for kinetic analysis, the activation energy E_a of a process can be calculated for a given α without any assumption about the form of the kinetic model [115]. Taking the natural logarithm of both sides of Equation 5.4,

$$\log\frac{d\alpha}{dt} = \log\left(\frac{A}{\beta}f(\alpha)\right) - \frac{E_a}{RT}. \tag{5.5}$$

Given data taken at multiple heating rates, for $\frac{d\alpha}{dt}$, α, and T measured at equivalent conversion α, $f(\alpha)$ becomes a constant value and the activation energy E_a can be derived from the slope of the logarithm of the reaction rate vs. the inverse absolute temperature. During the combined kinetic analysis of multi-step reactions described by the subsequent sections, activation energy calculated from the Friedman isoconversional method was used to verify whether multiple reaction steps existed and to provide a starting guess for the activation energy during the combined kinetic analysis.

Combined Kinetic Analysis

The kinetic model $f(\alpha)$ can be expressed in the empirical reduced Sestak-Berggren (SB) form, which is also known as the extended Prout-Tompkins model, i.e.,

$$f(\alpha) = c\alpha^n(1-\alpha)^m \tag{5.6}$$

which is able to describe numerous kinetic models with by fitting parameters c, n, and m [116][117]. Substituting the reduced SB form for the kinetic model function into Equation 5.5 gives

$$\log \frac{d\alpha}{dt} - \log(1-\alpha)^m \alpha^n = \log(cA) - \frac{E_a}{RT}. \tag{5.7}$$

The above equation is the basis for combined kinetic analysis, where simultaneous fitting of various experimental data for the same solid-state reaction should only be described by the identical set of kinetic parameters E_a, $\log(cA)$, and $f(\alpha)$. In other words, data $T - \alpha - \frac{d\alpha}{dt}$ acquired under any experimental condition should fit Equation 5.7 provided the correct kinetic model is chosen [116][117]. For an individual kinetic process, by performing multiple linear heating rate experiments and performing a global optimization for model parameters c, n, and m to yield a linear plot for the left hand side of 5.7 vs. $-\frac{1}{RT}$, we can extract the pre-exponential factor and activation energy for the process. From this approach, the approximate kinetic model can be deduced.

Master Plot Analysis

After successfully extracting the reaction model parameters from combined kinetic analysis, one may plot the profile of the reaction relative to reference curves constructed by theoretical kinetic models, known as a master plot (Figure 5.1). Even if the Sestak-Berggren parameters of the experimentally determined kinetic model does not match those of the ideal models', qualitative agreement may be found graphically from the general behavior given by $f(\alpha)$.

Mathematical Deconvolution for Multi-Step Kinetics

Often, many solid-state processes obey multi-step kinetics, evidenced by features including, but not limited to, changes in activation energy as a reaction progresses as observed in a Friedman plot, the presence of multiple sigmoidal curves in thermogravimetric $\alpha - T$ data, or multiple peaks in derivative thermogravimetric $\frac{d\alpha}{dt} - T$ plots. Mechanistic information for each thermal processes can be extracted by analyzing each kinetic step independently. By performing the analysis described in the above sections by Equations 5.1 - 5.7 for each deconvoluted step in a multi-step process, we can exact the contribution of certain mechanisms to the overall reaction rate as well as their individual kinetic parameters. The overall conversion and reaction rates are

$$\alpha = \sum_i x_i \alpha_i \tag{5.8}$$

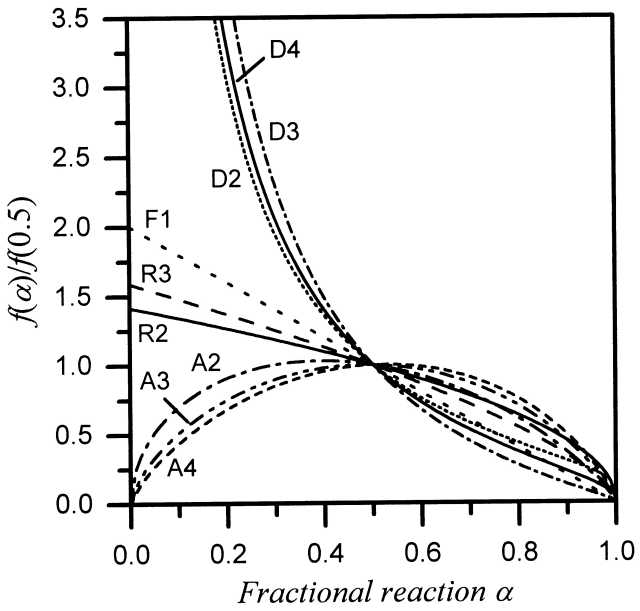

Figure 5.1: Theoretical master curves in differential form representing $f(\alpha)/f(0.5)$ as a function of α for the different kinetic models describing solid-state reactions. Reprinted with permission from [118] Copyright 2000 American Chemical Society.

and

$$\frac{d\alpha}{dt} = \sum_i x_i \left(\frac{d\alpha}{dt}\right)_i = \sum_i x_i k_i(T_i) f_i(\alpha_i), \tag{5.9}$$

where i represents each individual reaction step in the multi-step reaction and x_i are the contribution fractions to the overall reaction.

Following Perejón et al.'s treatment of complex thermal decomposition reactions with multiple overlapping processes, the Fraser-Suzuki function is used to mathematically deconvolute individual kinetic curves and thus reaction steps from overlapped peaks in the thermogravimetric reduction data [117][119][120].

$$y = a_0 \exp\left(-\log(2)\left(\frac{\log\left(1 + 2a_3\frac{x-a_1}{a_2}\right)}{a_3}\right)^2\right), \tag{5.10}$$

where a_0, a_1, a_2, and a_3 are the peak amplitude, position, half-width, and asymmetric skew, respectively. The Fraser-Suzuki function is used in favor of Gaussian and Lorentzian functions due to the asymmetry of kinetic curves which may arise due to non-idealities in experimental data like inhomogeneities in particle size distributions or particle shape. During peak deconvolution, in order to avoid local minima during the nonlinear least squares fitting of up to four FS functions to the experimental derivative peaks, greater weights were assigned to peak shoulders and tails away

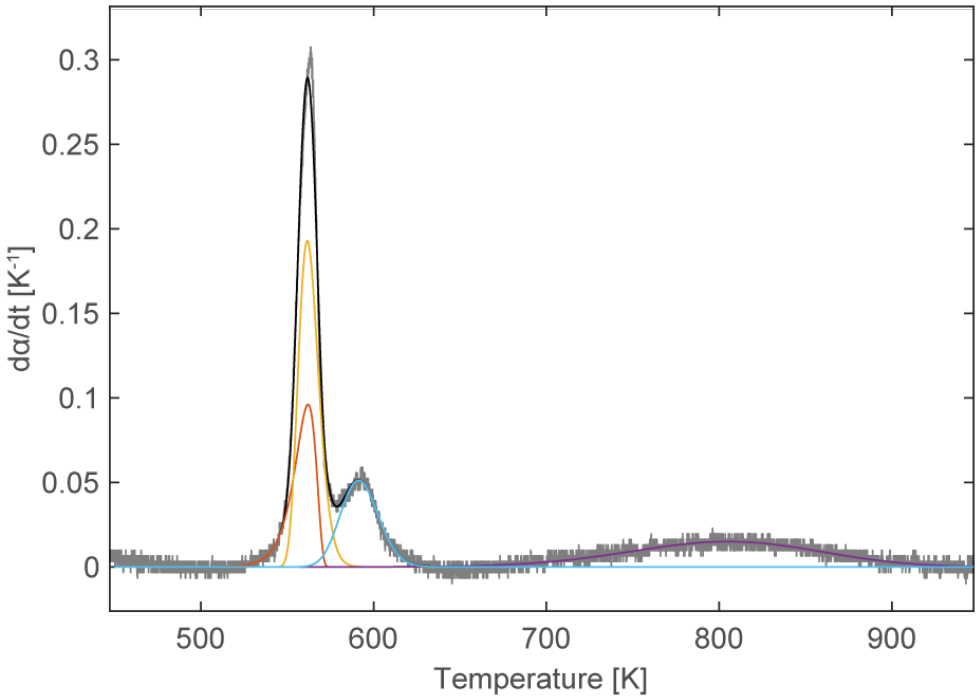

Figure 5.2: Mathematical deconvolution of derivative thermogravimetric signal using four Fraser-Suzuki functions represented by the colored curves, shown for a $Cu_{50}Ni_{50}$ run at 8°C/min. The black curve is their sum and shows a good agreement between the experimental signal and the fitted curve.

from the absolute maxima in order to replicate broad-tailed behavior which was closer in magnitude to the background than the absolute maximum of the derivative thermogravimetric data. This was essential for broad peaks with a higher degree of asymmetry which significantly overlapped with the major peak observed. Following deconvolution, analysis proceeds treating each deconvoluted step as an individual independent step, and the estimated kinetic parameters can be used to reconstruct a model for T-α-$f(\alpha)$.

5.4 Reduction Temperatures and Rates

Multiple mass loss events take place during the reduction of HIAM-ed metal oxides, evidenced by some $\alpha - T$ curves' multiple sigmoidal regions and their derivative curves multiple peaks $\frac{d\alpha}{dT}$ (Figures 5.3 and 5.4). In all compositions reduced, the reaction starts above 200°C and typically nears completion before 400°C. Between pure HIAM CuO and NiO, CuO is the faster reducing component. For the 3°C/min specimens, despite beginning reduction at similar temperatures around 250°C, the range of temperatures through which the reaction takes place is narrower for CuO. The mass of CuO stabilizes after 300°C, but the NiO mass does not fully stabilize

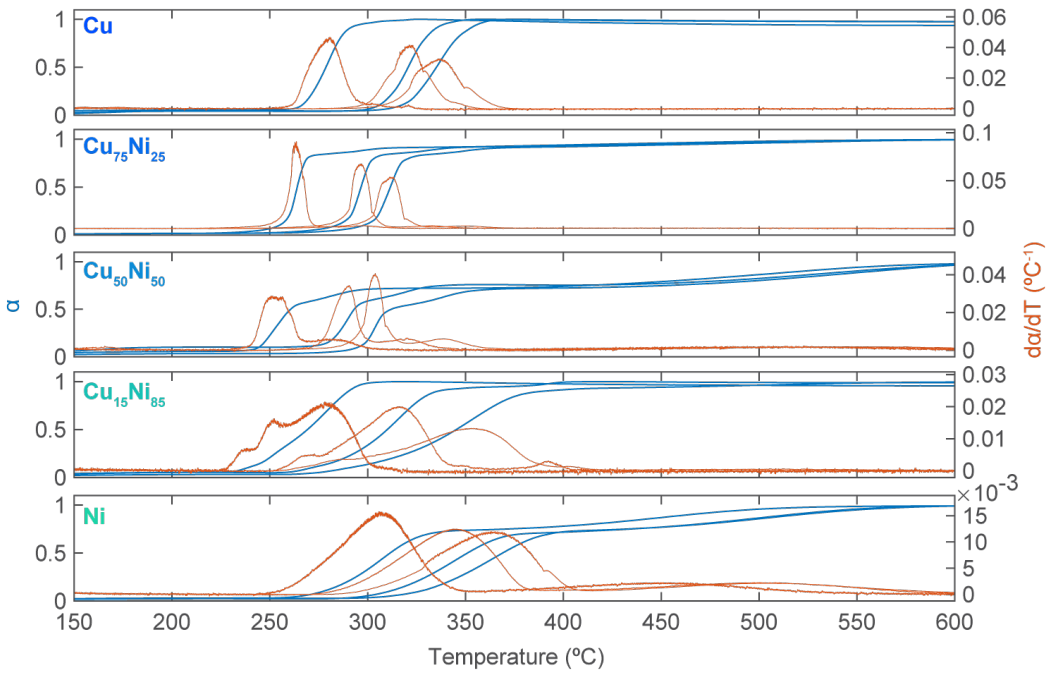

Figure 5.3: Thermogravimetric curves for the H_2-based reduction of HIAM Cu_xNi_{1-x} mixed oxides under linear rate heating conditions 3, 8, and 12°C/min. Both the extent of the reaction α and its derivative with respect to temperature $\frac{d\alpha}{dT}$ are plotted in blue and orange, respectively. Faster heating rates shift the reaction temperature towards higher temperatures.

until beyond 500°C. The reaction temperature range is wider for Ni-rich oxides but narrower for Cu-rich oxides. The fastest starts to reduction are exhibited by $Cu_{50}Ni_{50}$ for the Cu_xNi_{1-x} alloys at 251°C and 206°C for ODS Cu (at a heating rate of 3°C/min). Between the $Cu_{99}Y_1$ and $Cu_{99}Al_1$, the reduction initiates faster in the Y-containing specimen but exhibits wider peaks. The derivative peaks generally maintain their shape throughout the increasing heating rates, indicating the same mechanisms are present throughout specimens of the same composition. Temperatures at the peak mass loss events are are summarized in Table 5.1.

Instances of Mass Gain Following Reaction Completion

In some reductions, such as that of CuO at 3°C/min (Figure 5.5a), the remaining mass of the specimen after the reduction reaction appears to increase, which after data processing, falsely manifests itself as decreasing conversion α after the largest mass loss event and stabilizing around $\alpha \approx 0.9$. Considering that it is not uncommon to observe deposition of a carbon coating in cooler regions of the furnace following the reduction reaction, it is presumed that this increase in sample mass at higher

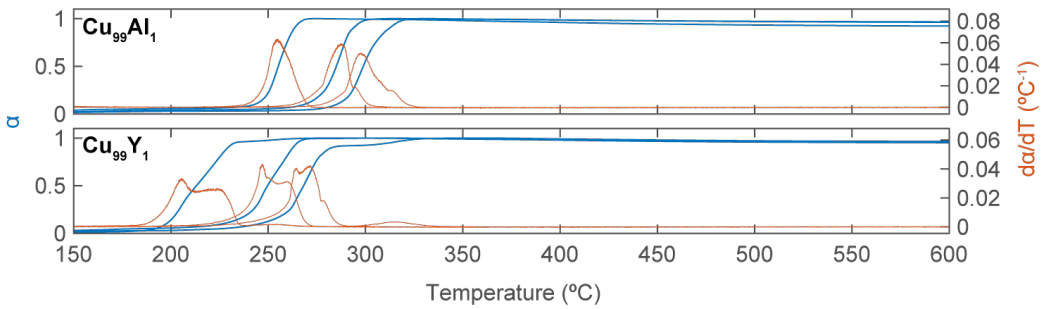

Figure 5.4: Thermogravimetric curves for the H_2-based reduction of HIAM $Cu_{99}Al_1$ and Cu_xY_{1-x} mixed oxides under linear rate heating conditions 3, 8, and 12°C/min. Both the extent of the reaction α and its derivative with respect to temperature $\frac{d\alpha}{dT}$ are plotted in blue and orange, respectively. Faster heating rates shift the reaction temperature towards higher temperatures.

temperatures is also a result of carbon deposition. Reaction with trace hydrocarbon contaminants from gas lines as an example could deposit films of carbon onto the chamber. This artifact is not observed as regularly as a gradual mass losses throughout the entirety of the heating profile, hidden by mass fluctuations at the limits of the balance's precision.

5.5 Incomplete Reduction

Theoretical mass losses are calculated based on the mass fraction of oxygen removed from the specimens assuming that Cu_xNi_{1-x} formed (Cu, Ni)O; $Cu_{99}Y_1$ formed $Cu_2Y_2O_5$ and CuO, and $Cu_{99}Al_1$ formed Al_2O_3 + CuO upon calcination. It is also assumed only oxygen is reduced from CuO and (Cu, Ni)O (Table 5.1). The nominal oxide compositions reported are those of the infusion solution expressed as the molar ratio of Cu to the secondary component, which is not typically maintained after calcination; Cu is typically found to be equilibrated at greater concentrations, presumably due to the stronger affinity of its metal ion to the PEGda hydrogel network during infusion. For the mixed oxides, the theoretical mass fraction of oxygen lost serves as a reference value. Cu_xNi_{1-x} oxides with more Cu would have lower theoretical mass losses, while those of $Cu_{99}Y_1$ and $Cu_{99}Al_1$ would be greater. Nevertheless, during the emulation of the reductive annealing process using a thermogravimetric analyzer, varying degrees of reduction are observed in the HIAM oxides. In the 8°C/min reductions of $Cu_{50}Ni_{50}$ and $Cu_{15}Ni_{85}$, the reaction stagnates with as much as 9.4% of the original oxygen content remaining in the "reduced" sample, compared to the reduction of unalloyed HIAM Cu and Ni oxides which are eventually the most reduced specimens, both leaving an average of 1.4% of

the oxygen content remaining (Table 5.1). In most specimens the reduction reaction concludes and the measured specimen mass stabilizes after 400°C, except for the $Cu_{50}Ni_{50}$ and Ni oxides (Figures 5.3 and 5.4).

Table 5.1: **Percentage Weight Losses and Reaction Temperatures During Reduction of HIAM-ed Cu_xNi_{1-x} and ODS Systems**

Nominal Oxide Composition	Heating Rate (°C/min)	Measured Mass Loss (%)	Theoretical Mass Loss (%)	T_{max} (°C)
Cu	3	19.63	20.11	280
	8	20.02		322
	12	19.84		336
$Cu_{75}Ni_{25}$	3	19.71	20.42	264
	8	19.36		297
	12	19.39		313
$Cu_{50}Ni_{50}$	3	19.60	20.75	251
	8	18.80		290
	12	19.71		304
$Cu_{15}Ni_{85}$	3	20.72	21.21	278
	8	19.22		316
	12	19.71		353
Ni	3	21.18	21.42	306
	8	20.87		343
	12	21.32		365
$Cu_{99}Al_1$	3	20.15	19.98	255
	8	19.97		287
	12	19.72		297
$Cu_{99}Y_1$	3	19.57	19.83	206
	8	19.86		247
	12	19.43		272

5.6 Kinetic Analysis

Deconvoluting Reaction Mechanisms of Reductive Annealing

During the deconvolution of derivative signals, major peak shapes generally remained the same across heating rates indicating the activation of similar mechanisms across the tested heating rates for a given composition. However, curve fitting presented challenges if there existed certain minor features, especially those that could only be observed within one or two datasets but not all three. This is in addition to inaccuracies for Fraser-Suzuki function fitting reported by Resentera and Rodriguez who noted poor fitting of the Fraser-Suzuki function to functions featuring sharp peaks and sudden decays [121]. These minor features included small kinks and

Table 5.2: **Kinetic Parameters Derived from Combined Kinetic Analysis for Reduction of HIAM Cu_xNi_{1-x}, $Cu_{99}Y_1$, and $Cu_{99}Al_1$**

Nominal Oxide Composition	$\overline{x}_i$	E_a (kJ/mol)	ln(cA)	n	m	$f(\alpha)$
Cu	0.97	48.4	9.74	0.93	0.68	A2
$Cu_{75}Ni_{25}$	0.20	75.3	13.97	0.83	0.58	A2
	0.64	51.1	11.18	0.86	0.75	A3
	0.07	73.9	11.90	0.97	0.62	A2
$Cu_{50}Ni_{50}$	0.11	101.4	19.79	0.70	0.69	A3
	0.43	68.7	14.43	1.01	0.63	A2
	0.17	74.9	13.29	0.99	0.60	A2
	0.28	141.4	17.40	1.18	-0.72	D3
Ni	0.71	63.4	11.34	0.88	0.54	A2
	0.29	101.9	12.69	1.08	-0.16	D2
$Cu_{99}Al_1$	0.10	76.9	14.42	0.63	0.73	A3
	0.71	62.4	13.60	0.76	0.81	A3
	0.20	80.8	16.24	0.91	0.71	A3/A2

inflection points occasionally appearing near the higher-temperature shoulders or tails of the major mass loss events; broad weak peaks which ranged from widths of 10 to 100s of degrees; and broad plateauing near the maximum peak heights (Figures 5.3 and 5.4). These features led to less accurate fits that sometimes prevented the analysis of one or more mechanisms such as in $Cu_{75}Ni_{25}$, where $\sum_i \overline{x_i} \neq 1$ (Table 5.2). Numerous overlapped peaks resulted in poor linear fits for $Cu_{15}Ni_{85}$ and $Cu_{99}Y_1$, preventing their kinetic analysis using the datasets acquired. Kinetic analysis results for the remaining compositions are provided in Table 5.2.

The derivative TGA data for Cu, $Cu_{75}Ni_{25}$, $Cu_{50}Ni_{50}$, and Ni were best fit by one, three, four, and two Fraser-Suzuki functions, respectively (Figures 5.5, 5.6, and 5.7). As mentioned, in $Cu_{75}Ni_{25}$, a gradual high temperature transition with a near-zero derivative signal could not be fit and evidences a fourth present mechanism that was not analyzed. For the ODS Cu system, only $Cu_{99}Al_1$ could be analyzed by fitting with three Fraser-Suzuki functions (Figure 5.8). Based on the kinetic master plots, all individual reduction mechanisms are indicated to elicit behaviors indicative of the Avrami nucleation and growth models as well as diffusion-based models (Figures 5.5, 5.6, 5.7, 5.8 and summarized in Table 5.2). In the Avrami nucleation models, reactions' rates are restricted based on the random nucleation and growth of domains that consume potential nucleation sites as they grow and

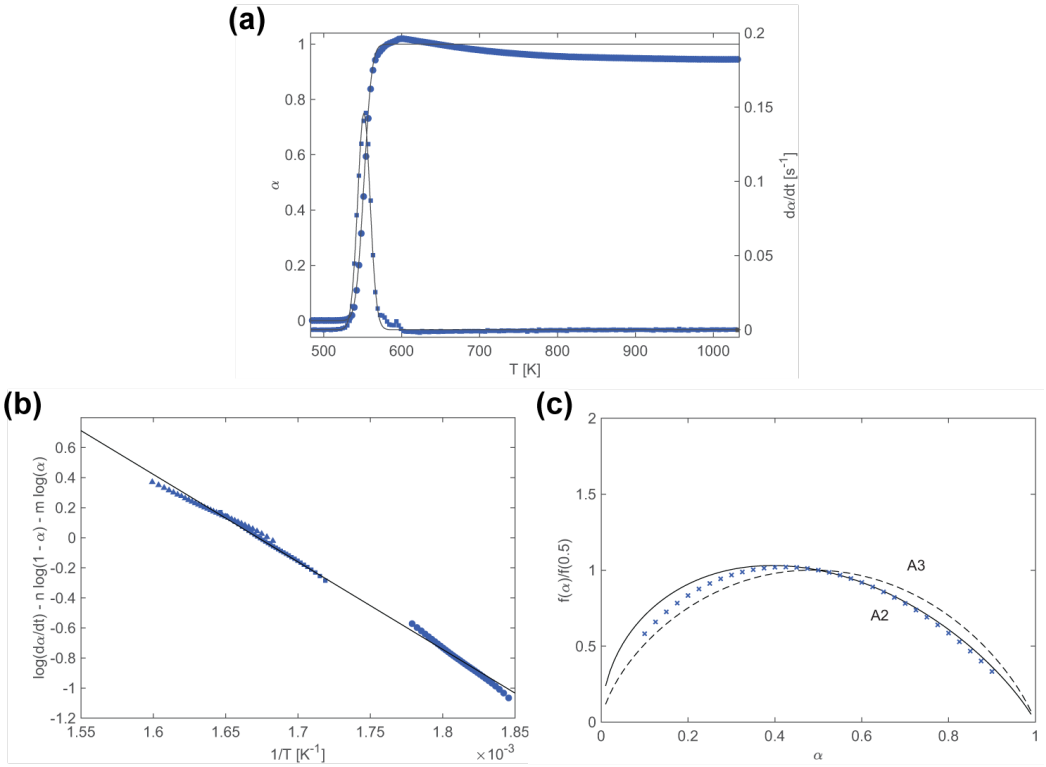

Figure 5.5: Combined kinetic analysis for HIAM Cu oxide reduction after fitting one Fraser-Suzuki function to the derivative signal. (a) Nonisothermal thermogravimetric data recorded at 3°C/min plotted alongside the constructed model (Eqs. 5.8, 5.9). (b) Combined kinetic analysis of the fit function and its (c) corresponding master plot indicating its reaction mechanism.

coalesce, removing interfaces between the reactant and product [114]. It follows that the change in reaction rate due to growth depends on the dimensionality of the growing nuclei. Two-dimensional nuclei limited to formation and growth on surfaces and interfaces are described by the 2D Avrami model (A2), and three-dimensional nuclei forming throughout bulk volumes are described by the 3D Avrami model (A3). Likewise, the difference between 2D and 3D diffusional models is based on limited mass transport of reactants or products on surfaces or in bulk volumes, respectively. The majority of fit reaction models are well described by 2D and 3D dimensionalities or a combination of them.

The reduction of CuO alone was dominated by one reduction event with an activation energy of 48.4 kJ/mol, while the reduction of NiO, barring the effects of diffusion, had a higher activation energy of 63.4 kJ/mol. Although Figure 5.6d is well-fit, the average activation energy of the higher-temperature, diffusion-based reduction of NiO did not fully match that of the energy calculated through the Friedman

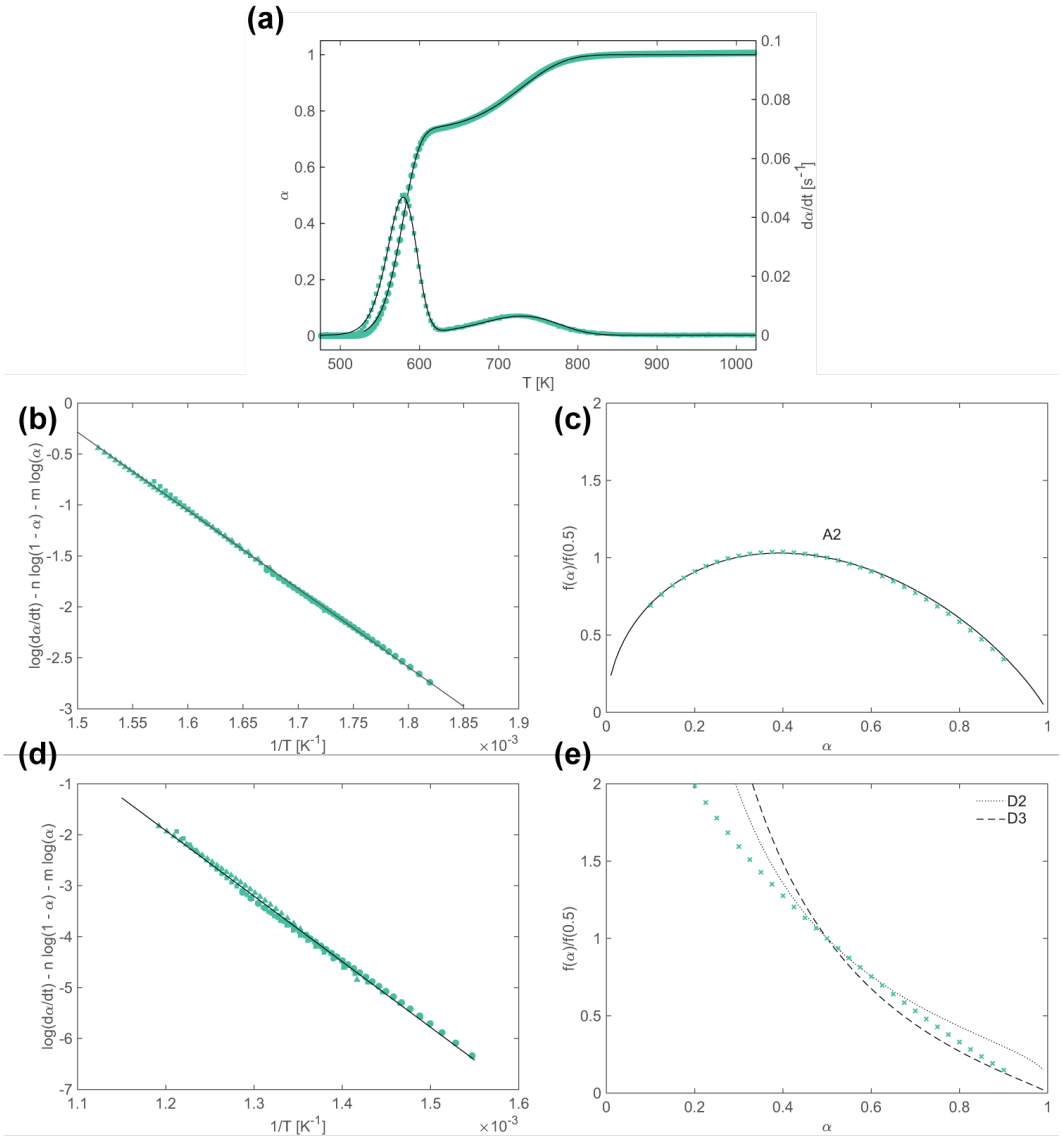

Figure 5.6: Combined kinetic analysis for HIAM Ni oxide reduction after fitting two Fraser-Suzuki functions to the derivative signal. (a) Nonisothermal thermogravimetric data recorded at 3°C/min plotted alongside the constructed model (Eqs. 5.8, 5.9). (b, d) Combined kinetic analysis of each fit function and their (c, e) corresponding master plots indicating their reaction mechanisms.

method, which was found to be increasing with the reaction extent. The reduction of mixed CuO-NiO compositions indicated higher average activation energies of their nucleation mechanisms than those of the individual CuO and NiO components, ranging between 51 to 101 kJ/mol, and the highest activation energies belonged to that of the D3 mechanism in $Cu_{50}Ni_{50}$ at 141.4 kJ/mol. Only specimen compositions containing Ni exhibit diffusion-limited behavior, presumably including the fourth

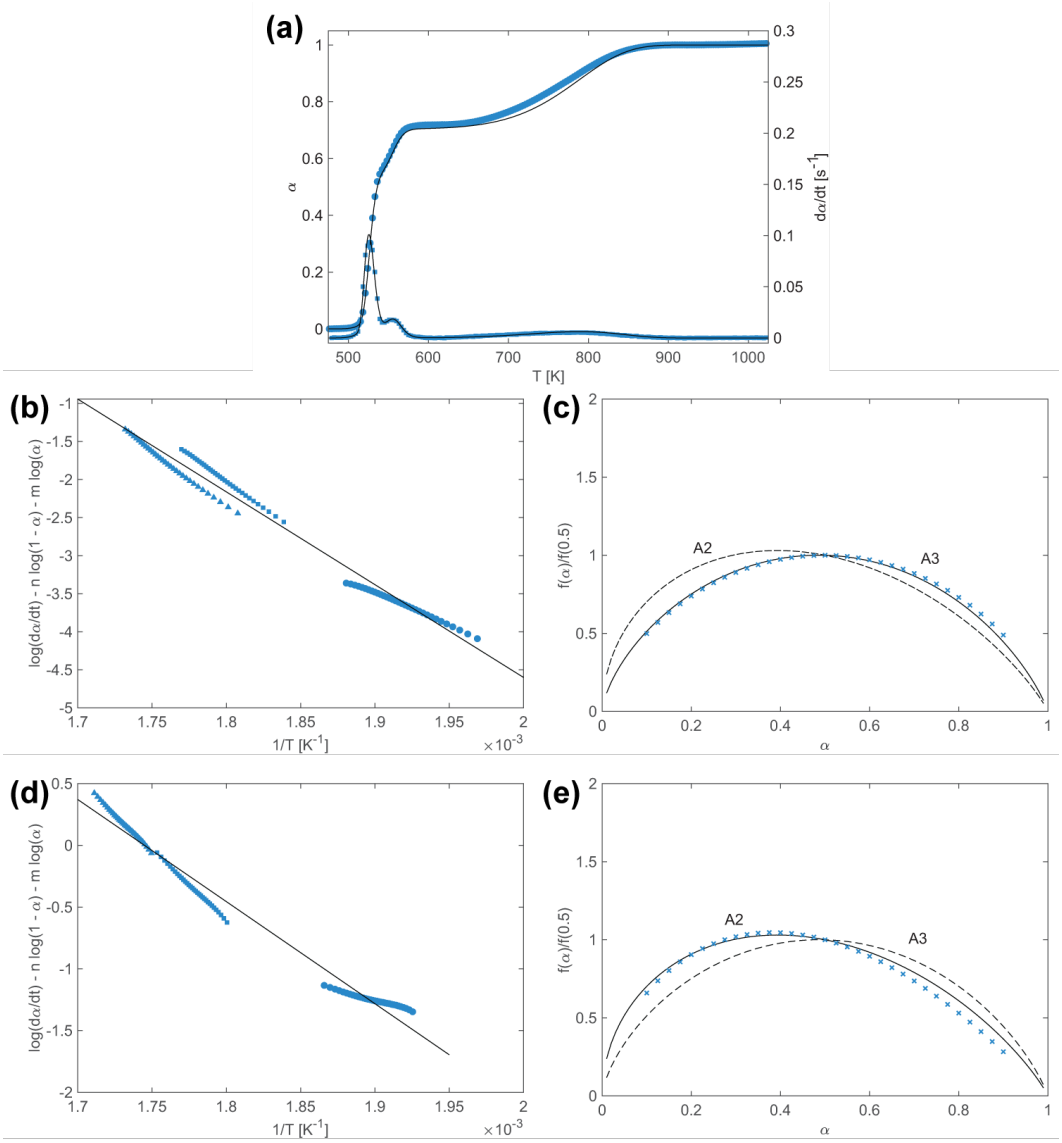

Figure 5.7: Combined kinetic analysis for HIAM $Cu_{50}Ni_{50}$ oxide reduction after fitting four Fraser-Suzuki functions to the derivative signal. (a) Nonisothermal thermogravimetric data recorded at 3°C/min plotted alongside the constructed model (Eqs. 5.8, 5.9). (b, d, f, h) Combined kinetic analysis of each fit function and their (c, e, g, i) corresponding master plots indicating their reaction mechanisms.

un-analyzed mechanism of $Cu_{75}Ni_{25}$ which makes up the remaining fraction of its reaction extent. The ODS alloy $Cu_{99}Al_1$ also exhibited increases in activation energy when compared to that of pure Cu. its reaction was best fit as three separate nucleation events (Figure 5.4).

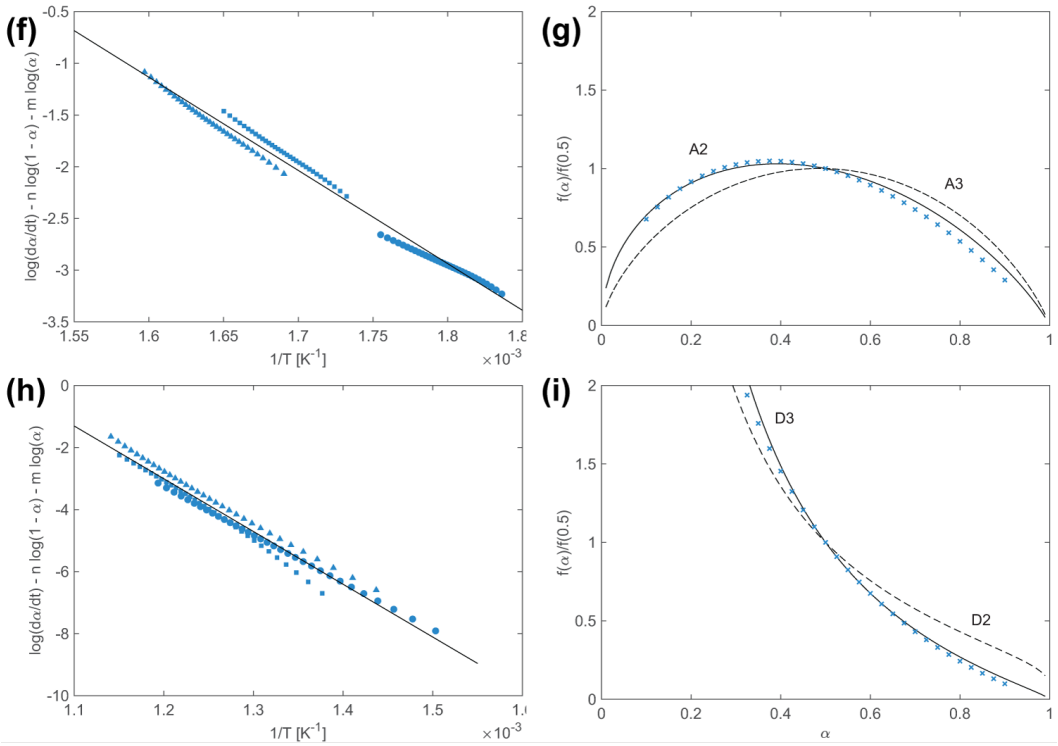

Figure 5.7: (continued).

5.7 Nucleation and Diffusion Limitations in Reductive Annealing

In the kinetic analysis of the reduction of HIAM-produced CuO-NiO system, by tracking the oxygen mass lost by the system, up to four solid-state reaction mechanisms are identified, commensurate with one recent analysis of hydrogen temperature-programmed reduction (TPR-H_2) of CuO-NiO which fitted four peaks to its hydrogen uptake during reduction [122]. Based on master plot analysis, deconvoluted mass loss events are ascribed to reaction mechanisms by which oxygen is extracted from the oxides. In CuO-NiO, the mechanisms which are initially activated are those of the Avrami-type nucleation. The largest mass loss events are comprised of simultaneous nucleation of 2D and 3D nuclei, followed by secondary minor events represented by 2D Avrami nucleation, and concludes through a long-lasting mass loss occurring through by diffusion.

Despite increases in activation energy that occur as a result of alloying in the mixed oxide system, faster rates of reduction are achieved in the Cu_xNi_{1-x} system through the significant rise in the pre-exponential factors. This implies that although the same mechanisms take place, the addition of CuO to NiO and vice versa tends to increase the number of possible nucleation sites at which reduction can occur. This is possible

through smaller crystallite sizes that are observed in more Ni-rich specimens as well as through chemical doping in each oxide's respective lattices, lending increased surface area and sites for hydrogen to adsorb [123][122]. In addition, multiple reduction events arise from the sequential reduction of monoclinic CuO and rock salt NiO where the reduction of CuO occurs first. While Federov et al. claimed that several reduction events resulted from the reduction of distinct NiO phases with increasing amounts of Cu in solid solution, this is not observed here. Rather, the nucleation during HIAM-fabricated CuO-NiO is described by two events—one where 2D and 3D nuclei were formed simultaneously, and another which only 2D nuclei formed—each corresponding to the independent reduction of CuO and NiO (Figure 5.2).

5.8 Dimensionality of the Reduction Reaction

The geometry of the HIAM reduction is complex since the initial state prior to reduction is one which is porous and nanocrystalline. In a local sense, 2D nucleation corroborates the idea that reduction starts at the outer surface of the particles at the gas-solid interface. However, the nucleation can develop additional dimensionality in the beginning stages of reduction due to the size of the oxide nanocrystals relative to the bulk scale structure, resulting in kinetics which appear three dimensional on average. For the diffusion-based reaction mechanisms, three-dimensionality implies the bulk diffusion of hydrogen or oxygen towards or away the reaction interfaces, resulting in slow reaction rates. For Ni, the agreement to the diffusion mechanisms was poorer (Figure 5.6e), which could also be due to complexities in microstructure changing the prevalence of diffusion routes as a function of the reaction extent (e.g., along grain boundaries, dislocations).

In contrast, the ODS $Cu_{99}Al_1$ reaction did not produce diffusion limitations during its reduction, possibly due to the pinning of grain boundaries by Al-based oxides similar to those observed in Cu_xY_{1-x} in Chapter 4. Limited grain growth could cause the apparent three-dimensionality in the three nucleation models fitted. Although there appears to be one major peak, three deconvoluted mechanisms the data may suggest the formation of intermediates during the pathway to reduction, possibly represented by the stable phases in Figure 4.8b.

5.9 A Summary of the Reduction Mechanism in HIAM

Synthesizing the findings of this chapter, reduction studies in literature, and the observations of microstructural features characterized in Chapter 2, a complete

picture of the reduction mechanism in HIAM binary alloys is presented.

In previous experimental findings it has been proposed that the reduction of copper and nickel oxides each obey a nucleation and growth model, in which small metallic nuclei nucleate throughout the parent oxide and grow until they meet and coalesce [62][63][54][64][65]. In this model, the formation of active sites associated with the diffusion of lattice O toward O-depleted reaction interfaces limits the rate of metallic nuclei growth [124]. However, significant deviations from model predictions occur in later stages of reduction [54]. In later stages, deficiencies of hydrogen adsorption sites along the metal-oxide interface slows the reaction [54][65][64][63]. When H_2O vapor formed during the process fails to desorb, it competes with H_2 for adsorption sites [51][52][54]. This is what presumably occurs in the late stages of reduction, when reduced areas grow large enough to impinge each other, encapsulating oxide grains and preventing H_2O from escaping [53]. There is direct evidence for this in the unreduced HIAM Cu_xNi_{1-x} microstructures, which contained dispersed metallic nuclei within grains of unreduced NiO. Despite the higher temperature and duration of the HIAM reduction treatment relative to the previous reduction studies, oxides remain and form a metal-oxide composite microstructure in HIAM Cu_xNi_{1-x}.

The identified NiO phases spanned across various sizes and orientation relationships indicative of various stages of the reduction reaction: (i) larger NiO grains were a matrix for semicoherent metallic nuclei (Figures 2.8 and 2.5); (ii) adjacent Cu_xNi_{1-x} alloy grains featured small semicoherent NiO nuclei (Figure 2.9b, d); and (iii) other alloy grains contained incoherent, randomly oriented NiO (Figure 2.9c, d). Reduction is halted throughout various stages of the reaction due to the concurrent coarsening and growth of metallic nuclei surrounding oxide crystallites. As observed by [61], coherent metal-oxide phase boundaries present during the early stages of reduction (i) can lose their coherency to the collapsing of O vacancy clusters at the metal-oxide interface, resulting in pore formation or grain rotation (iii) [54][63]. Loss of easy diffusion pathways for the ingress and egress of H_2 and H_2O, respectively, greatly inhibit reduction rates. It is possible that sluggish late-stage reduction reorients remaining trapped oxides such that coherency can be maintained with mostly reduced alloy grains (ii).

Through analysis of the reduction reaction's multi-step kinetics, the transitions between the early-stage and late-stage behaviors of the reaction are demarcated. Specifically, the reaction rates of individual components in mixed oxides are decoupled from diffusion-limited behavior that causes deviations from the Avrami nucleation

and growth models describing them. Models formed from this analysis enable the mapping as a function of temperature when the various steps of microstructural formation following reduction occur. Thus, thermal profiles for reductive annealing can be designed to engineer microstructures in future HIAM alloys by engineering the onset of the diffusion-limited regime, to avoid or introduce the kinetic trapping of oxides into the structure.

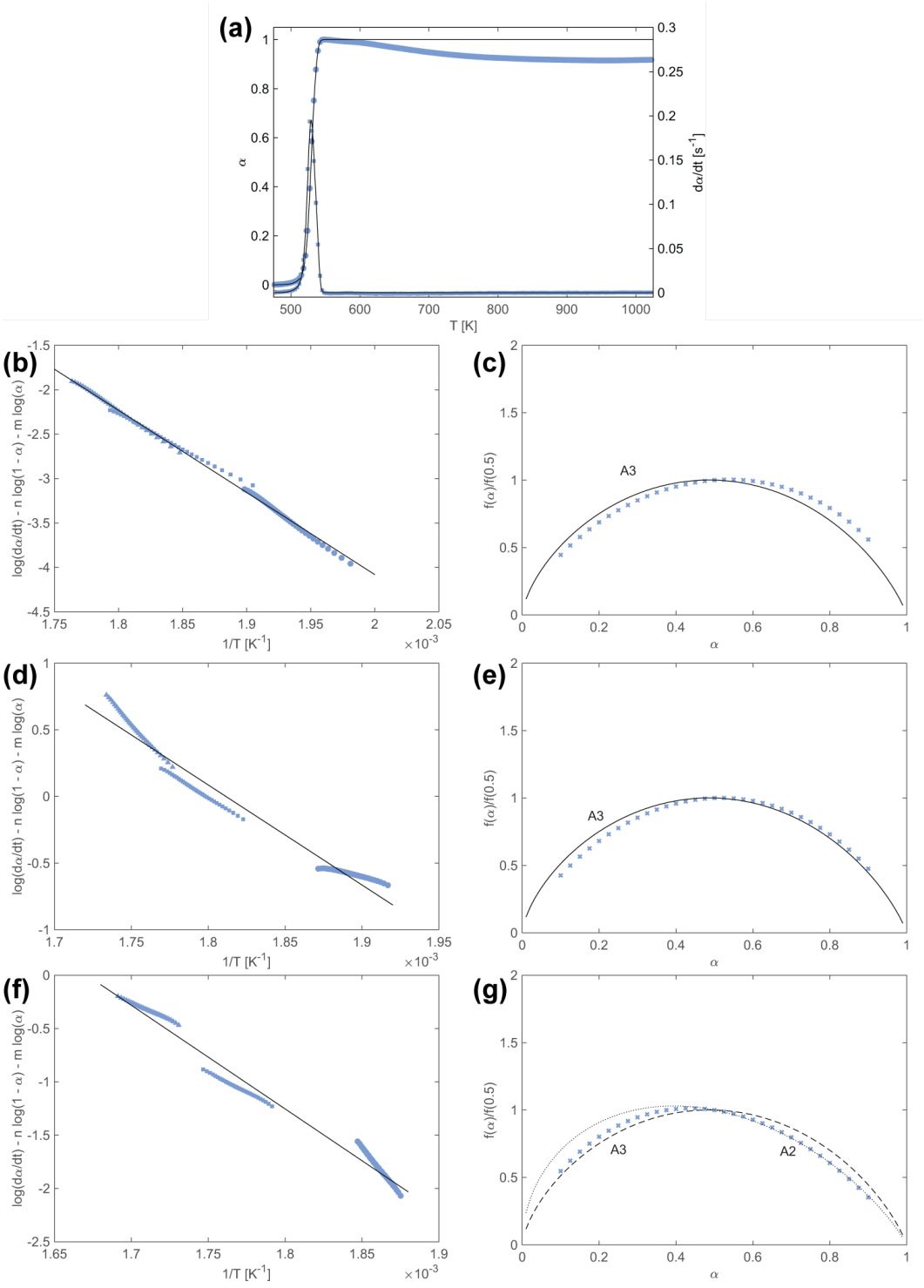

Figure 5.8: Combined kinetic analysis for HIAM $Cu_{99}Al_1$ oxide reduction after fitting three Fraser-Suzuki functions to the derivative signal. (a) Nonisothermal thermogravimetric data recorded at 3°C/min plotted alongside the constructed model (Eqs. 5.8, 5.9). (b, d, f) Combined kinetic analysis of each fit function and their (c, e, g) corresponding master plots indicating their reaction mechanisms.

Chapter 6

SUMMARY AND OUTLOOK

To elucidate the process-structure-properties relationships for HIAM-fabricated alloys, this thesis conducted a systematic characterization of reduced and annealed microstructures down to the atomic scale using a suite of characterization techniques. Using the compositional tunability of HIAM to readily produce microscale structures that sweep the entire compositional space for Cu_xNi_{1-x}, we identify non-equilibrium artifacts from HIAM processing generated in the binary FCC solid solutions. Due to the substantial and uniform grain growth of nucleated metallic clusters into microscale alloyed grains, the resulting polycrystals are chemically homogeneous with fine, equiaxed grains and high densities of annealing twins. Although perhaps limited by their densification after reduction, the use of the reductive annealing process to additively manufacture alloys appears to demonstrate a possible route for in situ grain boundary engineering of as-printed parts. In HIAM Cu_xNi_{1-x}, the fraction and density of coherent twin boundaries, as well as other special boundaries, exceed what has been observed for conventional grain boundary engineered Cu and Ni by strain recrystallization. The growth-based process not only increases the propensity for the formation of lower-energy interfaces, which are favorable for optimizing fatigue or corrosion resistance in manufactured parts, but also increases the manufacturability of grain boundary engineered parts, enabling the design of more complex part geometries for these complex material microstructures.

Furthermore, for the first time, HIAM alloys are discovered with trapped unreduced oxide grains and nano-inclusions which are hierarchical in nature. They assume various orientation relationships, which are indicative of the stages of microstructural evolution throughout the reductive annealing process. As HIAM Cu_xNi_{1-x} alloys nucleate and grow, coherency is maintained between the oxide and reduced metal through a cube-on-cube relationship with a large lattice misfit. During the later stages of reduction, the reaction is effectively halted by the presence of water vapor trapped by the formation of a metallic shell that acts as a diffusion barrier preventing the ingress of H_2 and the egress of H_2O. As metallic grains coarsen, they lose their coherency and can favor void formation. The kinetics of the internal reduction reaction favors the maintenance of the semicoherent orientation relationship, showing that NiO reduction is topotactic in nature—the crystallographic orientation of alloy

which is reduced is dictated by the orientation of its parent oxide. The stages of oxide retention throughout the HIAM alloys therefore present another opportunity for microstructural engineering through HIAM thermal treatments. Incomplete reduction can introduce nanodisperse oxide inclusions resulting in metal matrix composite microstructures, and the local degree of reduction manipulates the coherency between the metal matrix and oxide inclusions. Both inter- and intragranular defects resulting from the process culminate in elevated average nanoindentation hardnesses regardless of composition, up to four times those of bulk Cu_xNi_{1-x}. A composition dependence is only found in the strengths of micropillars and their scaling of the "smaller is stronger" size effect, which is related to changes in the reduction kinetics influencing the density of inclusions and voids incorporated by the HIAM reductive annealing process. The defect densities of the resulting alloys are as a result sensitive to the starting proportions of the oxide phases and may be controlled with further knowledge of their reduction kinetics.

Additional insights into the microstructural evolution of the reductive annealing process are provided by attempts to fabricate multiphase alloys with HIAM. By replacing a reducible oxide with an irreducible oxide, the irreducible oxide can be intentionally left in a matrix of reduced metal to form an oxide dispersion-strengthened alloy. In targeting particular phases after reduction, thermodynamic considerations such as phase stability and equilibria are essential for predicting the phase compositions before and after reduction. However, kinetic pathways to reduction can further induce profound microstructural heterogeneities. In Cu_xY_{1-x}, observed bimodal and trimodal grain distributions are due to the initial segregation of Cu between two phases, where the different reduction rates of the phases led to different rates of grain growth in the reduced Cu. Reduction pathways are therefore chemistry-dependent parameters that determine microstructural heterogeneities based on the speed at which metal is reduced from their parent oxide phases.

Lastly, the chemical kinetics of the reduction reaction are studied via thermogravimetry. Results for the reduction of mixed oxides fabricated by HIAM illustrated the multi-step complexity of their reduction, even for binary metallic solid solutions like Cu_xNi_{1-x}, whose microstructural evolution included concurrent processes via the solid-state reduction reaction, grain growth, and densification, and resulted in the retention of up to 10% of their oxygen content. Convoluted mass loss events in the derivative mass signals necessitated the application of mathematical deconvolution, after which kinetic analysis could be performed to extract the kinetic parameters for

the individual reaction mechanisms active during reductive annealing as a function of temperature. The analysis is able to resolve the Avrami-type nucleation of each metal oxide phase, as well as the instance at which diffusion limitations arise, particularly for the NiO-containing mixed oxides at higher temperatures greater than 400°C. Through the combination of thermodynamic and kinetic considerations for the formation of metal in HIAM-fabricated systems, it becomes possible to adapt the thermal profiles and engineer the microstructures and properties exhibited in this thesis. For example, introducing an initial low temperature hold at the peak reduction temperatures could ensure the complete reduction of the reducible oxides while minimizing premature densification that would lead to diffusion limitations and thus oxide retention. Otherwise, compositions can be specifically selected such that more complex reduction pathways can intentionally incorporate heterogeneous or gradient grain morphologies. The combination of the HIAM approach's thermal and compositional tunability with the introduced kinetic analysis and calculation of phase diagrams (CALPHAD) approach is powerful for the design for future heterogeneously microstructured HIAM alloys.

Outlook

In this work, the application of kinetic analysis, microstructural characterization, and micromechanical testing are used in tandem to further refine our understanding of the process-structure-properties relationships for the metal-forming process in HIAM. In developing this understanding, this research not only continues to expand the microstructural space achievable by HIAM but also offers valuable design considerations for metals and alloys processed by solid-state processes—additively manufactured and otherwise. It informs future work on the in situ microstructure design of additively manufactured materials and yet provides some insight into sustainable metallurgy. Reductive annealing as performed in HIAM is an extension of the hydrogen-based direct reduction, which is a carbon-free alternative to traditional metallurgical processes whose only product is water vapor, provided that the source of hydrogen is also green. While many current studies focus on the reduction of wustite, FeO, for the formation of iron since steel production is one of the greatest industrial contributors to carbon emissions, here it is shown how reduction can also be used to successfully fabricate Cu- and Ni-based binary alloys and oxide dispersion-strengthened alloys with heterogeneous microstructures. In spite of the challenge of pore retention and the inhibition of the reduction reaction by retained water, the use of a nanoporous oxide scaffold for reduction shows

promise as a method to promote the full reduction of the oxide prior to densification and grain growth. Once densified, the process may even be leveraged to enhance properties, either with increased densities of low-energy interfaces or the incorporation of nanoscale intragranular defects. Therefore, HIAM is not just an additive manufacturing approach capitalizing on the low temperature synthesis of metal in the solid state; its processing also offers a unique environment where substantial grain growth of reduced metal is driven by the reduction of grain curvatures and by chemical potential gradients whilst being simultaneously influenced by reduction kinetics. As a result, novel and complex microstructural landscapes can be fabricated which may contribute to the development of new heterogeneously nanostructured alloys with favorable mechanical properties. The introduction of heterogeneities like the bi- and trimodal grain morphologies and the hierarchical unreduced oxides could potentially be tuned, for example, to form heterostructured alloys which take advantage of hetero-deformation induced (HDI) strengthening to enhance strength and HDI strain hardening to retain or increase ductility.

The characterization performed in this study in general presents an experimental framework that showcases microscale metal additive manufacturing as a powerful method for alloy design. The compositional tunability of HIAM combined with microscale testing approaches enabled property mapping of the entire Cu_xNi_{1-x} composition space even with minimal amounts of material used, since the fabrication of many mm-scale specimens with unique alloy compositions could be parallelized and subsequently tested by suites of microscale characterization techniques. With recent technological advancements and efforts towards automated, high-throughput characterization, for example towards rapid nanoindentation mapping, this integrated AM and micro-characterization approach could assist in the development of novel compositionally complex alloys like high entropy alloys (HEAs) where the composition space becomes infinitely larger than those of the binary alloys characterized in this study, and their phase equilibria can be nearly as complicated. The integrated fabrication and characterization approach, especially when combined with kinetic modeling and CALPHAD approaches, could serve as a promising methodology for alloy prototyping, enabling the rapid optimization of process-structure-properties relationships for novel alloys. Ultimately, their characterization lays the groundwork to tailor them and unlock the full potential of these processes, structures, and properties for a wide range of applications.

Although the characterization was *small*, its impacts are **big**.

BIBLIOGRAPHY

1. Gault, B. *et al.* Atom probe tomography. *Nature Reviews Methods Primers* **1.** Publisher: Nature Publishing Group, 1–30. ISSN: 2662-8449. doi:10.1038/s43586-021-00047-w (2021).

2. Raabe, D., Tasan, C. C. & Olivetti, E. A. Strategies for improving the sustainability of structural metals. en. *Nature* **575,** 64–74. ISSN: 1476-4687. doi:10.1038/s41586-019-1702-5 (2019).

3. Sames, W. J., List, F. A., Pannala, S., Dehoff, R. R. & Babu, S. S. The metallurgy and processing science of metal additive manufacturing. en. *International Materials Reviews* **61,** 315–360. ISSN: 0950-6608, 1743-2804. doi:10.1080/09506608.2015.1116649 (2016).

4. Herzog, D., Seyda, V., Wycisk, E. & Emmelmann, C. Additive manufacturing of metals. *Acta Materialia* **117,** 371–392. ISSN: 1359-6454. doi:10.1016/j.actamat.2016.07.019 (2016).

5. Lewandowski, J. J. & Seifi, M. Metal Additive Manufacturing: A Review of Mechanical Properties. *Annual Review of Materials Research* **46,** 151–186. doi:10.1146/annurev-matsci-070115-032024 (2016).

6. Bertsch, K. M., Meric de Bellefon, G., Kuehl, B. & Thoma, D. J. Origin of dislocation structures in an additively manufactured austenitic stainless steel 316L. *Acta Materialia* **199,** 19–33. ISSN: 1359-6454. doi:10.1016/j.actamat.2020.07.063 (2020).

7. Li, Z. *et al.* Enhanced strengthening and hardening via self-stabilized dislocation network in additively manufactured metals. *Materials Today* **50,** 79–88. ISSN: 1369-7021. doi:10.1016/j.mattod.2021.06.002 (2021).

8. Liu, L. *et al.* Dislocation network in additive manufactured steel breaks strength–ductility trade-off. *Materials Today* **21,** 354–361. ISSN: 1369-7021. doi:10.1016/j.mattod.2017.11.004 (2018).

9. Ramirez, D. A. *et al.* Novel precipitate–microstructural architecture developed in the fabrication of solid copper components by additive manufacturing using electron beam melting. *Acta Materialia* **59,** 4088–4099. ISSN: 1359-6454. doi:10.1016/j.actamat.2011.03.033 (2011).

10. Daryadel, S. *et al.* Localized Pulsed Electrodeposition Process for Three-Dimensional Printing of Nanotwinned Metallic Nanostructures. *Nano Lett.* **18,** 208–214. ISSN: 1530-6984. doi:10.1021/acs.nanolett.7b03930 (2018).

11. Gaytan, S. *et al.* Comparison of Microstructures and Mechanical Properties for Solid and Mesh Cobalt-Base Alloy Prototypes Fabricated by Electron Beam Melting. *Metallurgical and Materials Transactions A* **41,** 3216–3227. ISSN: 1543-1940. doi:10.1007/s11661-010-0388-y (2010).

12. Dehoff, R. R. *et al.* Site specific control of crystallographic grain orientation through electron beam additive manufacturing. *Materials Science and Technology* **31,** 931–938. ISSN: 0267-0836. doi:10.1179/1743284714Y.0000000734 (2015).

13. Randle, V. Twinning-related grain boundary engineering. en. *Acta Materialia* **52,** 4067–4081. ISSN: 13596454. doi:10.1016/j.actamat.2004.05.031 (2004).

14. Watanabe, T. Grain boundary engineering: historical perspective and future prospects. en. *J Mater Sci* **46,** 4095–4115. ISSN: 1573-4803. doi:10.1007/s10853-011-5393-z (2011).

15. Sofinowski, K. A., Raman, S., Wang, X., Gaskey, B. & Seita, M. Layerwise engineering of grain orientation (LEGO) in laser powder bed fusion of stainless steel 316L. *Additive Manufacturing* **38,** 101809. ISSN: 2214-8604. doi:10.1016/j.addma.2020.101809 (2021).

16. Seita, M. & Gao, S. Broadening the design space of engineering materials through "additive grain boundary engineering". *Journal of Materials Science* **57,** 9530–9540. ISSN: 1573-4803. doi:10.1007/s10853-022-06886-6 (2022).

17. Nie, Y., Chang, Y. T. & Charpagne, M. A. Origins of twin boundaries in additive manufactured stainless steels. *Acta Materialia* **275,** 120035. ISSN: 1359-6454. doi:10.1016/j.actamat.2024.120035 (2024).

18. Saccone, M. A., Gallivan, R. A., Narita, K., Yee, D. W. & Greer, J. R. Additive manufacturing of micro-architected metals via hydrogel infusion. en. *Nature* **612,** 685–690. ISSN: 1476-4687. doi:10.1038/s41586-022-05433-2 (2022).

19. Zhang, W. *et al.* Suppressed Size Effect in Nanopillars with Hierarchical Microstructures Enabled by Nanoscale Additive Manufacturing. *Nano Lett.* **23,** 8162–8170. ISSN: 1530-6984. doi:10.1021/acs.nanolett.3c02309 (2023).

20. Yee, D. W. *et al.* Hydrogel-Based Additive Manufacturing of Lithium Cobalt Oxide. en. *Advanced Materials Technologies* **6,** 2000791. ISSN: 2365-709X. doi:10.1002/admt.202000791 (2021).

21. Sun, Y. & Greer, J. R. Micro-Architected Lithium Cobalt Oxide Electrodes Via Hydrogel Infusion Additive Manufacturing. *ECS Meeting Abstracts* **MA2023-01.** Publisher: IOP Publishing, 541. ISSN: 2151-2043. doi:10.1149/MA2023-012541mtgabs (2023).

22. Ma, S. *et al.* Additive Manufacturing of Micro-Architected Copper based on an Ion-Exchangeable Hydrogel. *Angewandte Chemie International Edition* **63.** _eprint: https://onlinelibrary.wiley.com/doi/pdf/10.1002/anie.202405135, e202405135. ISSN: 1521-3773. doi:10.1002/anie.202405135 (2024).

23. Yaw, N. S. *et al.* Precursor design for additive manufacturing of ceramics through hydrogel infusion. *Inorganic Chemistry Frontiers* **12.** Publisher: The Royal Society of Chemistry, 3055–3072. ISSN: 2052-1553. doi:10.1039/D5QI00139K (2025).

24. Ji, Y. & Yee, D. *Low Shrinkage Hydrogel Infusion Additive Manufacturing of Ceramics and Metals* 2025. doi:10.26434/chemrxiv-2025-vwjgv.

25. Vogl, V., Åhman, M. & Nilsson, L. J. Assessment of hydrogen direct reduction for fossil-free steelmaking. *Journal of Cleaner Production* **203,** 736–745. ISSN: 0959-6526. doi:10.1016/j.jclepro.2018.08.279 (2018).

26. El-Zoka, A. A., Stephenson, L. T., Kim, S.-H., Gault, B. & Raabe, D. The Fate of Water in Hydrogen-Based Iron Oxide Reduction. en. *Advanced Science* **10,** 2300626. ISSN: 2198-3844. doi:10.1002/advs.202300626 (2023).

27. Kim, S.-H. *et al.* Influence of microstructure and atomic-scale chemistry on the direct reduction of iron ore with hydrogen at 700°C. *Acta Materialia* **212,** 116933. ISSN: 1359-6454. doi:10.1016/j.actamat.2021.116933 (2021).

28. Tran, T. T., Gallivan, R. A. & Greer, J. R. Multiscale Microstructural and Mechanical Characterization of Cu-Ni Binary Alloys Reduced During Hydrogel Infusion Additive Manufacturing (HIAM). *Small, under review* (2025).

29. Billinge, S. J. L. The rise of the X-ray atomic pair distribution function method: a series of fortunate events. *Philosophical Transactions of the Royal Society A.* Publisher: The Royal Society Publishing. doi:10.1098/rsta.2018.0413 (2019).

30. Juhás, P., Davis, T., Farrow, C. L. & Billinge, S. J. L. PDFgetX3: a rapid and highly automatable program for processing powder diffraction data into total scattering pair distribution functions. *Journal of Applied Crystallography* **46.** Publisher: International Union of Crystallography, 560–566. ISSN: 0021-8898. doi:10.1107/S0021889813005190 (2013).

31. Farrow, C. L. *et al.* PDFfit2 and PDFgui: computer programs for studying nanostructure in crystals. *Journal of Physics: Condensed Matter* **19,** 335219. ISSN: 0953-8984. doi:10.1088/0953-8984/19/33/335219 (2007).

32. Egami, T. & Billinge, S. J. L. *Underneath the Bragg peaks: structural analysis of complex materials Pergamon materials series* **v. 7.** ISBN: 978-0-08-042698-3 (Pergamon, Kiddington, Oxford, UK Boston, 2003).

33. Merkle, K. L. & Shao, B. Studies of NiO-Metal Interfaces. *MRS Proceedings* **122,** 69. ISSN: 1946-4274. doi:10.1557/PROC-122-69 (1988).

34. Walls, B. *et al.* Nanodomain structure of single crystalline nickel oxide. en. *Sci Rep* **11,** 3496. ISSN: 2045-2322. doi:10.1038/s41598-021-82070-1 (2021).

35. Owen, E. A. & Pickup, L. Parameter Values of Copper-Nickel Alloys. de. *Zeitschrift für Kristallographie - Crystalline Materials* **88,** 116–121. ISSN: 2196-7105. doi:10.1524/zkri.1934.88.1.116 (1934).

36. Zhang, W. *et al.* Suppressed Size Effect in Nanopillars with Hierarchical Microstructures Enabled by Nanoscale Additive Manufacturing. *Nano Letters* **23,** 8162–8170. ISSN: 1530-6984. doi:10.1021/acs.nanolett.3c02309 (2023).

37. Maity, P. C., Lahiri, I. & Suresh, K. S. Role of twin boundaries and copper content on the mechanism of recrystallization in Ni-Cu alloys. *Materialia* **22,** 101428. ISSN: 2589-1529. doi:10.1016/j.mtla.2022.101428 (2022).

38. Cahoon, J. R., Li, Q. & Richards, N. L. Microstructural and processing factors influencing the formation of annealing twins. *Materials Science and Engineering: A* **526,** 56–61. ISSN: 0921-5093. doi:10.1016/j.msea.2009.07.021 (2009).

39. Lu, L., Shen, Y., Chen, X., Qian, L. & Lu, K. Ultrahigh Strength and High Electrical Conductivity in Copper. *Science* **304,** 422–426. doi:10.1126/science.1092905 (2004).

40. Hodge, A. M., Wang, Y. M. & Barbee, T. W. Large-scale production of nano-twinned, ultrafine-grained copper. *Materials Science and Engineering: A* **429,** 272–276. ISSN: 0921-5093. doi:10.1016/j.msea.2006.05.109 (2006).

41. Mahajan, S., Pande, C. S., Imam, M. A. & Rath, B. B. Formation of annealing twins in f.c.c. crystals. *Acta Materialia* **45,** 2633–2638. ISSN: 1359-6454. doi:10.1016/S1359-6454(96)00336-9 (1997).

42. Gleiter, H. The formation of annealing twins. *Acta Metallurgica* **17,** 1421–1428. ISSN: 0001-6160. doi:10.1016/0001-6160(69)90004-2 (1969).

43. Carter, C. B. & Ray, I. L. F. On the stacking-fault energies of copper alloys. *The Philosophical Magazine: A Journal of Theoretical Experimental and Applied Physics* **35,** 189–200. ISSN: 0031-8086. doi:10.1080/14786437708235982 (1977).

44. Carter, C. B. & Holmes, S. M. The stacking-fault energy of nickel. *The Philosophical Magazine: A Journal of Theoretical Experimental and Applied Physics* **35,** 1161–1172. ISSN: 0031-8086. doi:10.1080/14786437708232942 (1977).

45. Alwen, A., Liang, A., Branicio, P. S. & Hodge, A. M. Combinatorial and high-throughput investigation of growth nanotwin formation. *Acta Materialia* **270,** 119839. ISSN: 1359-6454. doi:10.1016/j.actamat.2024.119839 (2024).

46. Den Broeder, F. J. A. & Nakahara, S. Diffusion induced grain boundary migration and recrystallization in the CuNi system. *Scripta Metallurgica* **17,** 399–404. ISSN: 0036-9748. doi:10.1016/0036-9748(83)90181-3 (1983).

47. Nakahara, S. & den Broeder, F. J. A. Diffusion-induced grain boundary migration in heated CuNi alloy targets during sputtering. *Scripta Metallurgica* **17,** 607–610. ISSN: 0036-9748. doi:10.1016/0036-9748(83)90386-1 (1983).

48. Kizaki, T., O, M. & Kajihara, M. Kinetics of Diffusion Induced Recrystallization in the Cu(Al) System. *MATERIALS TRANSACTIONS* **61.** Publisher: The Japan Institute of Metals and Materials, 206–212. ISSN: 1345-9678, 1347-5320. doi:10.2320/matertrans.MT-M2019174 (2020).

49. Liu, D., Miller, W. A. & Aust, K. T. Diffusion induced grain boundary migration in a rapidly solidified, oxidized NiCu alloy. *Scripta Metallurgica* **21,** 643–647. ISSN: 0036-9748. doi:10.1016/0036-9748(87)90377-2 (1987).

50. Yoon, D. Theories and observations of chemically induced interface migration. *International Materials Reviews* **40,** 149–179. ISSN: 0950-6608, 1743-2804. doi:10.1179/imr.1995.40.4.149 (1995).

51. Lewis, J. S. 105. The reduction of copper oxide by hydrogen. en. *J. Chem. Soc.,* 820–826. ISSN: 0368-1769. doi:10.1039/JR9320000820 (1932).

52. Pease, R. N. & Taylor, H. S. THE REDUCTION OF COPPER OXIDE BY HYDROGEN. *J. Am. Chem. Soc.* **43,** 2179–2188. ISSN: 0002-7863. doi:10.1021/ja01443a007 (1921).

53. Hidayat, T., Rhamdhani, M. A., Jak, E. & Hayes, P. C. On the Relationships between the Kinetics and Mechanisms of Gaseous Hydrogen Reduction of Solid Nickel Oxide. en. *Metall Mater Trans B* **40,** 474–489. ISSN: 1543-1916. doi:10.1007/s11663-009-9239-x (2009).

54. Jeangros, Q. *et al.* Reduction of nickel oxide particles by hydrogen studied in an environmental TEM. en. *J Mater Sci* **48,** 2893–2907. ISSN: 1573-4803. doi:10.1007/s10853-012-7001-2 (2013).

55. Backhaus-Ricoult, M. & Ricoult, D. Electron microscopy of internally reduced (Mg, Ni)O. *Journal of Materials Science* **23.** Publisher: Springer Science and Business Media LLC, 1309–1316. ISSN: 0022-2461, 1573-4803. doi:10.1007/bf01154594 (1988).

56. Narayan, J. Epitaxial Growth Of Nickel Nanocrystals By Domain Matching Epitaxy. *MRS Proceedings* **877.** Publisher: Springer Science and Business Media LLC. ISSN: 0272-9172, 1946-4274. doi:10.1557/proc-877-s4.7 (2005).

57. Ricoult, D. L. & Schmalzried, H. Internal reactions in the (Mg, Me)O system. *Journal of Materials Science* **22,** 2257–2266. ISSN: 1573-4803. doi:10.1007/BF01132969 (1987).

58. Fecht, H. & Gleiter, H. A lock-in model for the atomic structure of interphase boundaries between metals and ionic crystals. *Acta Metallurgica* **33,** 557–562. ISSN: 00016160. doi:10.1016/0001-6160(85)90019-7 (1985).

59. Atkinson, A. Diffusion along grain boundaries and dislocations in oxides, alkali halides and carbides. *Solid State Ionics* **12,** 309–320. ISSN: 01672738. doi:10.1016/0167-2738(84)90160-7 (1984).

60. Atkinson, A. & Taylor, R. I. Impurity diffusion in NiO grain boundaries. *Journal of Physics and Chemistry of Solids* **47,** 315–323. ISSN: 0022-3697. doi:10.1016/0022-3697(86)90101-0 (1986).

61. Little, J. A., Evans, J. W. & Westmacott, K. H. Early stages of reduction of nickel oxide single crystals: An investigation by transmission electron microscope. en. *Metall Trans B* **11,** 519–524. ISSN: 2379-0229. doi:10.1007/BF02676897 (1980).

62. Pöyhtäri, S. *et al.* Kinetic Analysis of Hydrogen Reduction of Nickel Compounds. en. *Metall Mater Trans B.* ISSN: 1543-1916. doi:10.1007/s11663-023-02955-6 (2023).

63. Zou, L., Li, J., Zakharov, D., Stach, E. A. & Zhou, G. In situ atomic-scale imaging of the metal/oxide interfacial transformation. en. *Nat Commun* **8,** 307. ISSN: 2041-1723. doi:10.1038/s41467-017-00371-4 (2017).

64. Rodriguez, J. A., Hanson, J. C., Frenkel, A. I., Kim, J. Y. & Pérez, M. Experimental and Theoretical Studies on the Reaction of H2 with NiO: Role of O Vacancies and Mechanism for Oxide Reduction. *J. Am. Chem. Soc.* **124,** 346–354. ISSN: 0002-7863. doi:10.1021/ja0121080 (2002).

65. Rodriguez, J. A., Kim, J. Y., Hanson, J. C., Pérez, M. & Frenkel, A. I. Reduction of CuO in H2: In Situ Time-Resolved XRD Studies. en. *Catalysis Letters* **85,** 247–254. ISSN: 1572-879X. doi:10.1023/A:1022110200942 (2003).

66. Coury, F. G., Miller, C., Field, R. & Kaufman, M. On the origin of diffuse intensities in fcc electron diffraction patterns. en. *Nature* **622,** 742–747. ISSN: 1476-4687. doi:10.1038/s41586-023-06530-6 (2023).

67. Zhang, R. *et al.* Short-range order and its impact on the CrCoNi medium-entropy alloy. en. *Nature* **581,** 283–287. ISSN: 1476-4687. doi:10.1038/s41586-020-2275-z (2020).

68. Chen, X. *et al.* Direct observation of chemical short-range order in a medium-entropy alloy. en. *Nature* **592,** 712–716. ISSN: 1476-4687. doi:10.1038/s41586-021-03428-z (2021).

69. Walsh, F., Zhang, M., Ritchie, R. O., Asta, M. & Minor, A. M. Multiple origins of extra electron diffractions in fcc metals. *Science Advances* **10.** Publisher: American Association for the Advancement of Science, eadn9673. doi:10.1126/sciadv.adn9673 (2024).

70. Xiao, H. Z. & Daykin, A. C. Extra diffractions caused by stacking faults in cubic crystals. *Ultramicroscopy* **53,** 325–331. ISSN: 0304-3991. doi:10.1016/0304-3991(94)90045-0 (1994).

71. Clapp, P. C. Atomic Configurations in Binary Alloys. en. *Phys. Rev. B* **4,** 255–270. ISSN: 0556-2805. doi:10.1103/PhysRevB.4.255 (1971).

72. Mozer, B., Keating, D. T. & Moss, S. C. Neutron Measurement of Clustering in the Alloy CuNi. en. *Phys. Rev.* **175,** 868–876. ISSN: 0031-899X. doi:10.1103/PhysRev.175.868 (1968).

73. Turchanin, M. A., Agraval, P. G. & Abdulov, A. R. Phase equilibria and thermodynamics of binary copper systems with 3d-metals. VI. Copper-nickel system. en. *Powder Metall Met Ceram* **46,** 467–477. ISSN: 1573-9066. doi:10.1007/s11106-007-0073-x (2007).

74. Hall, E. O. The Deformation and Ageing of Mild Steel: III Discussion of Results. *Proceedings of the Physical Society. Section B* **64,** 747. ISSN: 0370-1301. doi:10.1088/0370-1301/64/9/303 (1951).

75. Cordero, Z. C., Knight, B. E. & Schuh, C. A. Six decades of the Hall–Petch effect – a survey of grain-size strengthening studies on pure metals. *International Materials Reviews* **61.** Publisher: SAGE Publications, 495–512. ISSN: 0950-6608. doi:10.1080/09506608.2016.1191808 (2016).

76. Gallivan, R. A. *The Role of Boundaries and Other Microstructural Features on Emergent Mechanical and Mechanically-Coupled Phenomena at the Nanoscale* PhD thesis (California Institute of Technology, 2023). doi:10.7907/gv3v-9k07.

77. Pande, C., Rath, B. & Imam, M. Effect of annealing twins on Hall–Petch relation in polycrystalline materials. *Materials Science and Engineering: A* **367,** 171–175. ISSN: 09215093. doi:10.1016/j.msea.2003.09.100 (2004).

78. Chang, S.-Y. & Chang, T.-K. Grain size effect on nanomechanical properties and deformation behavior of copper under nanoindentation test. *Journal of Applied Physics* **101,** 033507. ISSN: 0021-8979. doi:10.1063/1.2432873 (2007).

79. Bansal, S., Toimil-Molares, E., Saxena, A. & Tummala, R. *Nanoindentation of single crystal and polycrystalline copper nanowires* in *Proceedings Electronic Components and Technology, 2005. ECTC '05.* Electronic Components and Technology, 2005. ECTC '05. ISSN: 2377-5726 (2005), 71–76 Vol. 1. doi:10.1109/ECTC.2005.1441248.

80. Emeis, F., Peterlechner, M., Divinski, S. V. & Wilde, G. Grain boundary engineering parameters for ultrafine grained microstructures: Proof of principles by a systematic composition variation in the Cu-Ni system. *Acta Materialia* **150,** 262–272. ISSN: 1359-6454. doi:10.1016/j.actamat.2018.02.054 (2018).

81. Bahr, D. F. & Vasquez, G. Effect of solid solution impurities on dislocation nucleation during nanoindentation. en. *Journal of Materials Research* **20,** 1947–1951. ISSN: 2044-5326. doi:10.1557/JMR.2005.0244 (2005).

82. Greer, J. R. & De Hosson, J. T. Plasticity in small-sized metallic systems: Intrinsic versus extrinsic size effect. *Progress in Materials Science* **56,** 654–724. ISSN: 00796425. doi:10.1016/j.pmatsci.2011.01.005 (2011).

83. Greer, J. R., Oliver, W. C. & Nix, W. D. Size dependence of mechanical properties of gold at the micron scale in the absence of strain gradients. *Acta Materialia* **53,** 1821–1830. ISSN: 1359-6454. doi:10.1016/j.actamat.2004.12.031 (2005).

84. Sneddon, I. N. Boussinesq's problem for a flat-ended cylinder. *Mathematical Proceedings of the Cambridge Philosophical Society* **42,** 29–39. ISSN: 1469-8064, 0305-0041. doi:10.1017/S0305004100022702 (1946).

85. Zhang, H., Schuster, B. E., Wei, Q. & Ramesh, K. T. The design of accurate micro-compression experiments. *Scripta Materialia* **54,** 181–186. ISSN: 1359-6462. doi:10.1016/j.scriptamat.2005.06.043 (2006).

86. Bower, A. F. *Applied mechanics of solids* OCLC: ocn277196164. 794 pp. ISBN: 978-1-4398-0247-2 (CRC Press, Boca Raton, 2010).

87. Fei, H., Abraham, A., Chawla, N. & Jiang, H. Evaluation of Micro-Pillar Compression Tests for Accurate Determination of Elastic-Plastic Constitutive Relations. *Journal of Applied Mechanics* **79.** ISSN: 0021-8936. doi:10.1115/1.4006767 (2012).

88. Kratochvíl, P. & Neradová, E. Solid solution hardening in some copper base alloys. en. *Czech J Phys* **21,** 1273–1278. ISSN: 1572-9486. doi:10.1007/BF01699490 (1971).

89. Osswald, E. Zugversuche an Kupfer-Nickelkristallen. de. *Z. Physik* **83,** 55–78. ISSN: 0044-3328. doi:10.1007/BF01331092 (1933).

90. Suzuki, H. in *Strength of Metals and Alloys (ICSMA 8)* (eds Kettunen, P. O., Lepistö, T. K. & Lehtonen, M. E.) 573–578 (Pergamon, Oxford, 1989). ISBN: 978-0-08-034804-9. doi:10.1016/B978-0-08-034804-9.50088-7.

91. Dimiduk, D. M., Uchic, M. D. & Parthasarathy, T. A. Size-affected single-slip behavior of pure nickel microcrystals. *Acta Materialia* **53,** 4065–4077. ISSN: 1359-6454. doi:10.1016/j.actamat.2005.05.023 (2005).

92. Jennings, A. T., Burek, M. J. & Greer, J. R. Microstructure versus Size: Mechanical Properties of Electroplated Single Crystalline Cu Nanopillars. *Phys. Rev. Lett.* **104,** 135503. doi:10.1103/PhysRevLett.104.135503 (2010).

93. Schneider, A. S. *et al.* Correlation between critical temperature and strength of small-scale bcc pillars. eng. *Phys Rev Lett* **103,** 105501. ISSN: 0031-9007. doi:10.1103/PhysRevLett.103.105501 (2009).

94. Gu, R. & Ngan, A. H. W. Size effect on the deformation behavior of duralumin micropillars. *Scripta Materialia* **68,** 861–864. ISSN: 1359-6462. doi:10.1016/j.scriptamat.2013.02.012 (2013).

95. Lu, L. *et al.* Nano-sized twins induce high rate sensitivity of flow stress in pure copper. *Acta Materialia* **53,** 2169–2179. ISSN: 1359-6454. doi:10.1016/j.actamat.2005.01.031 (2005).

96. Labusch, R. A Statistical Theory of Solid Solution Hardening. en. *physica status solidi (b)* **41,** 659–669. ISSN: 1521-3951. doi:10.1002/pssb.19700410221 (1970).

97. Fleisgher, R. L. Solution hardening. *Acta Metallurgica* **9,** 996–1000. ISSN: 0001-6160. doi:10.1016/0001-6160(61)90242-5 (1961).

98. Suzuki, T., Takeuchi, S. & Yoshinaga, H. en. in *Dislocation Dynamics and Plasticity* (eds Suzuki, T., Takeuchi, S. & Yoshinaga, H.) 32–46 (Springer, Berlin, Heidelberg, 1991). ISBN: 978-3-642-75774-7. doi:10.1007/978-3-642-75774-7_3.

99. Nakanishi, K. & Suzuki, H. Analysis of the Grain Size Dependence of the Yield Stress in Copper-Aluminum and Copper-Nickel Alloys. *Transactions of the Japan Institute of Metals* **15,** 435–440. doi:10.2320/matertrans1960.15.435 (1974).

100. Parthasarathy, T. A., Rao, S. I., Dimiduk, D. M., Uchic, M. D. & Trinkle, D. R. Contribution to size effect of yield strength from the stochastics of dislocation source lengths in finite samples. *Scripta Materialia* **56,** 313–316. ISSN: 1359-6462. doi:10.1016/j.scriptamat.2006.09.016 (2007).

101. El-Awady, J. A. *et al.* Pre-straining effects on the power-law scaling of size-dependent strengthening in Ni single crystals. en. *Scripta Materialia* **68,** 207–210. ISSN: 13596462. doi:10.1016/j.scriptamat.2012.10.035 (2013).

102. Schneider, A. *et al.* Influence of bulk pre-straining on the size effect in nickel compression pillars. en. *Materials Science and Engineering: A* **559,** 147–158. ISSN: 09215093. doi:10.1016/j.msea.2012.08.055 (2013).

103. Girault, B., Schneider, A. S., Frick, C. P. & Arzt, E. Strength Effects in Micropillars of a Dispersion Strengthened Superalloy. en. *Advanced Engineering Materials* **12.** ISSN: 1527-2648. doi:10.1002/adem.201000089 (2010).

104. Li, S.-H., Zhao, Y., Lau, K. B., Wang, P. & Upadrasta, R. Micropillar compression investigation on the mechanical behavior of Ni manufactured using laser powder bed fusion. *Materials Science and Engineering: A* **879,** 145269. ISSN: 0921-5093. doi:10.1016/j.msea.2023.145269 (2023).

105. Tran, T. T., Zhang, W., Joyce, K. J., Wu, A. & Greer, J. R. Oxide-Dispersion Strengthened Alloys Printed via Hydrogel Infusion-Based Additive Manufacturing (HIAM). *In preparation* (2025).

106. Bergerhoff, G., Hundt, R., Sievers, R. & Brown, I. D. The inorganic crystal structure data base. *Journal of Chemical Information and Computer Sciences* **23.** Publisher: American Chemical Society, 66–69. ISSN: 0095-2338. doi:10.1021/ci00038a003 (1983).

107. Bale, C. *et al.* FactSage thermochemical software and databases, 2010–2016. *Calphad* **54,** 35–53. ISSN: 03645916. doi:10.1016/j.calphad.2016.05.002 (2016).

108. Gadalla, A. M. & Kongkachuichay, P. Compatible phases of the Y_2 O_3 –CuO–Cu_2 O system in air. *Journal of Materials Research* **6,** 450–454. ISSN: 0884-2914, 2044-5326. doi:10.1557/JMR.1991.0450 (1991).

109. Manohar, P. A., Ferry, M. & Chandra, T. Five Decades of the Zener Equation. *ISIJ International* **38,** 913–924. doi:10.2355/isijinternational.38.913 (1998).

110. Ishiguro, T., Ishizawa, N., Mizutani, N. & Kato, M. A new delafossite-type compound CuYO2. *Journal of Solid State Chemistry* **49,** 232–236. ISSN: 0022-4596. doi:10.1016/0022-4596(83)90117-2 (1983).

111. Zhu, Y. & Wu, X. Heterostructured materials. *Progress in Materials Science* **131,** 101019. ISSN: 0079-6425. doi:10.1016/j.pmatsci.2022.101019 (2023).

112. Tran, T. T. & Greer, J. R. Nonisothermal Kinetics of Reduction in Hydrogel Infusion-Based Additive Manufacturing. *In preparation* (2025).

113. Richardson, J. T., Scates, R. & Twigg, M. V. X-ray diffraction study of nickel oxide reduction by hydrogen. *Applied Catalysis A: General* **246,** 137–150. ISSN: 0926-860X. doi:10.1016/S0926-860X(02)00669-5 (2003).

114. Khawam, A. & Flanagan, D. R. Solid-State Kinetic Models: Basics and Mathematical Fundamentals. *The Journal of Physical Chemistry B* **110.** Publisher: American Chemical Society, 17315–17328. ISSN: 1520-6106. doi:10.1021/jp062746a (2006).

115. Friedman, H. L. Kinetics of thermal degradation of char-forming plastics from thermogravimetry. Application to a phenolic plastic. *Journal of Polymer Science Part C: Polymer Symposia* **6,** 183–195. ISSN: 1935-3065. doi:10.1002/polc.5070060121 (1964).

116. Pérez-Maqueda, L. A., Criado, J. M. & Sánchez-Jiménez, P. E. Combined Kinetic Analysis of Solid-State Reactions: A Powerful Tool for the Simultaneous Determination of Kinetic Parameters and the Kinetic Model without Previous Assumptions on the Reaction Mechanism. *The Journal of Physical Chemistry A* **110.** Publisher: American Chemical Society, 12456–12462. ISSN: 1089-5639. doi:10.1021/jp064792g (2006).

117. Perejón, A., Sánchez-Jiménez, P. E., Criado, J. M. & Pérez-Maqueda, L. A. Kinetic Analysis of Complex Solid-State Reactions. A New Deconvolution Procedure. *The Journal of Physical Chemistry B* **115.** Publisher: American Chemical Society, 1780–1791. ISSN: 1520-6106. doi:10.1021/jp110895z (2011).

118. Gotor, F. J., Criado, J. M., Malek, J. & Koga, N. Kinetic Analysis of Solid-State Reactions: The Universality of Master Plots for Analyzing Isothermal and Nonisothermal Experiments. *The Journal of Physical Chemistry A* **104.** Publisher: American Chemical Society, 10777–10782. ISSN: 1089-5639. doi:10.1021/jp0022205 (2000).

119. Svoboda, R. & Málek, J. Applicability of Fraser–Suzuki function in kinetic analysis of complex crystallization processes. *Journal of Thermal Analysis and Calorimetry* **111,** 1045–1056. ISSN: 1572-8943. doi:10.1007/s10973-012-2445-9 (2013).

120. Vyazovkin, S. *et al.* ICTAC Kinetics Committee recommendations for analysis of multi-step kinetics. *Thermochimica Acta* **689,** 178597. ISSN: 00406031. doi:10.1016/j.tca.2020.178597 (2020).

121. Resentera, A. C. & Rodriguez, M. H. Some limitations of the Fraser-Suzuki function for fitting thermokinetic curves. *Thermochimica Acta* **725,** 179520. ISSN: 0040-6031. doi:10.1016/j.tca.2023.179520 (2023).

122. Fedorov, A. V. *et al.* Temperature-programmed reduction of model CuO, NiO and mixed CuO–NiO catalysts with hydrogen. *Journal of Alloys and Compounds* **844,** 156135. ISSN: 0925-8388. doi:10.1016/j.jallcom.2020.156135 (2020).

123. Gentry, S. J., Hurst, N. W. & Jones, A. Study of the promoting influence of transition metals on the reduction of cupric oxide by temperature programmed reduction. *Journal of the Chemical Society, Faraday Transactions 1: Physical Chemistry in Condensed Phases* **77.** Publisher: The Royal Society of Chemistry, 603–619. ISSN: 0300-9599. doi:10.1039/F19817700603 (1981).

124. Furstenau, R. P., McDougall, G. & Langell, M. A. Initial stages of hydrogen reduction of NiO(100). *Surface Science* **150,** 55–79. ISSN: 0039-6028. doi:10.1016/0039-6028(85)90211-0 (1985).